National Library
of Canada

Acquisitions and
Bibliographic Services Branch

395 Wellington Street
Ottawa, Ontario
K1A 0N4

Bibliothèque nationale
du Canada

Direction des acquisitions et
des services bibliographiques

395, rue Wellington
Ottawa (Ontario)
K1A 0N4

Your file Votre référence

Our file Notre référence

NOTICE

The quality of this microform is heavily dependent upon the quality of the original thesis submitted for microfilming. Every effort has been made to ensure the highest quality of reproduction possible.

If pages are missing, contact the university which granted the degree.

Some pages may have indistinct print especially if the original pages were typed with a poor typewriter ribbon or if the university sent us an inferior photocopy.

Reproduction in full or in part of this microform is governed by the Canadian Copyright Act, R.S.C. 1970, c. C-30, and subsequent amendments.

AVIS

La qualité de cette microforme dépend grandement de la qualité de la thèse soumise au microfilmage. Nous avons tout fait pour assurer une qualité supérieure de reproduction.

S'il manque des pages, veuillez communiquer avec l'université qui a conféré le grade.

La qualité d'impression de certaines pages peut laisser à désirer, surtout si les pages originales ont été dactylographiées à l'aide d'un ruban usé ou si l'université nous a fait parvenir une photocopie de qualité inférieure.

La reproduction, même partielle, de cette microforme est soumise à la Loi canadienne sur le droit d'auteur, SRC 1970, c. C-30, et ses amendements subséquents.

Canada

UNIVERSITY OF ALBERTA

CHARACTERIZING THE MAGNETIC FIELD AT GEOSTATIONARY ORBIT

BY ©

SUSAN SKONE

A thesis submitted to the Faculty of Graduate Studies and Research in partial fulfillment of the requirements for the degree of Master of Science in Physics.

Department of Physics

Edmonton Alberta

Spring 1994

National Library
of Canada

Acquisitions and
Bibliographic Services Branch

395 Wellington Street
Ottawa, Ontario
K1A 0N4

Bibliothèque nationale
du Canada

Direction des acquisitions et
des services bibliographiques

395, rue Wellington
Ottawa (Ontario)
K1A 0N4

Your file Votre référence

Our file Notre référence

The author has granted an irrevocable non-exclusive licence allowing the National Library of Canada to reproduce, loan, distribute or sell copies of his/her thesis by any means and in any form or format, making this thesis available to interested persons.

The author retains ownership of the copyright in his/her thesis. Neither the thesis nor substantial extracts from it may be printed or otherwise reproduced without his/her permission.

L'auteur a accordé une licence irrévocable et non exclusive permettant à la Bibliothèque nationale du Canada de reproduire, prêter, distribuer ou vendre des copies de sa thèse de quelque manière et sous quelque forme que ce soit pour mettre des exemplaires de cette thèse à la disposition des personnes intéressées.

L'auteur conserve la propriété du droit d'auteur qui protège sa thèse. Ni la thèse ni des extraits substantiels de celle-ci ne doivent être imprimés ou autrement reproduits sans son autorisation.

ISBN 0-612-11372-8

Canada

University of Alberta

Release Form

Name of Author:	Susan Skone
Title of Thesis:	Characterizing the Magnetic Field at Geostationary Orbit
Degree:	Master of Science
Year This Degree Granted:	1994

Permission is hereby granted to the University of Alberta to reproduce single copies of this thesis and to lend or sell such copies for private, scholarly or scientific research purposes only.

The author reserves all other publication and other rights in association with the copyright in the thesis, and except as hereinbefore provided neither the thesis nor any substantial proportion thereof may be printed or otherwise reproduced in any material form whatever without the author's written permission.

Susan Skone.

Susan Skone
Department of Physics
University of Alberta
Edmonton, Alberta
T6G 2J1
Canada

26 January 1994

UNIVERSITY OF ALBERTA

FACULTY OF GRADUATE STUDIES AND RESEARCH

The undersigned certify that they have read, and recommend to the Faculty of Graduate Studies and Research for acceptance, a thesis entitled "Characterizing the Magnetic Field at Geostationary Orbit" submitted by Susan Skone in partial fulfillment of the requirements for the degree of Master of Science in Physics.

G. Rostoker, Supervisor

C R James

C. R. James

D. P. Hube

J. C. Samson

26 January 1994

CNSR
Canadian Network
For
Space Research

A Network of Centres of Excellence

26 Jan 1994

To whom it may concern,

I hereby grant the authorization for Susan Skone to include a copy of figure 1 from the paper Magnetospheric substorms as a signature of the solar terrestrial interaction, in *Ionospheric Structure and Variability on a Global Scale and Interactions with Atmosphere and Magnetosphere*, in the thesis Characterizing the Magnetic Field at Geostationary Orbit.

Gordon Rostoker

BIOLOGICAL SCIENCES BLDG., CW-005, UNIVERSITY OF ALBERTA, EDMONTON, ALBERTA, CANADA T6G 2E9 TELEPHONE (403) 492-6568 FAX (403) 492-4256

MAGNETOSPHERIC
SUBSTORMS.

Published under the aegis of the AGU Books Board.

Library of Congress Cataloging-in-Publication Data

Magnetospheric substorms / Joseph R. Kan . . . [et al.], editors.
p. cm. — (Geophysical monograph : 64)
ISBN 0-87590-030-5
1. Magnetospheric substorms—Congresses. I. Kan, Joseph R.
II. Series.
QC809.M35M333 1991
538'.766—dc20 91-34806
CIP

ISBN 0-87590-030-5

Copyright 1991 by the American Geophysical Union, 2000 Florida Avenue, NW, Washington, DC 20009, U.S.A.

Figures, tables, and short excerpts may be reprinted in scientific books and journals if the source is properly cited.

Authorization to photocopy items for internal or personal use, or the internal or personal use of specific clients, is granted by the American Geophysical Union for libraries and other users registered with the Copyright Clearance Center (CCC) Transactional Reporting Service, provided that the base fee of $1.00 per copy plus $0.10 per page is paid directly to CCC, 21 Congress Street, Salem, MA 10970. 0065-8448/89/$01. + .10.

This consent does not extend to other kinds of copying, such as copying for creating new collective works or for resale. The reproduction of multiple copies and the use of full articles or the use of extracts, including figures and tables, for commercial purposes requires permission from AGU.

Printed in the United States of America.

fig. 7,8

THE UNIVERSITY OF ALBERTA

RELEASE FORM

NAME OF AUTHOR ..Terence John Hughes..

TITLE OF THESIS ..A Comprehensive Model of Ionospheric-
Magnetospheric Current Systems During
Periods of Moderate Magnetospheric Activity

DEGREE FOR WHICH THESIS WAS PRESENTED ..Ph.D...

YEAR THIS DEGREE GRANTED ..1978..

Permission is hereby granted to THE UNIVERSITY OF ALBERTA LIBRARY to reproduce single copies of this thesis and to lend or sell such copies for private, scholarly or scientific research purposes only.

The author reserves other publication rights, and neither the thesis nor extensive extracts from it may be printed or otherwise reproduced without the author's written permission.

(Signed) Terence John Hughes

PERMANENT ADDRESS:

Radiological Research Labs,
University of Toronto,
Toronto, Ontario.

DATED 27 March 1978

Geophysical Research Letters

Editor-in-Chief
James L. Burch

Editors
Jeff Dozier
David Halpern
Hiroshi Matsumoto
Peter L. Olson
David Rees
Philip Russell

Associate Editors
Andrew F. Cheng
Thomas E. Cravens
Janet U. Kozyra
Max Loewenstein
William Lotko
L. R. Lyons
Richard B. Rood
David M. Rust
Michelle F. Thomsen
J. Hunter Waite, Jr.

* * *

The Editors of **Geophysical Research Letters** welcome short, interesting contributions of broad geophysical interest. GRL Letters should be written in a style that makes their meaning and content clear to scientists from diverse geophysical disciplines. Ideally, the abstract and introduction should be easily understood by a beginning graduate student.

To submit a Letter, send 5 copies of the manuscript to one of the editors listed below. The covering letter should include the author's telephone number and the names, addresses, and telephone numbers of five potential referees.

James L. Burch, Geophysical Research Letters, Southwest Research Institute, P.O. Drawer 28510, San Antonio, TX 78228-0510 USA; telephone (210) 522-2526; telex 244846
Editorial Assistant: William S. Lewis (210) 522-5261

Jeff Dozier, Geophysical Research Letters, 2000 Florida Ave., NW, Washington, D. C. 20009 USA
Editorial Assistant: Jean Connelly (202) 462-6900; FAX (202) 328-0566

David Halpern, Jet Propulsion Laboratory, M/S 300-323, California Institute of Technology, Pasadena, CA 91109 USA; telephone (818) 354-5327; FAX (818) 393-6720
Editorial Assistant: Elizabeth Granite (818) 354-1940

Hiroshi Matsumoto, Radio Atmospheric Science Center, Kyoto University, Uji, Kyoto 611, JAPAN; FAX 011-81-774-31-8463

Peter L. Olson, Geophysical Research Letters, Department of Earth and Planetary Sciences, The Johns Hopkins University, Baltimore, MD 21218 USA
Editorial Assistant: Shirley Johnson (410) 516-7680; FAX (410) 516-7933

David Rees, Atmospheric Physics Laboratory, University College London, 67-73 Riding House Street, London W1P 7PP, UK; telephone 71-436-7614; FAX 71-436-7615

Philip Russell, Geophysical Research Letters, 2000 Florida Ave., NW, Washington, D. C. 20009 USA
Editorial Assistant: Jean Connelly (202)462-6900; FAX (202) 328-0566

Manuscript Preparation. To expedite publication and hold down page charges, papers submitted to GRL are strictly limited to 4 printed pages, and Comments and Replys to 2 pages ordinarily.

GRL contributions first undergo the usual review process. Authors send papers to the editors as double-spaced typescript. Including text, title, abstract, references, tables and all graphics, these should be the equivalent (or less) of 12 double-spaced pages.

After acceptance, camera-ready copy must be sent to AGU as single-spaced typewriting or typesetting to these widths: for single columns 10.4 cm (4⅛ in.) maximum & 9.8 cm (3⅞ in.) minimum; for double columns 21.6 cm (8½ in.); and for broadside tables and figures 29.8 cm (11¾ in.). Words and illustrations together cannot exceed 239 cm (94 in.) in depth. Sans serif typefaces are unacceptable.

If any previously published figures are to be reproduced in GRL, the AGU office must have written permission from the copyright holder. Copies of these permissions must accompany the figures. Moreover, AGU cannot process or publish any camera-ready copy until a signed copyright transfer form is received at AGU.

Publications Office. For assistance with accepted manuscripts, color charges, typographic or typewriter specifications, or AGU publication policy, contact: Cynthia A. Duck, *Production Coordinator,* (202) 462-6900.
TWX 710-822-9300 FAX 202-328-0566

Judy C. Holoviak, *Director of Publications*

Publication Charges. Author's institutions are requested to pay a publication charge of $93 per journal page, which entitles them to 100 reprints.

Microform Publications. To help meet the strict page limit for GRL, supporting material, such as data tables, lengthy mathematical derivations, and extended discussion, can with the editor's approval, be microfiched. (Photographs with a wide tonal range are not suitable.)

This supplemental material is included in GRL's microfiche editions which are archived by libraries. Individuals may order microfiche supplements separately for a small charge from AGU.

Subscriptions. AGU members may subscribe to GRL in printed or microfiche editions for their personal use at an annual rate of $55 (U.S. members) and $74 (non-U.S. members). Student members may subscribe at reduced rates. Contact AGU for special rates for libraries and other multiple-use institutions. Individual nonmembers interested in subscribing to GRL for personal use should contact AGU. Single-issue prices are available on request.

Claims and Changes of Address. Send address changes to AGU Customer Service Department with at least 5 weeks' advance notice. Claims due to insufficient notice of address change or for such reasons as "missing from files" cannot be serviced. For the U.S., lost mail should be reported within 90 days of the last day of the month of publication; for other countries, within 150 days.

Copyright. Permission is granted for individuals to make single copies for personal use in research, study, or teaching and to use figures and tables and short quotes from this journal for re-publication in scientific books and journals. AGU requests that the source be cited appropriately; there is no charge.

The appearance of the code at the foot of the first page of an article in this journal indicates the copyright owner's consent that copies of the article may be made for personal or internal use, or for the personal or internal use of specific clients. This consent is given on the condition that the copier pay the stated per copy fee through the Copyright Clearance Center, Inc. for copying beyond that permitted by Section 107 or Section 108 of the U.S. Copyright Law. This consent does not extend to other kinds of copying, such as that for advertising or promotional purposes, creating new collective works, or resale. Articles published prior to 1980 are subject to the same provisions. Reproduction of multiple copies and the use of full articles or extracts, including figures and tables, for commercial purposes requires specific written permission from AGU.

POSTMASTER: Send address changes to **Geophysical Research Letters,** American Geophysical Union, 2000 Florida Avenue, N.W., Washington, D.C. 20009 USA.

Geophysical Research Letters (ISSN 0094-8276) is published semimonthly for $55 per year for members' personal use by the American Geophysical Union from 2000 Florida Avenue, N.W., Washington, D.C. 20009. Second-class postage paid at Washington, D.C., and at additional mailing offices.

Copyright 1993
by American Geophysical Union. 09/03/93

Fig. 15

JGR

The *JGR* editors welcome original scientific contributions on the physics and chemistry of the Earth, its environment, and the solar system.

Editors

CHRISTOPH K. GOERTZ, deceased
W.-H. IP AND Y. KAMIDE

Papers on aeronomy and magnetospheric physics, planetary atmospheres and magnetospheres, interplanetary and external solar physics, cosmic rays, and heliospheric physics are published in *JGR-Space Physics* and should be submitted directly to one of the editors listed below. Four copies of the typescript should be submitted to the appropriate editor:

JAMES A. VAN ALLEN, Acting Editor
Journal of Geophysical Research
Department of Physics and Astronomy
University of Iowa
Iowa City, Iowa 52242

EDITOR'S ASSISTANTS:
Jo Ann Beard
Mary Allen
(319) 335-0635
Telefax: (319) 335-1753

W.-H. IP, European Editor
Max-Planck-Institut für Aeronomie
D-3411 Katlenburg-Lindau
Federal Republic of Germany
(49) 5556-401-416
Telefax: (49) 5556-401-240

Y. KAMIDE, Asian and Pacific Editor
Solar-Terrestrial Environment Laboratory
Nagoya University
Toyokawa 442
Japan
(81) 533-86-3164
Telefax: (81) 533-89-0409
Telex: 5422-661 KSU J

Associate Editors

L. P. Block
W. J. Burke
J. T. Clarke
K. P. Dere
C. G. Fesen
J. L. Fox
H. S. Hudson
R. Johnson
A. D. Johnstone
T. L. Killeen
J. U. Kozyra
L. C. Lee
W. Lotko
R. Lysak
E. Marsch
B.H. Mauk
E. Mobius
J. Rottger
A. Roux
J.-P. St.-Maurice
T. Sato
M. Saunders
K. Schindler
J. D. Scudder
H. Spence
M. A. Temerin
C.-Y. Tu
O. L. Vaisberg
R. J. Walker
D. Winske

Judy C. Holoviak, Director of Publications

Journal of Geophysical Research, JGR (ISSN 0148-0227) is published weekly for $492 per year (for AGU members' personal use) by the American Geophysical Union, 2000 Florida Ave., N.W., Washington, DC 20009. Second Class postage paid at Washington, DC, and additional offices. POSTMASTER: Send address changes to *Journal of Geophysical Research*, American Geophysical Union, 2000 Florida Avenue, N.W., Washington, DC 20009 USA.

Copyright 1992 American Geophysical Union.

Manuscript Submission. Papers should be submitted to the Editor dealing with the appropriate topic:

Space Physics to James A. Van Allen, W.-H. Ip, or Y. Kamide.

Solid Earth Sciences to Robert C. Liebermann, Allen Glazner, Richard G. Gordon, Susan Halgedahl, Thomas A. Herring, David F. McTigue, Stuart A. Sipkin, Albert Tarantola, or Alan Zindler.

Ocean Sciences to Larry P. Atkinson, W. J. Jenkins, Julian P. McCreary, James E. Overland, James G. Richman, or Hugh W. Ducklow.

Atmospheric Sciences to Shaw Liu, James Dye, or Kenneth S. Gage.

Planetary Sciences to Clark R. Chapman.

For current addresses of these editors, call or write AGU Author Information (address and phone number below).

Publication Charge Policy. The page charge income received for JGR helps support rapid publication, allows more pages per volume, and makes possible the low subscription rates which result in a circulation of about 4500 issues, about half going to libraries, where wider distribution is afforded. The publication rate for articles typeset by AGU is $150 per printed page. This includes 100 reprints. AGU will typeset only those articles for which this rate is paid. If the author chooses to provide final photo-ready copy, prepared for the printer according to AGU specifications, there is no page charge; reprints are available at $45 per printed page for the first 100.

Authors who cannot produce final photo-ready copy may contact the AGU Publications Program office for assistance.

Foldouts and color figures may be published; however, the additional cost must be borne by the author.

Microform Publication. Authors are encouraged to submit concise papers. To reduce publication expense and allow for complete reporting of work, AGU provides a microfiche deposit service to its authors. This includes printing in JGR an approved typeset summary of an accepted paper and placing the entire manuscript on microfiche at these rates: for the first two typeset pages, no charge; $250 for each additional typeset page; and a $19 deposit charge for each 96 pages or fraction thereof placed on microfiche. In addition to summaries, materials well suited to micropublication include lengthy mathematical derivations, data tables, computer printouts, and appendices. (Photographs with a wide tonal range are not suitable for microfiche.) Detailed information on preparing copy for microfiche is available from AGU Publications. Supplemental material is incorporated in the microform editions of the journal and is part of the archived literature. Microfiche can be ordered at a nominal cost from the AGU business office.

Subscriptions. AGU members may subscribe to the *Journal of Geophysical Research* in printed or microfiche editions for their personal use. Special subscription rates are available to libraries, reading rooms, multiple-use institutions, and individual nonmembers (for personal use).

Claims and Changes of Address. Send address changes to AGU Service Center with at least 5 weeks' advance notice. Claims for missing issues due to insufficient notice of address change or such reasons as "missing from files" cannot be serviced. For the U.S., lost mail should be reported within 90 days of the last day of the month of publication, and for other countries, within 150 days.

Copyright. Permission is granted for individuals to make single copies for personal use in research, study, or teaching and to use figures, tables, and short quotes from this journal for republication in scientific books and journals. There is no charge for any of these uses, but the material must be cited appropriately. The appearance of the code at the bottom of the first page of an article in this journal indicates the copyright owner's consent that copies of the article may be made for personal or internal use or for the personal or internal use of specific clients. This consent is given on the condition that the copier pay the stated per copy fee through the Copyright Clearance Center, Inc., for copying beyond that permitted by Section 107 or Section 108 of the U.S. Copyright Law. This consent does not extend to other kinds of copying, such as copying for general distribution, for advertising or promotional purposes, for creating new collective works, or for resale. Articles published prior to 1980 are subject to the same provisions. The reproduction of multiple copies, the use of full articles, or the use of extracts for commercial purposes requires special permission from AGU.

AGU Headquarters. The AGU Information Service Center (202) 462-6900 is open from 8:30 a.m. to 6:00 p.m. Eastern time to take calls of a general nature related to membership, subscriptions, meetings and publications. Questions of a specific nature will be referred to appropriate staff.

Additionally, the following direct dial lines to the publications department are provided to expedite information relative to paper status, reprints, and page charges and other publication costs.

Reprint Coordinator: (202) 939-3210   Author Information: (202) 939-3200

Address all correspondence to the appropriate department at the American Geophysical Union, 2000 Florida Avenue, N.W., Washington, DC 20009 USA. Telephone (202) 462-6900. TWX 710-822-9300. FAX 202-328-0566.

0192A

fig. 3, 4, 5, 9, 10, 12, 70

Abstract

Observed auroral phenomena are a manifestation of magnetospheric and ionospheric processes. In order to obtain a better understanding of auroral phenomena, it is necessary to determine the magnetospheric source regions of enhanced auroral activity. An identification of such source regions provides insight into the magnetospheric mechanisms which trigger a precipitation of particles into the ionosphere during substorms.

This thesis involves the study of a substorm event, in which auroral regions of enhanced activity are identified and mapped into the magnetosphere. Two magnetic field models are used to perform these mappings: an existing magnetic field model developed by *Tsyganenko* [1987], and a version of the *Donovan* [1993b] model in which parameters are determined specifically for the purposes of this thesis. In order to best specify the parameters in the Donovan model, it was necessary to conduct a careful study of geostationary magnetic field data. This study included the development of a method of data analysis in which the geostationary magnetic field measurements are transformed to remove seasonal effects, such that all data are consistent for a zero dipole tilt magnetic field configuration. I find from this study that the plane of the magnetotail current sheet may be significantly displaced from the magnetic equatorial plane near geostationary orbit even during quiet times. The quiet time magnetospheric magnetic field configuration was then modelled using the Donovan model in conjunction with the transformed data set. The magnetic field measurements during the substorm event are considered as perturbations from the quiet time magnetic field configuration, and the Donovan model adjusted to fit the specific substorm event.

The substorm event is studied using ground based magnetometer data, images

ages of the auroral oval recorded by the Viking satellite, and magnetic field and enegetic particle data from two geostationary satellites. It is found that significant perturbations can occur in the azimuthal component of the magnetic field at geostationary orbit which are due to movements of the large-scale field-aligned currents, rather than being a consequence of substorm current wedge formation. Auroral regions of discrete activity (as identified in the Viking images) are then mapped into the magnetotail. The model mappings differ from those done using the Donovan model. These differences may be attributed to the existence of "neutral regions" at the flanks of the Tsyganenko model magnetotail, and the lack of field-aligned current effects in the Tsyganenko model. The Donovan model maps the auroral activity along a line parallel to the Sun-Earth line in the magnetotail. This mapping suggests that the observed auroral activity is generated in an extended region of velocity shear, which stretches downtail along a locus lying between the dusk side magnetopause and the centre of the tail, but is well displaced from the noon-midnight meridian.

Acknowledgements

I am grateful to my supervisor, Gordon Rostoker, for his support and guidance throughout the course of my research, and for his patient and careful editing of the manuscript. Both he and John Samson have been excellent teachers, encouraging my interest in space physics.

I am also indebted to Eric Donovan for his determined efforts in performing the magnetic field modelling included in chapters 3 and 4, as well as his impromptu tutorial sessions, and last minute proofreading of the thesis.

Both Sherwood Botsford and Martin Connors have been invaluable sources of information about the computing systems; their patient explanations of various computing procedures have been helpful in advancing the progress of my research. I also acknowledge the Viking team for the Viking images and software used in chapter 4 of the thesis, and Gabrielle Deagle for producing the graphs in figures 55 and 61a.

I appreciate the friendship, conversation, and scientific discussions I have had the opportunity to share with many people within the space physics group: Karen Apps, Anna Belehaki, Sarah Derr, Eric Donovan, Martin Connors, Frances Fenrich, Christine Lesiak, John Manuel, Beth Tooley, Igor Voronkov, and Colin Waters. I also thank Jo-Anne Brown for her infectious enthusiasm, which prompted my introduction to the field of space physics.

Finally, I thank David Schwarz for unconditional support and encouragement, and my parents, Anne and John Skone, for their patience during the writing of this thesis and their continued enthusiasm and interest in all my endeavors, scientific and otherwise.

Table of Contents

page

1. Introduction: the Magnetosphere 1

    Solar Wind 1

    Solar-Terrestrial Interaction 5

  Magnetosphere Regions and Plasma Domains 10

    Boundary Regions (Plasma Mantle and Low Latitude Boundary Layer) 10

    Tail Lobe 11

    Plasma Sheet Boundary Layer 11

    Central Plasma Sheet 11

    Plasmasphere 13

  Magnetospheric Currents 15

    Magnetopause Current 15

    Ring Current 16

    Cross-tail Current 18

    Field-Aligned Currents 19

    Ionospheric Currents 21

    Solar Wind - Magnetosphere Dynamo 23

  Magnetospheric Substorms 28

    Near-earth Magnetotail Topology During Substorms and Associated Observations at Geostationary Orbit 34

    Ground Substorm Signatures 35

      Auroral Zone Stations 37

      Middle and Low Latitude Stations 38

Magnetic Field Modelling 42
Objectives of Thesis 44
2. Instrumentation and Data Acquisition 46
Ground Stations 46
Geostationary Satellites 52
Viking Imager 53
Using Viking Images to Study Auroral Activity 56
3. Establishing a Quiet Time Magnetospheric Magnetic Field
and Current Configuration 60
Requirements for Magnetic Field Modelling 60
A Survey of Quiet Time Data at Geostationary Orbit 62
The Nature of Seasonal and Diurnal Variations at
Geostationary Orbit 63
Development of the Data Set 70
Data Selection 71
Coordinate Transformation 73
Analysis of the Transformed Data Set 88
Quiet Time Current Configuration 96
Modelling the Quiet Time Current Configuration 100
4. Substorm Event 115
Event Overview 115
Near-Earth Magnetotail Signatures at GOES 5 and GOES 6 128
Nature of the Substorm Activity 138
Modelling the Substorm Magnetospheric Magnetic Field
and Current Configuration 142

Mapping the Auroral Intensifications into the Magnetosphere 155

5. Discussion and Conclusions 165

Discussion 165

Conclusions 171

Appendix A 172

Appendix B 176

Bibliography 179

List of Tables

table page

1. Typical parameters of the solar wind 7

2. Typical values of magnetotail parameters 14

3. Coordinates of North American ground magnetometer stations 49

List of Figures

figure page

1. Merging of the IMF with the Earth's dipole field 8

2. Cross-sectional illustration of the Earth's magnetosphere 9

3. The Chapman-Ferraro (magnetopause) current system 24

4. The ionospheric pattern of region 1 and region 2 field-aligned currents ...25

5. Nightside region 1 and region 2 field-aligned current closure in the magnetosphere 26

6. The configuration of high latitude electrojets and associated field-aligned currents 27

7. The large-scale auroral electrojets which characterize directly driven activity, and the substorm current wedge in the ionosphere 31

8. Auroral signatures during the various stages of substorm development ...32

9. An illustration of the substorm current wedge, which connects magnetotail current to the ionosphere 33

10. An illustration of the substorm current wedge magnetic field signatures, as observed at middle latitude ground stations and geostationary satellites located at different local time meridians 39

11. Theoretical latitude profile for a westward electrojet and associated field-aligned currents 40

12. Magnetic signatures associated with a substorm current wedge, as observed at auroral zone and low latitude stations 41

13. A map showing the array of Canadian ground magnetometer stations ... 50

14. Map of U.S. ground magnetometer stations 51

15. Schematic cross sections of the Viking camera and the image processing apparatus 58

16. An auroral intensification in the nightside auroral oval, as recorded by the Viking imager 59

17. VDH components of the magnetic field, as measured by GOES 6 in June and December, 1986 66

18. Hinging of the neutral sheet in the XZ_{gsm} plane 67

19. Dipole tilt angle as a function of the day of year 68

20. Projections of the neutral sheet configuration in the local HD and HV planes, at winter and summer solstices 69

21. A plot of the AE, AU, and AL indices for January 12, 1986 77

22. The distribution of low activity in 1986 78

23. An offset in the Hp magnetic field component, as measured by GOES 5 on October 12, 1986 79

24. An offset in the Hn magnetic field component, as measured by GOES 6 on April 27, 1986 80

25. Oscillations in the Hp magnetic field component, as measured by GOES 6 on November 19, 1986 81

26. A histogram showing the total number of one minute average magnetic field measurements (from both GOES 5 and 6) included in the GOES data set, per hour of local time 82

27. The geometry of the α angle calculation, in the local HV plane 83

28. Displacement of the neutral sheet from the magnetic equatorial plane, as a function of radial distance from the centre of the Earth to the position of the neutral sheet 84

29. Geometry of the calculation of R 85

30. Geometry of the calculation of the angle β, in the satellite local HD and VD planes at $R = 6.6R_E$ 86

31. Displacement of the neutral sheet from the magnetic equatorial plane, as a function of local time 87

32. Magnetic field angles of inclination as a function of distance from the neutral sheet, for nightside MLT sectors 91

33. Magnitude of the magnetic field as a function of distance from the neutral sheet, for nightside local time sectors 93

34. Angles of inclination, η_{VDH}, as a function of dipole tilt angle, for dayside local time sectors 16 to 18 MLT and 6 to 8 MLT 95

35. ΔB_X and ΔB_y as a function of perpendicular distance from the neutral sheet, for 18 to 20 MLT 103

36. Displacement of the neutral sheet from the magnetic equatorial plane resulting from a superposition of $\vec{B}_{terr}$ and $\vec{B}_{ext}$ 104

37. Displacement of the neutral sheet, and displacement of the central plane of current symmetry, from the magnetic equatorial plane as a function of radial distance 105

38. Displacement of the neutral sheet, and displacement of the central plane of current symmetry, from the magnetic equatorial plane as a function of local time 106

39. $\Delta B_{x'}$ as a function of distance from the central plane of current symmetry, and ΔB_x as a function of distance from the neutral sheet, for different nightside local time sectors 107

40. $\Delta B_{y'}$ as a function of distance from the central plane of current symmetry, and ΔB_y as a function of distance from the neutral sheet, for different nightside local time sectors 109

41. $\Delta B_{z'}$ as a function of distance from the central plane of current symmetry, for the local time sector 18 to 20 MLT 111

42. $\Delta B_{x'}$ and $\Delta B_{y'}$ as a function of local time for values of $z' = 0.5, 1.0$, and 1.5 R_E 112

43. $\Delta B_{z'}$ as a function of local time for $0.0 < z' < 1.8$ R_E 113

44. The distribution of ring and cross-tail currents in the XYgsm plane for the quiet time Donovan model 114

45. Magnetogram at Narssarssuaq, Greenland for 3 April, 1986 120

46. Viking images of auroral intensifications during the interval 0054 to 0100 UT on 3 April, 1986 121

47. Magnetogram at Fort Churchill for 3 April, 1986 122

48. Magnetogram at Poste de la Baleine for 3 April, 1986 123

49. Magnetogram at Fresno for 3 April, 1986 124

50. Magnetogram at Tucson for 3 April, 1986 125

51. Magnetogram at Fredericksburg for 3 April, 1986 126

52. Viking images of auroral intensifications during the interval 0114 to 0121 UT on 3 April, 1986 127

53. GOES 5 magnetic field measurements, in VDH coordinates, during the interval 0000 to 0300 UT on 3 April, 1986 133

54. GOES 6 magnetic field measurements, in VDH coordinates, during the interval 0000 to 0300 UT on 3 April, 1986 134

55. Latitude profiles for the Churchill line, at 0040 UT and 0050 UT, 3 April 1986 135

56. Particle flux at GOES 5, for electrons of energy $>$ 2 MeV, during the interval 0000 to 0300 UT on 3 April 1986 136

57. Particle flux at GOES 6, for electrons of energy $>$ 2 MeV, during the interval 0000 to 0300 UT on 3 April 1986 137

58. Magnetogram at Yellowknife for 3 April, 1986 140

59. The $B_{Z_{gsm}}$ component of the IMF, as measured at IMP 8, during the interval 0000 to 0300 UT, 3 April 1986 141

60. A plot of the Dst index during 0000 to 0300 UT, 3 April 1986 148

61. Churchill line latitude profile at 0054 UT on 3 April, 1986 149

62. Latitude profile for a westward electrojet and associated field-aligned currents, from *Kisabeth* [1972] 150

63. A model ionospheric potential, as calculated for enhanced activity levels from the Heppner-Maynard model 151

64. A plot of the Donovan model magnetic field values, as determined for the interval of substorm intensifications 0054 to 0116 UT, 3 April 1986 152

65. GOES 5 data for 3 April, 1986 compared with Donovan model values ..153

66. GOES 6 data for 3 April, 1986 compared with Donovan model values ..154

67. Images of the region of intensification in the auroral oval at ~ 0054 UT, and the 0116 UT surge, on 3 April 1986 160

68. Donovan model mappings of the substorm intensifications at 0054 and 0116 UT in the XY_{gsm} plane 161

69. T87 model mappings of the substorm intensifications at 0054 and 0116 UT in the XY_{gsm} plane 162

70. T87 mappings of circles of constant geomagnetic latitude, and lines of constant MLT, into the XY_{gsm} and YZ_{gsm} equatorial planes, for Kp=0,0+ and Kp=2,2+ 163

71. ΔB_D values, as calculated for the interval 0054 to 0116 UT on 3 April 1986 using the Donovan and T87 models 164

1. INTRODUCTION: THE MAGNETOSPHERE

The Earth's intrinsic magnetic field is dipolar, with the dipole axis inclined at an angle of ~ 11° from the Earth's rotation axis. The geomagnetic field is modified and distorted through electrodynamic solar-terrestrial interactions. The solar wind, a gas of charged particles flowing continuously from the Sun, is deflected by the geomagnetic field such that a magnetic cavity, called the magnetosphere, is formed around the Earth.

SOLAR WIND

The existence of a continuously flowing solar wind was first predicted by *Biermann* [1951], who studied observations of cometary tails. He determined that the Sun must emit a gas of outward streaming charged particles, in addition to electromagnetic energy, in order to explain the cometary tail features. The Sun consists of ~90 % Hydrogen, and ~10 % Helium. The outer layer of the Sun, the corona, is populated by ionized particles (mostly H^+), and extends into interplanetary space, pervading the entire solar system. The temperature at the base of the corona is several million degrees Kelvin, a local maximum, and decreases with distance outwards from the Sun.

Parker [1958] formulated a dynamic coronal model in which particles stream into space from the base of the corona. The solar wind expansion is similar to the flow of gas through a deLaval nozzle, which has maximum cross-sectional area at the two open ends. The ionized particles first approach a converging section of the nozzle (or, equivalently, a region of decreased flow speed and increased pressure and temperature at the base of the corona) and subsequently expand into a diverging section (where flow speed increases, and pressure and temperature decrease). The pressure ratio of upstream and downstream sections in the Sun is such that the ionized coronal particles are heated and energized, and the solar wind flow becomes supersonic and super-Alfvenic. Parker's solar wind model predicted values of the measurable parameters that were subsequently confirmed by spacecraft observations. Table 1 contains typical parameters of the solar wind at various distances from the Sun.

The solar wind has a Debye length, λ_D, of ~10 m [*Kavanagh*, 1972]. The plasma parameter is defined as $g = \frac{1}{N_D}$, where N_D is the number of particles in a Debye sphere:

$$N_D = \frac{4\pi n_o \lambda_D^3}{3}$$

$n_o \equiv$ density of ions/electrons

In the solar wind, $g << 1$ and the plasma approximation is therefore valid. Interparticle Coulomb and collisional forces can be neglected and the solar wind behaves like an electrically conducting fluid. Fluid dynamics deals with macroscopic phenomena and treats a collection of particles as a statistical ensemble. Magnetohydrodynamic (MHD) theory has been developed to deal specifically with magnetized ionized gases, such as the solar wind. The MHD momentum equation is given as follows:

$$\rho_m[\frac{\partial \vec{v}}{\partial t} + (\vec{v} \cdot \nabla)\vec{v}] = -\vec{\nabla} \cdot \tilde{p} + \vec{J} \times \vec{B} \qquad (1)$$

The macroscopic plasma parameters are (for a two species plasma such as the solar wind):

Centre of mass velocity:

$$\vec{v} = \frac{n_i m_i \vec{v_i} + n_e m_e \vec{v_e}}{n_i m_i + n_e m_e} \tag{2}$$

Pressure tensor:

$$\tilde{p} = \tilde{p_i} + \tilde{p_e} \tag{3}$$

Current density:

$$\vec{J} = n_i q_i \vec{v_i} + n_e q_e \vec{v_e} \tag{4}$$

Mass density:

$$\rho_m = n_i m_i + n_e m_e \tag{5}$$

where i, e subscripts denote the ion and electron species respectively. The full set of MHD equations and their derivations are given in *Nicholson*, [1983].

An "ideal MHD" approach is often used to study dynamic space plasma processes [*Newcomb*, 1958]. The ideal MHD approximation assumes infinite conductivity in a collisionless plasma. This assumption is valid in the solar wind. One consequence of this condition is

$$\vec{E} + \vec{v} \times \vec{B} = 0 \tag{6}$$

where $\vec{E} \equiv$ electric field, $\vec{B} \equiv$ magnetic field, and $\vec{v} \equiv$ solar wind bulk velocity. This relationship implies that 1. the magnetic flux through any loop moving with the plasma remains constant, and 2. plasma elements initially on a magnetic field line remain on that field line. The magnetic field appears "frozen" in the plasma flow.

Plasmas are often characterized by a β parameter which is the ratio of particle pressure to magnetic field pressure:

$$\beta = \frac{p}{(\frac{B^2}{2\mu_o})}$$

Cold, collisionless plasmas such as the solar wind, for which the ideal MHD assumption is valid, have $\beta << 1$.

The solar wind is a good electrical conductor, and its magnetic Reynold's number, $\mu_o \sigma L v$, is much greater than one, where $L \equiv$ characteristic spatial length of $\vec{B}$, $\sigma \equiv$ conductivity, and $v \equiv$ speed of the solar wind. The solar coronal magnetic field therefore diffuses slowly in the solar wind, and is convected outwards from the Sun (viz. frozen-in-field theorem). Near the Earth's orbit, this coronal field has been termed the interplanetary magnetic field (IMF). The solar wind magnetic field lines are curved in space, due to the rotation of the Sun, in which the IMF is anchored. The near-earth IMF makes an angle of ~45° with the Sun-Earth line; this is referred to as the garden-hose angle.

SOLAR-TERRESTRIAL INTERACTION

Dungey [1961] suggested that the interplanetary field lines merge with geomagnetic field lines at the dayside boundary of the magnetosphere, as in figure 1. The interconnected field lines are swept antisunward in the solar wind flow (as they are frozen into the moving solar wind plasma). The result is an open magnetic field configuration, called the *magnetosphere*, with a nightside *magnetotail*, in which high latitude field lines have one end anchored on the Earth and the other on the Sun. The Earth's magnetosphere is illustrated in figure 2. The boundary between the solar wind and the magnetosphere is, by convention, called the *magnetopause*. Upstream of the magnetopause, a dayside *bow shock* is formed in the supersonic solar wind flow. The solar wind plasma is compressed and thermalized behind the bow shock, and deflected around the geomagnetic field, forming the *magnetosheath*. Dayside closed field lines are separated from the open tail field lines by the *cusp*. Some open field lines are reconnected at a distant neutral line in the tail, with the associated magnetic field energy dissipated or injected back into the solar wind. In a steady state magnetosphere, the reconnection rate in the tail is approximately equal to the dayside merging rate [cf. *McPherron*, 1991]. *Perrault and Akasofu* [1978] derived an expression for input solar wind power:

$$\varepsilon = l_o{}^2 v_s B^2 \sin^4\frac{\theta}{2} \tag{7}$$

where

$v_s \equiv$ solar wind speed

$B \equiv$ magnitude of IMF

$\theta \equiv$ polar angle of the component of the IMF normal to the Sun-Earth line, and measured from the northward geomagnetic axis

$l_o \equiv$ a constant with the dimensions of length

The entry of energy into the magnetosphere is enhanced when the value of θ approaches 180° (i.e. the IMF becomes increasingly antiparallel to the geomagnetic field). A northward turning of the IMF is usually accompanied by a release of energy from the magnetotail into the ionosphere. Approximately ninety percent of energy transport from the solar wind into the magnetosphere occurs through reconnection [*Baumjohann and Haerendel*, 1986]. The remaining ten percent of solar wind-magnetosphere energy transfer takes place through viscous interaction at the low latitude magnetosphere boundaries [*Baumjohann and Haerendel*, 1986].

r/r_0	1.03	1.5	10	215
$n(\mathrm{m}^{-3})$	2×10^{14}	1.6×10^{13}	4×10^{9}	7×10^{3}
T (° K)	1.7×10^{6}	10^{6}	4×10^{5}	4×10^{4}
B (Teslas)	10^{-4}	0.5×10^{-4}	10^{-6}	5×10^{-9}
v (m/s)	0.6×10^{3}	3×10^{3}	3×10^{5}	4×10^{5}

Table 1. Typical parameters of the solar wind, at varying distances from the Sun, where $r_0 \equiv$ radius of the Sun, n $\equiv$ density of ions/electrons, T $\equiv$ temperature, B $\equiv$ magnetic field strength, v $\equiv$ velocity of solar wind, and $\frac{r}{r_0} = 215$ is the Sun-Earth distance. $r_0 \sim 7 \times 10^8$ m.(values taken from [*Parks*, 1991]).

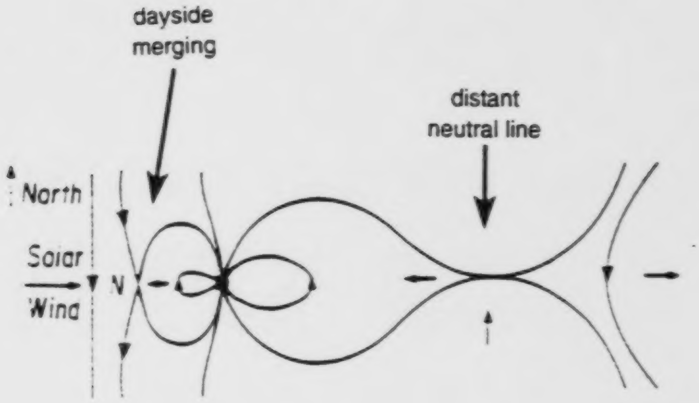

Figure 1. Merging of the IMF with the Earth's dipole field, in the XZ_{gsm} plane. Dayside geomagnetic field lines merge with the IMF and are swept into the magnetotail. Reconnection of these field lines takes place at the distant neutral line.(as adapted from *Dungey*, 1963).

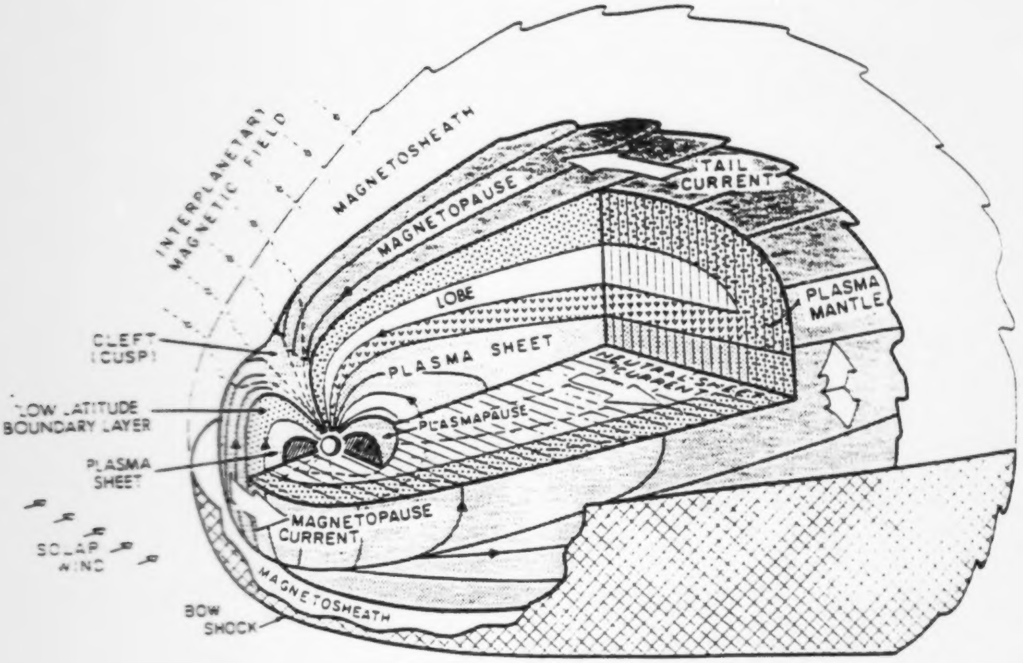

Figure 2. A cross-sectional illustration of the Earth's magnetosphere, and regions therein. [*Rostoker*, 1989]

MAGNETOSPHERE REGIONS AND PLASMA DOMAINS

An open magnetosphere configuration allows for entry of the solar wind plasma across the magnetopause. Plasma of either solar wind or ionospheric origin pervades the entire magnetosphere. It is convenient to classify different regions of the magnetosphere by their distinct plasma properties. The different regions are labelled in figure 2, and the characteristics of plasmas in each region are given in table 2.

BOUNDARY REGIONS (PLASMA MANTLE AND LOW LATITUDE BOUNDARY LAYER)

A small amount of the magnetosheath plasma (≤ 1 % [cf. *Lui*, 1987]) crosses the magnetopause. One such entry region is the cusp, where the magnetic field is weak and the ideal MHD approximation breaks down such that solar wind plasma may enter the magnetosphere. The penetrating plasma may reach low altitudes before being reflected in the stronger near-earth magnetic field and retreating tailward in the *plasma mantle*, a region of high latitude open field lines. Solar wind plasma also penetrates the *low latitude boundary layer* (LLBL), a region of closed field lines along the flanks of the tail. The LLBL is a turbulent region, characterized by significant vorticity and velocity shear. Solar wind energy and momentum are transported into the magnetosphere at this boundary [*Axford and Hines*, 1961; *Miura*, 1984; *Manuel*, 1993] via viscous interaction. The plasma properties in the plasma mantle and LLBL are similar to those of the adjacent magnetosheath plasma.

TAIL LOBE

The tail lobes are regions of open field lines bounded by the plasma mantle and plasma sheet boundary layer at high and low latitudes respectively. Particle densities are lowest, and the magnetic field strongest, in this region of the magnetosphere. Energy density is therefore dominated by the magnetic field contribution ($\beta < 1$). The particle population consists of ions from the cusp region, and some electrons of solar wind origin.

PLASMA SHEET BOUNDARY LAYER

The Plasma Sheet Boundary Layer (PSBL) borders the tail lobes at their low latitude edge. This is a region of anisotropic plasma, characterized by rapidly flowing field-aligned ion beams (H^+, O^+) [*Fairfield*, 1987], and a β lower than that of the neighboring central plasma sheet. *Eastman et al.* [1984] propose that these ions are accelerated from a region of weak magnetic field near the neutral line, towards the Earth, by Speiser acceleration mechanisms [*Speiser*, 1965]. The ions are then mirrored in the stronger low altitude fields and accelerated tailward.

CENTRAL PLASMA SHEET

The central plasma sheet (CPS), located at the core of the tail, contains only closed field lines. This region extends from $\sim$ 6.5 R_E [*Lui*, 1975] to $\sim$ 50 R_E [*Rostoker and Skone*, 1993], and is bounded at the flanks by the LLBL. The CPS is thinner near midnight and becomes thicker towards the flanks of the tail [*Bame et al.*, 1967]. A neutral sheet lies in the central plane of this region, across which the magnetic field reverses direction (from sunward to antisunward). The magnetic field is weakest in the neutral sheet plane (generally on the order of a few nT beyond ~ 12 R_E downtail [*Rostoker and Skone*, 1993]). The CPS is populated by plasma particles of solar wind and ionospheric origin. The plasma is isotropic, and has β values ranging from .3 near the upper and lower boundaries, to 20 – 30 [*Baumjohann et al.*, 1989] in the neutral sheet. Typically, a spacecraft moving from the lobe regions to the CPS will encounter earthward streaming beams, followed by counterstreaming beams and isotropic plasma sheet distributions. Based on this, *Eastman et al.* [1984] propose that the PSBL is a source of the energetic CPS plasma.

The motion of the solar wind with respect to the Earth's magnetic field creates a quasi-static electric field in the magnetotail. This electric field is directed from dawn to dusk across most of the CPS. Guiding centre theory predicts a drift velocity which is the sum of gradient, curvature and "$\vec{E} \times \vec{B}$" drifts:

$$\vec{v}_D = \frac{mv_\perp^2}{2qB^3}(\vec{B} \times \vec{\nabla} B) + \frac{mv_\parallel^2}{qB^4}[\vec{B} \times (\vec{B} \cdot \vec{\nabla})\vec{B}] + \frac{\vec{E} \times \vec{B}}{B^2} \tag{8}$$

The guiding centre approximation is reasonable in most of the CPS, with the exception of the neutral sheet. In the ideal MHD, "cold" plasma, approximation the gradient and curvature terms are negligible. Plasma sheet particles are not necessarily cold, however. Ion energies are ~5 keV [*Huang and Frank*, 1986], and electron energies are ~ 1 keV [*Lui* 1987]. For particles of energy ~ 10 keV, the gradient and curvature drifts become of comparable importance to the "$\vec{E} \times \vec{B}$" term [cf. *Hines*, 1963]. Ions (electrons) in the CPS therefore experience gradient and curvature drifts parallel (antiparallel) to the electric field. These particles are adiabatically heated as they move across equipotentials. The "$\vec{E} \times \vec{B}$" drift causes particles to also convect earthwards.

Neutral sheet particles experience similar energization. Dawn-dusk drifts in this region may result from Speiser type orbits [*Speiser*, 1965] if the magnetic field radius of curvature is small and the magnetic field weak (such that MHD approximation is not valid), and particles undergo nonadiabatic heating. Large-scale magnetotail currents arising from particle drifts are discussed in a later section.

Individual particles also undergo bounce motion along field lines, conserving the first adiabatic invariant. Some particles precipitate into the high latitude ionosphere while others continue to drift earthwards, and eventually populate the radiation belt. Individual particle behavior depends on the particle's equatorial pitch angle. Inside of ~ 8 R_E there exists a "trapped" particle population of ionospheric and solar wind origin [*Lyons and Williams*, 1984].

PLASMASPHERE

The plasmasphere, located earthward of the CPS, is a region of cold (≤ 1 eV) [cf. *Lyons and Williams*, 1984] ionospheric ions and electrons. The particles are in diffusive equilibrium and corotate with the Earth. A "corotational electric field" is induced in this region such that the equipotentials form closed surfaces around the Earth. The plasmapause corresponds to the outermost closed equipotential and is located between ~ 3 and ~ 4 R_E [*Parks*, 1991].

	Magnetosheath	Plasma mantle	Tail lobe	Plasma sheet boundary layer	Central plasma sheet	Neutral sheet
number density (cm^3)	5	1	10^{-2}	10^{-1}	5 x 10^{-1}	1
ion temperature (K)	10^6	10^6	10^6	10^7	5 x 10^7	5 x 10^7
electron temperature (K)	5 x 10^5	5 x 10^5	5 x 10^5	5 x 10^6	10^7	10^7
magnetic field (nT)	5	25	25	20	10	2
electric field (mV/m)	1	1	10^{-1}	10^{-1}	10^{-2}	10^{-2}
Debye length (m)	1.8 x 10^1	4.0 x 10^1	4.0 x 10^2	4.0 x 10^2	2.8 x 10^2	2.0 x 10^2
plasma skin depth (m)	2.4 x 10^3	5.3 x 10^3	5.3 x 10^4	1.7 x 10^4	7.5 x 10^3	5.3 x 10^3
electron gyroradius (R_E)	4.9 x 10^{-4}	9.8 x 10^{-5}	9.8 x 10^{-5}	3.9 x 10^{-4}	1.1 x 10^{-3}	5.5 x 10^{-3}
ion gyroradius (R_E)	3.0 x 10^{-2}	5.9 x 10^{-3}	5.9 x 10^{-3}	2.3 x 10^{-2}	1.0 x 10^{-1}	5.2 x 10^{-1}
electron gyrofrequency (Hz)	1.4 x 10^2	7.0 x 10^2	7.0 x 10^2	5.6 x 10^2	2.8 x 10^2	5.6 x 10^1
ion gyrofrequency (Hz)	7.6 x 10^{-2}	3.8 x 10^{-1}	3.8 x 10^{-1}	3.0 x 10^{-1}	1.5 x 10^{-1}	3.0 x 10^{-2}
electron plasma frequency (Hz)	2.0 x 10^4	9.0 x 10^3	9.0 x 10^2	2.8 x 10^3	6.3 x 10^3	9.0 x 10^3
ion plasma frequency (Hz)	4.7 x 10^2	2.1 x 10^2	2.1 x 10^1	6.6 x 10^1	1.5 x 10^2	2.1 x 10^2
ion sound speed (km/s)	8.3 x 10^1	8.3 x 10^1	8.3 x 10^1	2.6 x 10^2	3.7 x 10^2	3.7 x 10^2
Alfven speed (km/s)	4.9 x 10^1	5.5 x 10^2	5.5 x 10^3	1.4 x 10^3	3.0 x 10^2	4.4 x 10^1
electron thermal speed (km/s)	2.8 x 10^3	2.8 x 10^3	2.8 x 10^3	8.7 x 10^3	1.2 x 10^4	1.2 x 10^4
ion thermal speed (km/s)	9.1 x 10^1	9.1 x 10^1	9.1 x 10^1	2.9 x 10^2	6.4 x 10^2	6.4 x 10^2
convection speed (km/s)	2.0 x 10^2	4.0 x 10^0	4.0 x 10^0	5.0 x 10^0	1.0 x 10^0	5.0 x 10^0
thermal/magnetic energy ratio	6.9 x 10^0	5.6 x 10^{-2}	5.6 x 10^{-4}	8.7 x 10^{-2}	8.8 x 10^0	4.3 x 10^2
magnetic energy density (J m^{-3})	9.9 x 10^{-18}	2.5 x 10^{-16}	2.5 x 10^{-16}	1.6 x 10^{-16}	4.0 x 10^{-17}	1.6 x 10^{-18}

Table 2. Typical values of parameters in various regions of the Earth's magnetotail. (values taken from *Lui* [1987]).

MAGNETOSPHERIC CURRENTS

The magnetospheric configuration is supported by four large-scale current systems: magnetopause, ring, cross-tail, and field-aligned currents. To study these large-scale phenomena, it is convenient to invoke MHD theory. The plasma parameters in various magnetosphere regions can be calculated from table 2 values. The plasma parameter, g, is less than 10^{-9} in current carrying regions, and the particles may be treated as a plasma.

MAGNETOPAUSE CURRENT

The existence of magnetopause currents was first suggested by *Chapman and Ferraro* [1930]. These currents are induced at the boundary between the solar wind and the geomagnetic field and serve to shield the Earth's magnetic field in the main body of solar wind plasma. The position of the magnetopause, and hence the shape of the magnetosphere, is determined by pressure balances. The fluid and electromagnetic stresses at the magnetopause are balanced so that (cf. equation 1)

$$0 = -\vec{\nabla} p_{sw} + \vec{J}_{mp} \times \vec{B}_{mp} \tag{9}$$

where $\vec{J}_{mp} \times \vec{B}_{mp}$ is the electromagnetic stress vector, and the solar wind pressure is approximated as a scalar:

$$p_{sw} \sim K n_{sw} m_p v^2 \sin^2\theta$$

where

$K \equiv$ a constant measuring how efficiently the solar wind particles' momentum transfers to the magnetosphere

$n_{sw} \equiv$ number density

$m_p \equiv$ proton mass

$v \equiv$ bulk velocity

$\theta \equiv$ angle between the solar wind velocity and the tangent to the magnetopause surface.

The solar wind magnetic pressure is neglected (typically small in comparison to the kinetic contribution [cf. *Siscoe*, 1987]), as is the thermal contribution (T ~ 50-100 eV [*Parks*, 1991]). From equation 9, it follows that

$$\vec{J}_{mp} = \frac{\vec{B}_{mp} \times \vec{\nabla} p_{sw}}{B_{mp}^2} \tag{10}$$

The magnetopause current is therefore diamagnetic. It arises from the partial gyration motions of protons and electrons at the magnetopause. This current system consists of two eddy currents, one in each hemisphere, centred about the cusps. The currents flow counter-clockwise in the northern hemisphere, and clockwise in the southern hemisphere, and are illustrated in figure 3.

RING CURRENT

The ring current arises from drift motions of trapped particles in the inner magnetosphere, and from gyrational motions of these particles in the inhomogeneous magnetic field. This current flows around the Earth in the azimuthal direction, perpendicular to the magnetic field. A steady state expression for $\vec{J}_{\perp}$ (the current density perpendicular to the magnetic field) can be derived from the MHD momentum equation [*Vasyliunas*, 1984] or, equivalently, is derived from single particle drifts using the first-order guiding centre approximation [*Parker*, 1957]:

$$\vec{J}_\perp = \frac{\vec{B} \times \vec{\nabla} p_\perp}{B^2} + \frac{p_\parallel - p_\perp}{B^2} \vec{B} \times [(\hat{b} \cdot \vec{\nabla})\hat{b}] + \frac{\rho_m}{B^2} \vec{B} \times (\vec{v} \cdot \vec{\nabla} \vec{v}) \qquad (11)$$

where $p_\perp, p_\parallel \equiv$ components of particle pressure perpendicular and parallel to the magnetic field respectively, and all other quantities are defined in equations 2 through 5.

The above expression describes a current derived from four particle motions: gyromotion (term1), gradient and curvature drifts (term 2), and inertial drifts (term3). The inertial current is small relative to the diamagnetic current in the ring current region [*Sato*, 1982]. *Lui et al.* [1987] found that the diamagnetic current dominated over the curvature current during periods of enhanced activity. The ring current is therefore caused primarily by pressure gradients in the trapped particle population. The particle population consists of terrestrial ions ($\mathrm{He}^{++}, \mathrm{O}^{+}$) as well as protons of solar wind origin [*Lundin et al.*, 1980] which have been convected earthward in the CPS. The pressure increases with radial distance out to approximately 3 $\mathrm{R_E}$, at which point the pressure gradient becomes negative [*Lui et al.*, 1987]. The results of *Lui et al.* [1987] are consistent with the existence of an eastward ring current out to 3 $\mathrm{R_E}$, and a stronger westward ring current from approximately 3 to at least 8 $\mathrm{R_E}$.

CROSS-TAIL CURRENT

The formation of a magnetotail requires the existence of a current flowing from dawn to dusk in the tail region. Such a current causes the magnetic field to be weaker in the near-earth neutral sheet, and field lines to be inclined at smaller angles to the magnetic equatorial plane than for a purely dipolar configuration. This magnetic field topology is said to be *taillike.* *Williams and Mead* [1965] first modelled a cross-tail current, confined to the neutral sheet, in order to explain the magnetotail magnetic field configuration. Later models of the tail current include that of *Olson and Pfitzer* [1974] who allowed for a cross-tail current at distances 3 R_E above and below the neutral sheet, in addition to cross-tail currents in the neutral sheet plane. Such a model was found to fit reasonably well to observed magnetic field values. The cross-tail current can generally be described by equation 11, except in the neutral sheet. The diamagnetic term is dominant in equation 11 in all but the outer central plasma sheet region [*Sato*, 1982]. As mentioned previously, MHD theory is not necessarily valid in the neutral sheet, and the motions of particles in this plane must therefore be considered in terms of Speiser orbits and drifts. Such drifts also contribute to a dawn-dusk current in the tail. The cross-tail current closes through magnetopause currents flowing dusk to dawn over the tail lobes.

In the near-earth magnetotail, at radial distances of approximately 6.5 to 8 R_E, the ring current region and the CPS overlap. In this region, trapped particle drifts contribute to the ring current and less energetic plasma sheet particle motions contribute to the tail currents. The net current comprises both azimuthal and radial components such that the radius of current curvature is different than that for a purely azimuthal flow.

FIELD-ALIGNED CURRENTS

Birkeland [1908] first suggested a three-dimensional current system where ionospheric currents are linked to the magnetosphere by currents flowing along magnetic field lines. The pattern of field-aligned current in the topside ionosphere was studied initially by *Boström* [1964] who determined, from theoretical considerations, that field-aligned currents may "feed" high latitude ionospheric current systems. Later observational studies include those of *Zmuda and Armstrong* [1974] and *Iijima and Potemra* [1978]. Figure 4 shows the ionospheric location of region 1 and 2 field-aligned currents .

The poleward currents flow into the ionosphere on the dawn side and away from the ionosphere on the dusk side. This is the "region 1" [*Iijima and Potemra*, 1976] system. The "region 2" currents are located equatorward of region 1, and are of opposite polarity. *Yasuhara et al.* [1975] determined that region 1 currents are generally stronger than those of the region 2 system, as did *Iijima and Potemra* [1979]. Region 1 and 2 currents flow into and out of a region of the ionosphere where auroral phenomena take place. This region of enhanced conductivity is known as the auroral oval [*Feldstein and Starkov*, 1967]. The nightside oval is believed to map to the CPS [*Lassen*, 1974], where particles experience bounce motions and may enter the loss cone and precipitate into the ionosphere.

Hasegawa and Sato [1979] derived an expression for the field-aligned current, $J_{\|}$, from the condition

$$\vec{\nabla} \cdot \frac{1}{\mu_o}(\vec{\nabla} \times \vec{B}) = \vec{\nabla} \cdot \vec{J} = 0$$

$$\Rightarrow \vec{\nabla} \cdot \vec{J}_{\perp} = -\vec{\nabla} \cdot \vec{J}_{\|}$$

and, using the MHD expression for $\vec{J}_\perp$ (cf. equation 11), found

$$\vec{J}_\parallel = B\int[\frac{\rho}{B}\frac{d}{dt}(\frac{\Omega}{B}) + \frac{2}{B^2}\vec{J}_\perp \cdot \nabla B + \frac{1}{\rho_m B}\vec{J}_{in} \cdot \nabla\rho]dl_\parallel \qquad (12)$$

where

$$\vec{J}_{in} = -(\frac{\rho_m}{B^2})(\frac{d\vec{v}}{dt} \times \vec{B})$$

and

$$\Omega = (\vec{\nabla} \times \vec{v}) \cdot \vec{B}$$

The presence of the vorticity term, Ω, suggests that generation mechanisms for field-aligned currents operate in regions of the magnetosphere where there are oppositely directed plasma flows or velocity shears, such as the LLBL and near-earth CPS.

Kan [1987] also derived an expression (steady state) for $\vec{\nabla} \cdot \vec{J}_\perp$ and identified the near-earth CPS as the main "response" region of region 2 currents, and dynamo regions (LLBL, PSBL) as the main "source" of region 1. *Kan* [1987] determined that the region 1 currents may be generated on open field lines (PSBL) and closed field lines in the antisunward flow region of the CPS (LLBL) by plasma pressure gradients and magnetospheric convection respectively. Additionally, *Sato* [1982] determined that vorticity in the LLBL may support region 1 currents. *Sato* showed that vorticity is directly proportional to the amount of space charge or, equivalently, directly proportional to the divergence of the electric field. *Goertz and Boswell* [1979] demonstrated that the initiation of an electric field divergence, across a magnetic field line, results in the propagation of an Alfven wave. The wavefront supports an electric field parallel to the magnetic field, and a steady state current may be established along the magnetic field line. Currents in the region 1 sense have also been detected in the PSBL by *Fairfield* [1973] and *Ohtani et al.* [1988]. *Zanetti et al.* [1991] have determined that the divergence of equatorial currents in the near-Earth CPS, and ring current regions, is of the region 2 sense.

The closure of region 1 and 2 currents in the magnetosphere has not been determined conclusively. *Ohtani et al.* [1990], *Iijima et al.* [1990], and *Zanetti et al.* [1991] have studied the magnetospheric closure of field-aligned currents during levels of disturbed activity. They determined that region 2 currents may close through an azimuthal westward current in the near-earth tail. *Ohtani et al.* [1990] proposed also that region 1 and 2 currents close through radial tail currents, as shown in figure 5.

IONOSPHERIC CURRENTS

Ionospheric currents flow in a region 100-150 km altitude above the Earth. At this altitude, the particles are primarily of terrestrial origin and densities (density of neutrals $\sim 2 \times 10^{18}$ m^{-3}, [cf. *Cole et al.*, 1965]) are large enough that collisions cannot be ignored. Current flows can therefore be described by Ohm's law:

$$\vec{J} = \tilde{\sigma} \cdot (\vec{E} + \vec{v} \times \vec{B}) \tag{13}$$

where the conductivity, $\tilde{\sigma}$, is a tensor. Ionospheric conductivity is anisotropic and currents flow in directions both parallel and perpendicular to the ionospheric electric field. From Ohm's law, an expression for $\vec{J}_\perp$ can be derived:

$$\vec{J}_\perp = \Sigma_P \vec{E}_\perp + \Sigma_H \hat{b} \times \vec{E}_\perp \tag{14}$$

where Σ_P and Σ_H are the Pedersen and Hall height-integrated conductivities respectively, and $\hat{b}$ is a unit vector in the direction of the magnetic field $\vec{B}$ [*Boström*, 1964].

Harang [1946] established the location of large-scale east-west ionospheric currents at auroral zone latitudes. These currents, called electrojets, occupy a high latitude region colocated with the auroral oval, and flow from noon to midnight across the dawn and dusk meridians, as shown in figure 6. The eastward electrojet flows across dusk, while a stronger westward electrojet flows across dawn, penetrating into the evening sector through midnight. Both electrojets are present near midnight, where they are separated by the "Harang discontinuity" [*Heppner*, 1972]. The electric field in this auroral region is directed primarily poleward (equatorward) in the eastward (westward) electrojet regions. The electrojets are therefore primarily Hall currents.

The electrojets are colocated with the auroral oval, and are components of a three-dimensional current system which includes field-aligned currents. Downward field-aligned current diverges into the ionosphere near noon and flows into the electrojets [*Hughes and Rostoker*, 1977]. Some electrojet current diverges up field lines at the dawn and dusk terminators. Most of the electrojet current, however, flows into the evening sector where it diverges into a region of net upward field-aligned current [*Rostoker*, 1992]. The field-aligned current serves to couple the electrojets to the magnetosphere.

SOLAR WIND - MAGNETOSPHERE DYNAMO

The flow of ionospheric Pedersen currents is accompanied by energy dissipation such that $\vec{J} \cdot \vec{E} > 0$. A dynamo process, in which energy supplies the Pedersen current circuit, is therefore required. Since Pedersen currents are the ionospheric component of a current system which includes field-aligned currents, the dynamo process must involve field-aligned current generation in the magnetosphere. As discussed previously, region 1 field-aligned currents are thought to be generated in the LLBL and PSBL. Solar wind flow along the magnetopause provides an obvious energy source. Energy may be transferred to the magnetosphere from the solar wind via the generation of region 1 field-aligned currents. The concept of a solar wind - magnetosphere dynamo is therefore invoked to describe many magnetospheric processes. It is not necessary, however, that current systems extend into the solar wind in order to derive energy. The solar wind interaction may energize plasma in the CPS by less direct interactions. Dynamo currents include the ionospheric, field-aligned, cross-tail, and magnetopause current systems.

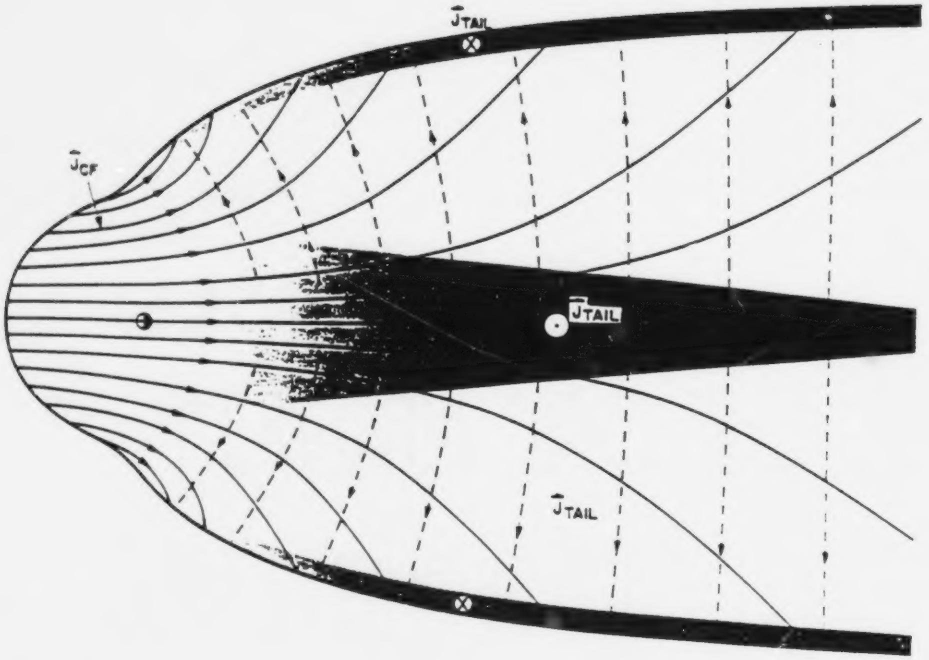

Figure 3. The Chapman-Ferraro (magnetopause) current system, $\vec{J}_{CF}$, and the tail currents, $\vec{J}_{tail}$, as projected into the XZ_{gsm} plane. [*Axford et al.*, 1965]

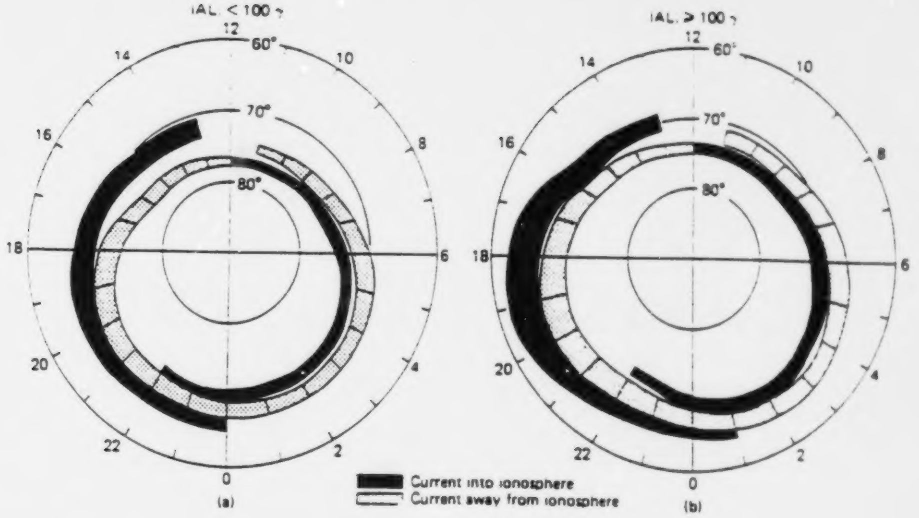

Figure 4. The ionospheric pattern of region 1 and region 2 field-aligned currents. Region 1 consists of current into (out of) the ionosphere in the post (pre) midnight sector. Region 2 consists of current into (out of) the ionosphere in the pre (post) midnight sector. The field-aligned current pattern is shown for both average (|AL| < 100 nT) and disturbed (|AL| > 100 nT) conditions. [*Iijima and Potemra*, 1978]

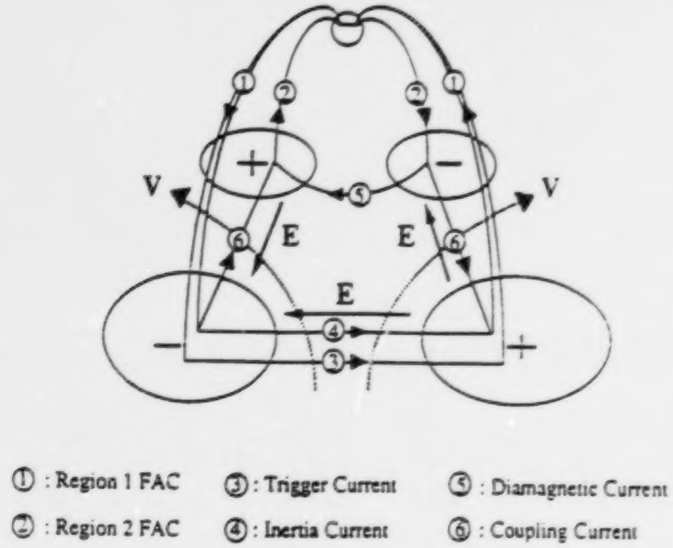

Figure 5. Nightside region 1 and region 2 field-aligned current closure in the magnetosphere. Region 2 currents close via an azimuthal equatorial current in the near-earth region. Region 2 currents also close with region 1 currents via radial currents in the dawn and dusk sectors. [*Ohtani et al.*, 1990]

Figure removed due to copyright restrictions.

Figure 6. The configuration of high latitude electrojets and associated field-aligned currents. Downward field-aligned current diverges into the east and west electrojets near noon. The electrojets converge into a region of net upward field-aligned current near midnight. [*Hughes*, 1978]

MAGNETOSPHERIC SUBSTORMS

Akasofu [1964] introduced the concept of an auroral substorm. He observed an intensification of the most equatorward arc in the midnight sector oval, followed by the development of a bright bulge. The westward edge of the bulge appeared to expand poleward and westward; this was interpreted as the evolution of a "westward travelling surge". The original concept of an auroral substorm was later expanded on and *Akasofu* [1968] proposed the concept of a "magnetospheric substorm", which stressed an involvement of the entire magnetosphere, including the magnetotail, in substorm phenomena. *Rostoker et al.* [1980] defined a magnetospheric substorm to be "a transient process initiated on the nightside of the Earth in which a significant amount of energy derived from the solar wind-magnetosphere interaction is deposited in the auroral ionosphere and in the magnetosphere".

It is believed that the auroral signatures associated with a substorm are caused by two distinct components of activity: a directly driven process, and an explosive "loading-unloading" process [*Rostoker et al.*, 1987]. The directly driven system is characterized by the auroral electrojets and region 1 and region 2 field-aligned currents. These currents are driven by the solar wind-magnetosphere dynamo. The dynamics of this system are such that input energy from the solar wind is dissipated in the ionosphere and inner magnetosphere with no intermediate storage in the magnetotail over and above the Alfvenic transit time from the boundary layer to the ionosphere. *Akasofu* [1979] calculated the power of the solar wind-magnetosphere dynamo using the *Perrault and Akasofu* [1978] ε parameter (defined in equation 7). He found that input solar wind power is approximately equal to the total power dissipation in the inner magnetosphere and ionosphere, for $l_o \sim 7\ \mathrm{R_E}$. Variations in directly driven electrojet strength, in direct response to changes in the solar wind, take place over a time scale of hours (as in figure 7a).

During substorms, short explosive periods of energy dissipation occur. These are characteristic of the "unloading" process which features a current wedge. This wedge consists of a three-dimensional current system: two oppositely directed sheets of field-aligned current, separated in longitude, are closed through a longitudinally localized westward current in the auroral ionosphere. This current system has a lifetime of $\sim$ 10-20 minutes (as in figure 7b). Unlike the directly driven system, where energy from the solar wind continuously drives large-scale ionospheric currents, the "loading-unloading" process requires a storage of magnetic energy in the magnetotail. This energy is then released, or "unloaded", through an internal instability in the magnetosphere, or by external triggering. Energy released in this process is also deposited in the ring current region.

There are three stages of substorm development: growth phase [*McPherron*, 1970], expansive and recovery phases [*Akasofu*, 1968]. Each phase is defined by distinct auroral and magnetospheric signatures. Figure 8 illustrates the substorm development in the auroral oval. The first two frames depict the growth phase. Energy is being deposited in the magnetosphere, through enhanced dayside merging, during a period of enhanced southward IMF. Dayside magnetic field lines are interconnected with the IMF and swept over the poles, into the tail. Magnetic flux is transported to the nightside and tail lobe flux increases. The polar cap, a region of primarily open field lines, grows in size and the auroral oval shifts equatorward. Part of the input solar wind energy during this phase is stored in the tail as magnetic field energy, while part of the energy is dissipated directly in the magnetosphere, through the directly driven process. The electrojets increase in strength, as do the field-aligned currents [*Iijima and Potemra*, 1979]. Short lived surges may be observed at the poleward edge of the oval during this phase; these have been termed pseudo-breakups [*Akasofu et al.*, 1966].

Frame 8d shows the oval shortly after the onset, which is the beginning of the expansive phase, where auroral activity is known to be initiated on field lines threading the equatorward edge of the oval near the midnight [*Samson et al.*, 1992]. This phase is characterized by the substorm current wedge [*McPherron et al.*, 1973] (figure 9) which may be considered as the sum of a series of wedgelets [*Wiens and Rostoker*, 1975] that are caused by the sudden release of stored magnetic field energy in the tail (viz. unloading process). The upward field-aligned wedge current appears as a bright surge in the auroral oval. This phase may feature multiple surges and intensifications, which are interpreted as the development of a westward travelling surge, as first identified by *Akasofu* [1964]. A northward turning of the IMF, and a corresponding decrease in the rate of energy entering the magnetosphere, often occurs just before the expansion phase onset. Frame 8e shows the beginning of the recovery phase, where the oval recedes poleward and returns to its quiet-time configuration.

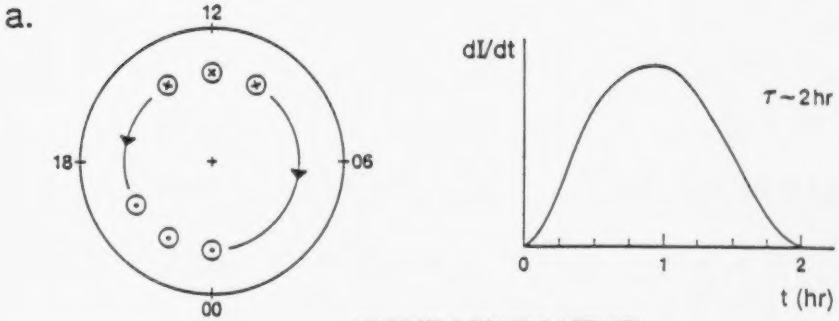

"DIRECTLY DRIVEN" ACTIVITY

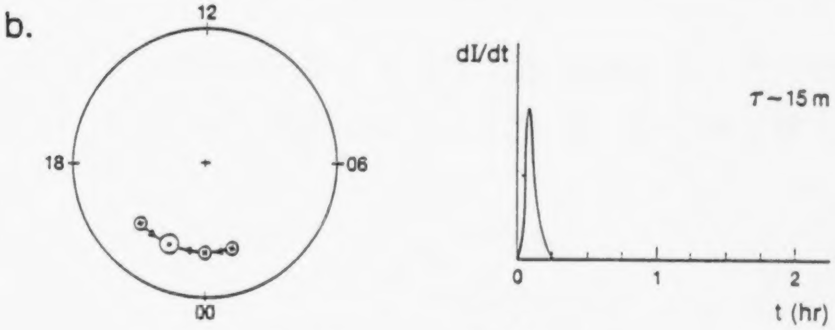

ACTIVITY AS A CONSEQUENCE OF "RELEASE" PROCESS

Figure 7a. The large-scale auroral electrojets which characterize directly driven activity. The impulse response time of these currents is several hours for an increase in energy input into the magnetosphere.

b. A substorm current wedge in the ionosphere. The localized region of intense upward field-aligned current appears as surge in the auroral oval. This type of current system has a lifetime of $\sim$ 15 minutes. [*Rostoker*, 1991]

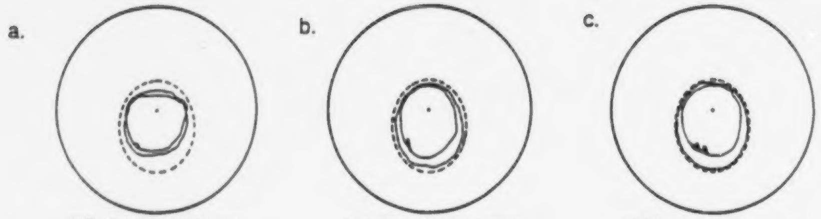

a. IMF after being northward for some time has just turned southward

b. Oval expands equatorward under influence of southward IMF

c. IMF has just turned northward

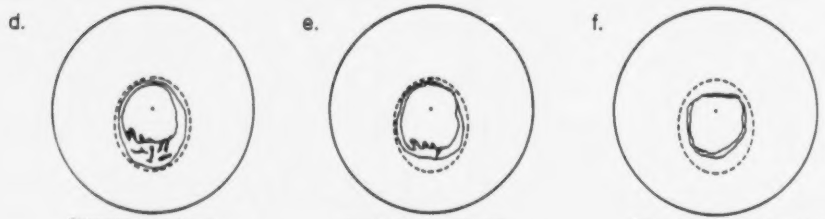

d. Poleward edge of oval expands poleward and features multiple surges. Bright structures seen within diffuse evening auroras

e. Surge action at poleward edge of oval continues as diffuse auroras recede poleward

f. Return to quiet oval about 1hr after IMF northward turning

Figure 8. Auroral signatures during the various stages of substorm development. The first two frames depict the substorm growth phase, while an expansive phase onset takes place in frame d. [*Rostoker*, 1991]

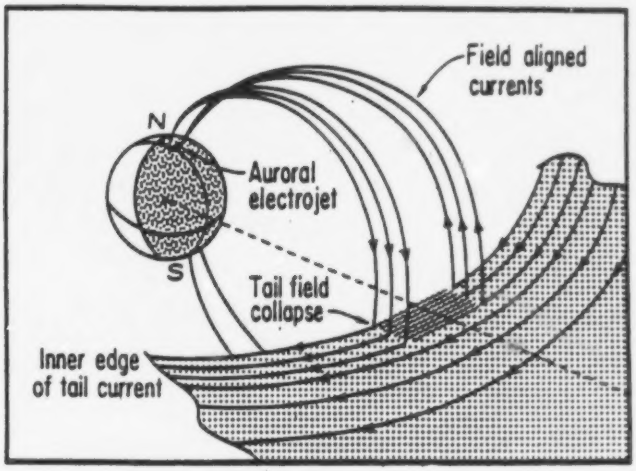

Figure 9. An illustration of the substorm current wedge. The wedge is formed by a diversion of cross-tail current in the magnetotail which closes via the westward electrojet in the nightside ionosphere. [*Clauer and McPherron*, 1974]

NEAR-EARTH MAGNETOTAIL TOPOLOGY DURING SUBSTORMS AND ASSOCIATED OBSERVATIONS AT GEOSTATIONARY ORBIT

The position of "geostationary orbit" is at 6.6 R_E radial distance, and is therefore near the average position of the inner edge of the plasma sheet on the nightside. Observations at geostationary orbit provide insight into the storage and release of magnetotail energy during a substorm.

During the substorm growth phase, the magnetic field at geostationary orbit becomes more taillike [*Lui*, 1978; *Sauvaud and Winckler*, 1980] and there is a thinning of the plasma sheet [*Hones et al.*, 1984] in the near-earth magnetotail. The antisunward stretching of field lines is consistent with a growth of cross-tail current in the near-earth magnetotail, normally just beyond geostationary orbit. In order to account for observations, *Kauffman* [1987] determined this current intensification must take place $\sim 7 - 10$ R_E downtail. There is also a decrease in the flux of energetic particles at geostationary orbit [*McIlwain*, 1974; *Baker*, 1984]. *Sauvaud and Winckler* [1980] attributed this decrease to an earthward shift of trapped particles, resulting from the field distortion.

The tail field at geostationary orbit recovers to a more dipolar configuration at substorm expansive phase onset [*Cummings et al.*, 1968; *McPherron*, 1972; *Kokubun and McPherron*, 1981], indicating an unloading of stored magnetotail energy. This is accompanied by an expansion of the plasma sheet [*Hones et al.*, 1984] in the near-earth magnetotail, and an injection of energetic particles near geostationary orbit [*Baker*, 1984].

The current reduction may be explained as a diversion of part of the cross-tail current along field lines into the ionosphere [*McPherron et al.*, 1973; *Lui*, 1978; *Kauffman*, 1987]. The diverted tail current forms the substorm current wedge, in which the upward field-aligned current sheet appears as a westward travelling surge in the ionosphere. This wedge is illustrated in figure 9. *Ohtani et al.* [1988] suggested that the field-aligned currents of the substorm wedge originate inside of 15 R_E downtail, implying that the energy release takes place in the near-earth magnetotail.

Nagai [1982] studied ground and geostationary magnetic field data, and determined that the wedge expands azimuthally. Figure 10 shows the magnetic field variations at geostationary orbit associated with the substorm current wedge expansion. The geostationary measurements are expressed in the VDH coordinate system which is described in appendix A. In this coordinate system, the H component is directed antiparallel to the dipole axis, while D is directed eastwards. A dipolarization (increase in H) is measured by the satellites at meridians B and C in figure 10 at expansive phase onset, indicating that these meridians are inside the substorm current wedge. Meridians A and D, however, are initially outside the wedge, as evidenced by the field becoming more taillike at these meridians after onset. Dipolarizations occur at meridians A and D minutes after onset as the wedge expands east and west from the onset sector. Positive (negative) perturbations in the D component at a given satellite meridian indicate that the meridian is west (east) of the centre of the current wedge.

GROUND SUBSTORM SIGNATURES

Ground stations are classified as polar cap, auroral zone, middle latitude, and low latitude. The criteria for classification generally depends on the latitude of the station. For the purposes of this thesis, the following definitions, which allow stations to be classified according to the nature of phenomena observed, will be used:

1. "Polar cap"defines the region of open field lines thought to map to the tail lobe. One expects no auroras in the polar cap ionosphere, as the only particle precipitation into the polar cap is polar rain.

2. "Auroral zone" defines the auroral oval region of closed field lines mapping to the tail plasma sheet and the boundary layers. One expects auroral luminosity and significant electrical conductivity in the auroral oval in regions of upward field-aligned current and at the edges of regions of downward field-aligned current. As stated previously, this region is threaded by region 1 and region 2 field-aligned currents and is the site of the auroral electrojets.

3. "Middle latitude" defines a region equatorward of the auroral oval but poleward of the projection of the plasmapause on the ionosphere. This is a region in which the magnetic effects of the auroral currents are confined to edge effects of the auroral electrojets (primarily in the vertical component of the perturbation magnetic field) and the effect of field-aligned, ring and tail currents. There is no significant particle precipitation into the middle latitude ionosphere and therefore no significant ionospheric conductivity in the nighttime hours.

4. "Low latitude" defines a region equatorward of the projection of the plasmapause on the ionosphere. It is a region affected geomagnetically only by the field-aligned, ring, and tail currents. Near the geomagnetic equator (latitude $< 5°$), the equatorial electrojet may lead to enhanced horizontal (northwards) and vertical magnetic field perturbations at the surface of the Earth.

Ground stations located near the equatorward edge of the oval fall into an ambiguous category. Depending on the nature of the activity, these stations may be auroral zone (as for an equatorward movement of the oval during substorms) or middle latitude (during periods of average activity). It is necessary to classify ground stations according to the predominant effects observed, which may change with activity level.

Auroral Zone Stations

As noted previously, the electrojets become stronger during substorm activity. The strength and latitudinal extent of the electrojets can be inferred from magnetic field measurements at ground stations in the auroral zone. Latitude profiles may be used to display the measurements of many stations located along a common meridian. Magnetic field values from quiet periods are subtracted from the disturbed values. This is necessary in order to subtract the effects of all but the enhanced electrojets and associated currents. The profile is constructed by plotting the magnetic field components as a function of the latitude of the observing station, where only stations located approximately on a common meridian are included in the profile. Figure 11 is a theoretical profile for a westward electrojet. The magnetic field components in this profile are represented in the HDZ coordinate system. Ground based magnetic field measurements are often expressed in HDZ coordinates, and this coordinate system is described in appendix A. The latitude profile in figure 11 includes the effects of field-aligned currents which close the electrojets in the magnetosphere. The centre of the jet is at the latitude where the H component has maximum magnitude, and the boundaries of the jet may be approximated as the latitudes where the magnitude of Z is maximum.

The presence of a substorm wedge at onset may also be detected from magnetic field measurements on the ground. Figure 12 illustrates the magnetic field variations at auroral zone stations due to a current wedge, for observatories located north and south of the westward electrojet associated with the surge. A sudden decrease in the H component is observed with the arrival of the surge at the observatory meridian. This is accompanied by a decrease (increase) in Z if the observatory is south (north) of the surge.

Middle and Low Latitude Stations

Magnetic variations observed at middle latitude stations are dominated by the effects of field-aligned currents. *Kokubun and McPherron* [1981] found a strong correlation between H variations at geostationary orbit and those at middle latitude stations on the same meridian. This correlation is interpreted as the station observing the effects of the substorm current wedge. Figures 10 and 12 show signatures at middle and low latitude stations located at various longitudes with respect to the onset sector. These signatures differ from those in the auroral zone in that the H perturbation is dominated by the effects of field-aligned current sheets, not the westward electrojet. A positive H perturbation occurs at middle or low latitude stations located inside the substorm current wedge.

Low latitude stations may also observe a large scale depression in the H component during periods of enhanced auroral activity. This corresponds to a growth in the symmetric ring current. The H depression lasts many hours and is thus distinguishable from variations due to the substorm wedge. The Dst index (see appendix B) is derived from measurements of H at low latitude observatories; this index is used as an indicator of ring current strength.

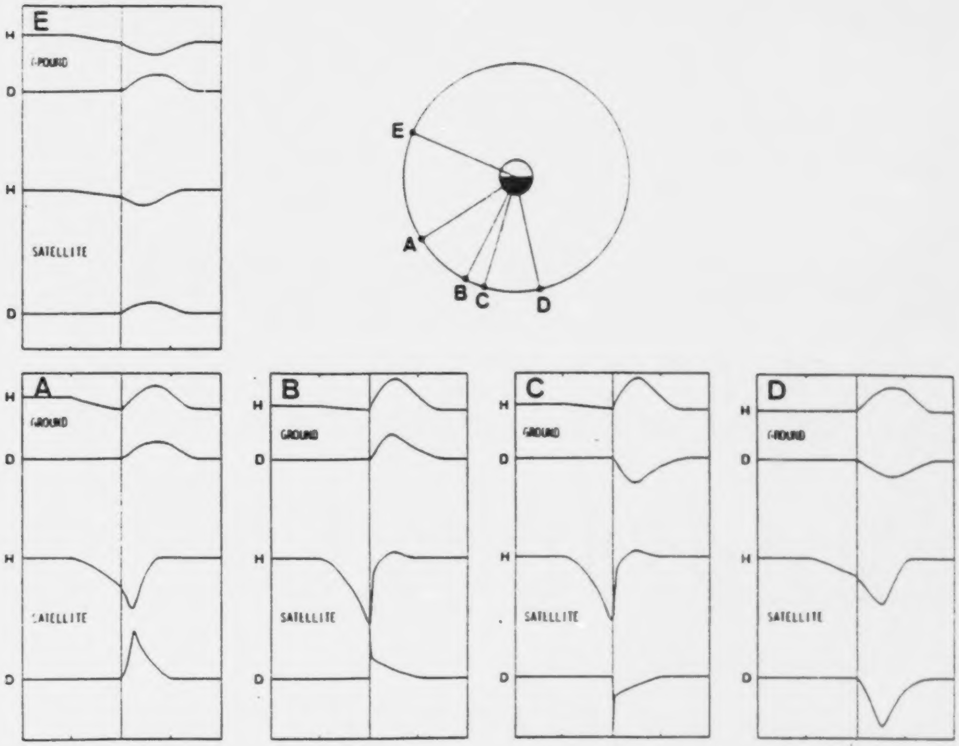

Figure 10. An illustration of the substorm current wedge magnetic field signatures, as observed at middle latitude ground stations and geostationary satellites located at different local time meridians. The ground measurements are expressed in HDZ coordinates, while the satellite measurements are expressed in VDH coordinates. Both of these coordinate systems are described in appendix A. The vertical line in each graph represents the time of onset, and an explanation of the magnetic signatures is given in the text. [*Nagai*, 1982]

Figure removed due to copyright restrictions.

Figure 11. Theoretical latitude profile for a westward electrojet, as calculated for a three dimensional current system which includes field-aligned currents. The meridian of observation for this profile is west of the central meridian of the electrojet, such that the D component is dominated by effects of the upward field-aligned current. [*Kisabeth*, 1972]

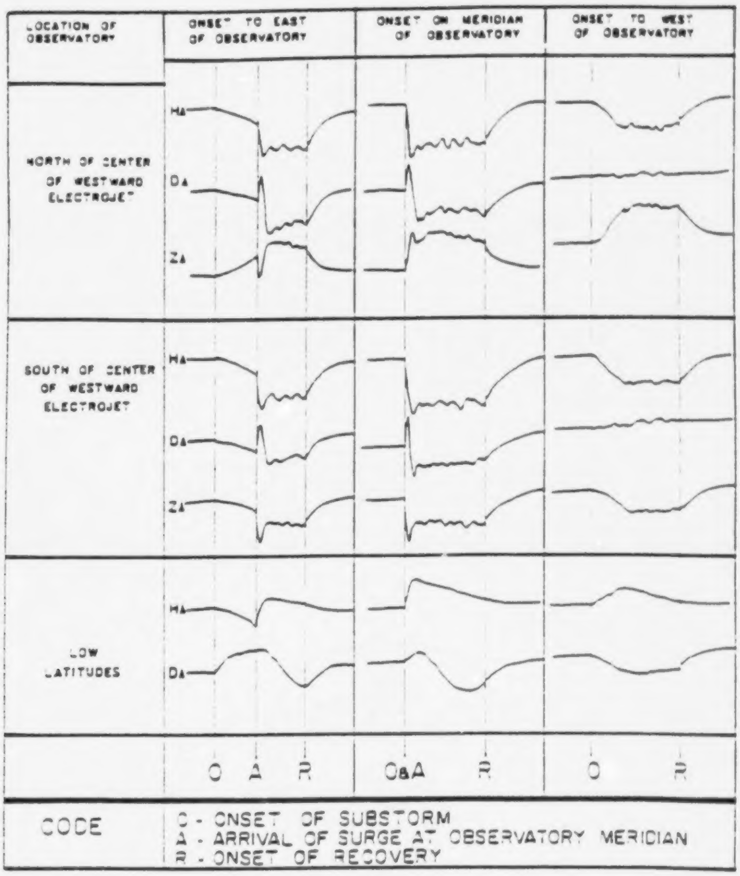
LOCATION OF OBSERVATORY
ONSET TO EAST OF OBSERVATORY
ONSET ON MERIDIAN OF OBSERVATORY
ONSET TO WEST OF OBSERVATORY
NORTH OF CENTER OF WESTWARD ELECTROJET
SOUTH OF CENTER OF WESTWARD ELECTROJET
LOW LATITUDES
H△
D△
Z△
O A R
O&A R
O R
CODE
O - ONSET OF SUBSTORM
A - ARRIVAL OF SURGE AT OBSERVATORY MERIDIAN
R - ONSET OF RECOVERY

Figure 12. Magnetic signatures associated with a substorm current wedge, as observed at auroral zone and low latitude stations located at different meridians and latitudes with respect to the wedge. An explanation of the signatures is given in the text. [*Rostoker et al.*, 1980]

MAGNETIC FIELD MODELLING

Auroral phenomena are a manifestation of magnetospheric and ionospheric processes. The magnetosphere-ionosphere coupling is achieved via field-aligned currents. In order to obtain a better understanding of auroral phenomena, it is necessary to identify magnetospheric source regions of field-aligned currents. This may be achieved by invoking an accurate magnetic field model and tracing the field lines from the ionosphere outwards. Most existing magnetic field models are empirical, e.g. [*Olson and Pfitzer*, 1974], [*Mead and Fairfield*, 1975], [*Tsyganenko*, 1987] (referred to as T87), [*Tsyganenko*, 1989] (referred to as T89). These models have been developed by fitting functions to a set of magnetic field observations made at various locations in the magnetosphere.

An empirical magnetic field model consists of a sum of vector functions

$$\vec{B}_{model}(\vec{R}) = \Sigma_{i=1}^{N} \vec{f}_i(\lambda_i^1, ..., \lambda_i^{M_i}; \vec{R}) = \vec{B}_{terrestrial} + \vec{B}_{external} \tag{15}$$

Most often, models use the International Geomagnetic Reference Field (IGRF) [*IAGA Commission 2, working group 4*, 1969] as the terrestrial field contribution. The Tsyganenko models are the most widely used representations of the magnetic field due to external currents. They represent the magnetospheric external field with contributions due to a model ring current and cross-tail current, as well as a polynomial function representing all other current sources. According to *Tsyganenko* [1987], the polynomial contains the magnetopause and field-aligned current contributions to the total field. *Donovan* [1993a], however, has shown that field-aligned currents are not present in the T87 model. In fairness, all that can be said is that the polynomial allows for a better fit to the data than would be possible with only model ring and cross-tail currents included in the model.

Fairfield [1991] compared the T87 model with observed magnetic field values at distances within 17 R_E of the Earth. He found that there was generally a good agreement between the model and observations. He noted, however, that there was a lack of adequate field line stretching in the tail and ring current regions, and that using the magnetic activity index Kp (see appendix B) to parameterize the model is not adequate. *Jordan et al.* [1992] found T89 to be a good representation of the average field in the inner magnetosphere. Both T87 and T89, however, have large deficiencies in regions further from the Earth. *Donovan et al.* [1992] noted that there are regions of negative Bz in the T89 model neutral sheet at distances greater than 20 R_E downtail. As well, *Rostoker and Skone* [1993] demonstrated that for both T87 and T89, B_{zgsm} in the neutral sheet is significantly smaller than observations in regions 15 - 40 R_E downtail. Thus, both Tsyganenko models underestimate the magnetic flux crossing the neutral sheet in this region of the magnetotail, and this has serious implications for mappings done using these models in the magnetotail.

Deficiencies in the Tsyganenko models arise because the models' functions are not consistent (via Ampere's law) with realistic magnetospheric currents. The model is a fit of these functions to a large but finite data set, such that they accurately represent the magnetic field in the regions where measurements were made. However, because the functions do not correspond to realistic currents, unrealistic magnetic field values are produced in at least some regions of the magnetosphere where model magnetic field values are not specified by measurements. *Donovan* [1993b] has developed a magnetic field model using large numbers of current elements. These current elements have a finite density everywhere, unlike the wire segments used in previous current based models [i.e. *Olson and Pfitzer*, 1974]. It was the intention of *Donovan* to create as realistic a current configuration as possible, and then alter parameters in order to fit the model field to measured properties of the actual field. Both the T87 model and Donovan models will be used in this thesis.

OBJECTIVES OF THESIS

The ultimate objective of this thesis is to perform mappings of auroral forms into the magnetosphere and, in doing so, gain insight into the physics of the magnetotail mechanisms responsible for the auroral displays. Most members of the space science community perform such mappings using either the T87 or T89 magnetic field models. These models, however, are known to have some deficiencies; these were outlined in the introductory section on modelling and will be discussed in greater depth in further sections of the thesis. An alternative approach to mapping is therefore conducted in this thesis, using the Donovan model.

The approach taken with the Donovan model requires a specification of parameters describing the magnetospheric current configuration at the time of the auroral intensifications. In order to best specify such parameters, a study of geostationary data is included as part of this thesis, with the objective of characterizing the magnetic field at geostationary orbit. The near-earth region close to geostationary orbit is of particular interest during substorm events: it is believed that an enhancement of the cross-tail current takes place in this region during substorm growth phase, with a subsequent disruption of the current occuring at expansive phase onset. A careful survey of geostationary magnetic field data is therefore conducted as part of this thesis, with the intention of best specifying parameters describing the magnetospheric current configuration, and hence magnetic field configuration, in the Donovan model during the substorm event.

A large part of this thesis is devoted to modelling using the Donovan model. This approach to modelling differs from that taken in developing the Tsyganenko models and inevitably some comparisons may be made about the relative effectiveness of the two approaches. Any discrepancies between the Donovan and Tsyganenko mappings of auroral activity may be interpreted as a reflection of inherent differences between the two models. It is not necessarily an objective of this thesis however, nor is it possible within the scope of the one substorm event studied in this thesis, to draw any conclusions as to which is the better magnetic field model. It is the intention in this thesis to use both models, mindful of their inherent differences, to gain insight into the magnetospheric source regions of auroral substorm activity.

2. INSTRUMENTATION AND DATA ACQUISITION

Sources of data for this thesis include ground stations, geostationary satellites, and an ultraviolet imager aboard a high altitude satellite. This chapter contains descriptions of the instrumentation, and discussions of data handling. All measurements were made during 1986.

GROUND STATIONS

Magnetometer data from both Canadian and U.S. ground stations are considered in this thesis. The observatories provide auroral zone and sub-auroral measurements at locations shown in figures 13 and 14. The geographic and geomagnetic coordinates of the U.S. and Canadian stations are given in table 3.

An array of magnetometer stations extends from ~55° N to ~85° N geomagnetic latitude. Resolute, Baker Lake, Eskimo Point, Fort Churchill, Gillam, and Glenlea lie on, or near, a common geomagnetic meridian. These stations form the "Churchill line", and latitude profiles are constructed from measurements made at stations along this line. The North American magnetometer array also covers ~70° of longitude. Measurements made by individual stations, located at different meridians, may be used to determine the apparent motion and longitudinal extent of a substorm wedge.

The Canadian stations, with the exception of Eskimo Point and Gillam, are operated by Energy, Mines and Resources Canada. These stations are equipped with an automatic magnetic observatory system (AMOS). This system consists of a triaxial fluxgate magnetometer, which measures X,Y,Z magnetic field components in the geographic coordinate system, and a proton precession magnetometer which measures the total scalar field intensity, F. The reader is referred to appendix A for descriptions of the geographic coordinate system and all other coordinate systems that are referred to in this chapter. The values of X,Y,Z, and F are processed through two filtering algorithms. The first filtering process determines 10 second samples, and the second filter averages seven such sample values, centred at one minute intervals. Each one minute average is multiplied by a correction factor:

$$\frac{F}{(X^2 + Y^2 + Z^2)^{\frac{1}{2}}}$$

A correction baseline value is also added to the one minute averages, in order to compensate for changes in the level and azimuth of the fluxgate assembly. Edited one minute averages are recorded, and eventually stored on microfilm in a reconstituted analog format. In order to better manipulate the data, it was necessary to digitize the microfilm magnetograms. The digitization process resulted in some inaccuracies. Errors below ~ 2 nT (for Ottawa, St. John's, and Victoria) or ~ 5 nT (at all other stations) were not detectable, as limited by the resolution of the analog data. The digitized X, Y, and Z magnetic field components were rotated into the geomagnetic coordinate system (as outlined in appendix A). Geomagnetic coordinates are preferred because the auroral oval and associated activity are centred about the geomagnetic dipole pole.

Eskimo Point and Gillam are part of the CANOPUS array, and are equipped with triaxial fluxgate magnetometers that have a sensitivity of 1/40 nT. Magnetic field measurements are expressed in digital form, in geographic coordinates, and are calculated as 5 second averages, constructed from 8 Hz samples. The magnetic field components at these stations were rotated into geomagnetic coordinates for use in this thesis.

The U.S. stations are operated by the USGS (United States Geological Survey). Each station is equipped with a triaxial fluxgate magnetometer. The fluxgate sensors are oriented with axes aligned in the H, D, and Z local magnetic directions. Each station also has a proton precession magnetometer which measures the total magnetic field intensity, F. The H, Z, and F components are measured in nT (with a resolution of .1 nT), while D is measured in minutes of arc (with a resolution of .1 minute of arc). Values are recorded as one minute averages. The H, D, and Z values were transformed into geomagnetic coordinates. This required first resolving H into the horizontal X and Y geographic directions. The X, Y, and Z components were then rotated into geomagnetic coordinates (as outlined in appendix A).

Table 3a. Canadian ground stations.

Station name and code		Geomagnetic		Geographic	
		lat (degrees N)	long (degrees E)	lat (degrees N)	long (degrees E)
Alert	(AL)	86.24	163.08	82.50	297.50
Baker Lake	(BL)	73.67	319.15	64.33	263.97
Cambridge Bay	(CB)	76.77	299.13	69.10	255.00
Eskimo Point	(EP)	70.78	324.73	61.10	265.93
Fort Churchill	(FC)	68.53	326.12	58.80	265.90
Gillam	(GI)	66.11	326.54	56.40	265.30
Glenlea	(GL)	59.19	326.06	49.63	262.90
Meanook	(MN)	61.88	304.02	54.62	246.67
Mould Bay	(MB)	79.62	259.89	76.30	240.60
Ottawa	(OT)	56.37	354.11	45.40	284.45
Poste de la Baleine	(PB)	66.21	350.32	55.30	282.25
Resolute Bay	(RB)	83.14	295.98	74.70	265.10
St. John's	(SJ)	57.19	23.39	47.60	307.32
Victoria	(VI)	54.33	295.66	48.52	236.58
Yellowknife	(YL)	69.14	296.56	62.47	245.53

Table 3b. U.S. ground stations.

Station name and code		Geomagnetic		Geographic	
		lat (degrees N)	long (degrees E)	lat (degrees N)	long (degrees E)
Fresno	(FRN)	43.50	304.30	36.73	299.78
Fredericksburg	(FRD)	49.13	352.23	38.20	282.63
Tucson	(TUC)	40.37	314.57	32.25	249.17

Table 3. The geographic and geomagnetic coordinates of the Canadian and U.S. array of ground magnetometer stations.

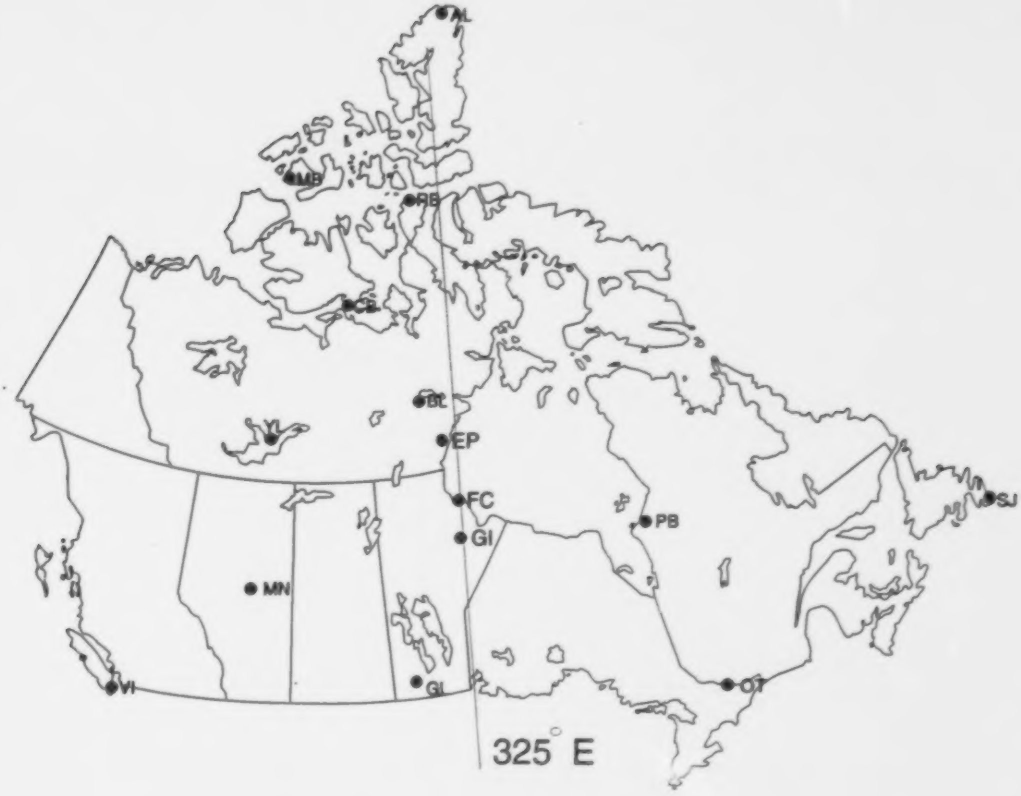

Figure 13. A map showing the array of Canadian ground magnetometer stations. Stations located along the 325° E geomagnetic meridian form the Churchill line. The full names of each station, along with their geographic and geomagnetic coordinates, are given in table 3.

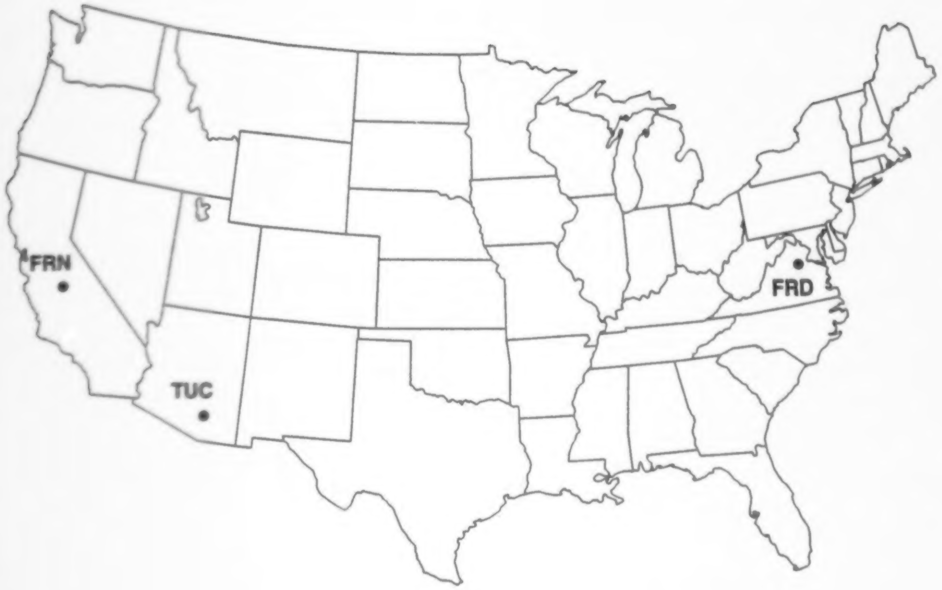

Figure 14. Map of U.S. ground magnetometer stations used in this thesis. The full names of each station, along with their geographic and geomagnetic coordinates, are given in table 3.

GEOSTATIONARY SATELLITES

Two Geostationary Operational Environmental Satellites (GOES) operated in the Earth's geographic equatorial plane, at a radial distance of 6.6 R_E, during 1986. GOES 5 was located within a few degrees of 75° W (geographic) and GOES 6 was located at 100° W (September through November) or 108° W (during the remainder of the year). GOES 5 was therefore positioned near the longitude of Poste de la Baleine, at the eastern edge of Hudson's Bay. GOES 6 was located 14 (September through November), or 6 (during the remainder of the year), degrees of longitude from the Yellowknife meridian. Both satellites were in excellent positions to make observations of magnetotail activity corresponding to ground signatures. The magnetic latitude was approximately 11° for GOES 5, and 10° (September through November) or 9° (during the remainder of the year) for GOES 6. Both satellites carried instrumentation to measure magnetic, energetic particle, and soft x-ray data.

Magnetic field measurements were made in the (Hp, He, Hn) coordinate system. Hp is parallel to the satellite spin axis, which is itself perpendicular to the satellite's orbital plane. He is parallel to the satellite-Earth centre line and points earthward. Hn is perpendicular to both Hp and He, and points eastward. Measurements of the field components were made by a twin-fluxgate spinning sensor which is sensitive to field strength changes as small as .2 nT. The magnetometer sampled the field every .75 seconds. Four consecutive samples were considered in each recorded measurement such that the low and high values are thrown out and the remaining two averaged. The GOES magnetic field data considered in this thesis are one minute averages, produced from these 3-second measurements. The magnetic field components are rotated from the satellite local coordinate system into (V, D, H) cylindrical coordinates. H is antiparallel to the geomagnetic dipole axis, V lies parallel to the magnetic equatorial plane, and is directed radially outwards from Earth, and D is in the direction of $\vec{H} \times \vec{V}$ (positive eastward). The rotation from (Hp, He, Hn) to (V, D, H) coordinates is described in appendix A. A detailed study of GOES data, and a discussion of the proper coordinate system in which to represent the data, are given in chapter 3. It is important to note that the GOES data contain offsets. The nature of these offsets, and their removal from the data set, will also be discussed in chapter 3.

VIKING IMAGER

The Viking satellite, launched in February, 1986, was produced in a multinational collaborative effort, under the guidance of the Swedish Space Corporation. The satellite was developed in order to investigate physical processes in the high latitude, medium height (1-2 R_E) region. Details of the project are outlined by *Hultqvist* [1987]. The satellite operated at an inclination of 98.8°, with an altitude between 817 km (perigee) and 13530 km (apogee), and an orbital period of 262 minutes.

Energetic electrons (which have been accelerated along field lines) precipitate into the ionosphere, and the resulting emission of visible and UV radiation can be detected optically. The Viking satellite was equipped with an imager in order to make measurements of this auroral luminosity. The imager was developed so as to be sensitive to vacuum UV wavelengths exclusively. The effects of solar emissions and atmospheric reflectivity are low in these wavelengths; aurora can thus be seen with good contrast on both the dark and sunlit sides of the Earth. The imager contained two different cameras, identical except in passband: camera 0, with a wavelength passband of 1345 - 1800 Å; camera 1, with a wavelength passband of 1235 - 1600 Å. Camera 0 responded mainly to the Lyman-Birge-Hopfield (LBH) bands of N2, and camera 1 was predominantly sensitive to the 1304 Å OI band. It was hoped that the relative intensities and spatial distributions of LBH and OI emissions would provide information on the precipitating electrons. Camera 1 only operated for 3 months, however, and its data will not be used in this thesis. Emissions measured by the imager cameras take place at various heights. The 1304 Å OI band emissions take place between 200-300 km above the surface of the Earth, while the LBH emissions occur in the height range $\sim$ 140-180 km [*S. Murphree, private communication*].

The Viking project sought to develop instrumentation with increased temporal and spatial resolution over satellites which had operated previously in this region of space (such as S3-3, DE-1). This motivated the use of CCD technology in construction of the imager cameras. Detailed descriptions of the camera design and its components are given by *Anger et al.* [1987]. A short discussion of the optical system will be given here. Essentially, each camera processed images via a microchannel plate (MCP), fibre optic bundles, and a CCD array, as shown in figure 15a.

An Inverse Cassegrain Burch system [*Burch*, 1947], as shown in figure 15b, produces an initial image at the MCP. The Burch system consists of two concentric mirrors, oriented such that a spherical image is formed at the conformal surface of the MCP. Angular distortion of the image is therefore minimized. The MCP surface is covered with a photocathode material from which electrons are released and form an electron image at the surface of the fibre optic bundle. Photons are then released from the phosphor surface of the bundle and travel along the straight fibres, entering the distortion corrector. This corrector is a tapered fibre optic bundle which serves to map the spherical image onto a flat CCD array. An intensified, distortion-free image is then produced at the CCD plate.

Each element of the CCD array essentially functions as a capacitor. The net charge accumulated in each capacitor site (or pixel) is proportional to the number of incident photons. The image stored in the CCD plate is read by applying a voltage across the array. This causes charge to flow across the array to a point where the data are read row by row. The camera exposure time is 1s, and the satellite completes one spin every 20s. In order to counteract the effect of the satellite spin, which causes the image to move across the array, the image data were clocked across the array at the same rate that the image moved. In order to facilitate the correction process, the CCD columns were aligned with the spacecraft equatorial plane, to within 0.2°.

The CCD array contained 288 × 385 pixels. Images telemetered to the ground consisted of 2 × 2 pixel (superpixel) averages such that each average value represented between $20 \times 20\ km^2$ (perigee) and $70 \times 70\ km^2$ (apogee) of the ionosphere. Image intensities were measured in units of DN, the telemetered signal per superpixel. The field of view of the camera was 20° × 25°, with an angular resolution of .076° × .076°, as limited by the pixel size. The Viking satellite design allowed for real-time analysis of imager data at the ground station. Scientists also had interactive control of the spacecraft. It was therefore possible to make the best use of the imager field of view. The CCD exposure could be triggered at any point in the spacecraft spin, or the field of view shifted. Consecutive images could thus be obtained over entire periods of substorm expansive phase development. It was possible to obtain images every 20s, but the interval between images was generally closer to one minute.

USING VIKING IMAGES TO STUDY AURORAL ACTIVITY

In order to study the images in the context of substorms, it is necessary to determine an exact relation between auroral forms seen from the ground and data measured by the imager. *Vallence Jones et al.* [1987] studied Viking observations of auroral displays in conjunction with simultaneous observations from a CANOPUS meridian scanning photometer. They calculated calibration factors which related the UV intensity to auroral intensity observed on the ground at optical wavelengths. The factor varied over the visible spectrum wavelengths: 14 ± 2 DN/kR for 5577 $\mathring{A}$, and 60 ± 10 DN/kR for 4278 $\mathring{A}$.

Akasofu [1964] defined an auroral substorm in terms of visible signatures. The DN/kR calibration factors directly relate UV intensities to visual intensities There are, however, no defined UV thresholds corresponding to visual substorm observations. Figure 16 is a Viking image of an intensification in the nightside auroral oval during a period of enhanced activity. The colour bar varies linearly from 0 to 255 DN (left to right). *Kidd and Rostoker* [1991] defined a surge, in the context of Viking images, as a localized structure exceeding 180 DN. Generally, oval intensifications at substorm onset exceed 250 DN. Surge structures with similarly high intensities, however, have been observed in Viking images prior to ground detected onsets [*Elphinstone et al.*, 1991]. Viking data alone cannot be used to identify substorm activity. It is best to also study simultaneous ground and satellite measurements, in conjunction with the images. Imager observations may then be considered in the context of substorm activity, as inferred from the ground and satellite signatures. In this thesis, events have been selected in which auroral activity (as identified in the images) takes place over North America. This ensures the availability of simultaneous ground and satellite measurements in the sector of enhanced activity.

Murphree et. al. [1991] outline some limitations of the satellite auroral images. They note that individual discrete arcs can have widths much less than the minimum spatial resolution of the imager. This leads to uncertainties in the location and nature (discrete or diffuse aurora) of the activity. Temporal uncertainties also exist. The time interval between images limits identification of exact timings, such as substorm onset. It also important to note that auroral luminosity is caused by the precipitation of electrons into the ionosphere. Brighter regions are therefore areas of enhanced upward field-aligned current, and do not necessarily represent the full extent of a substorm wedge.

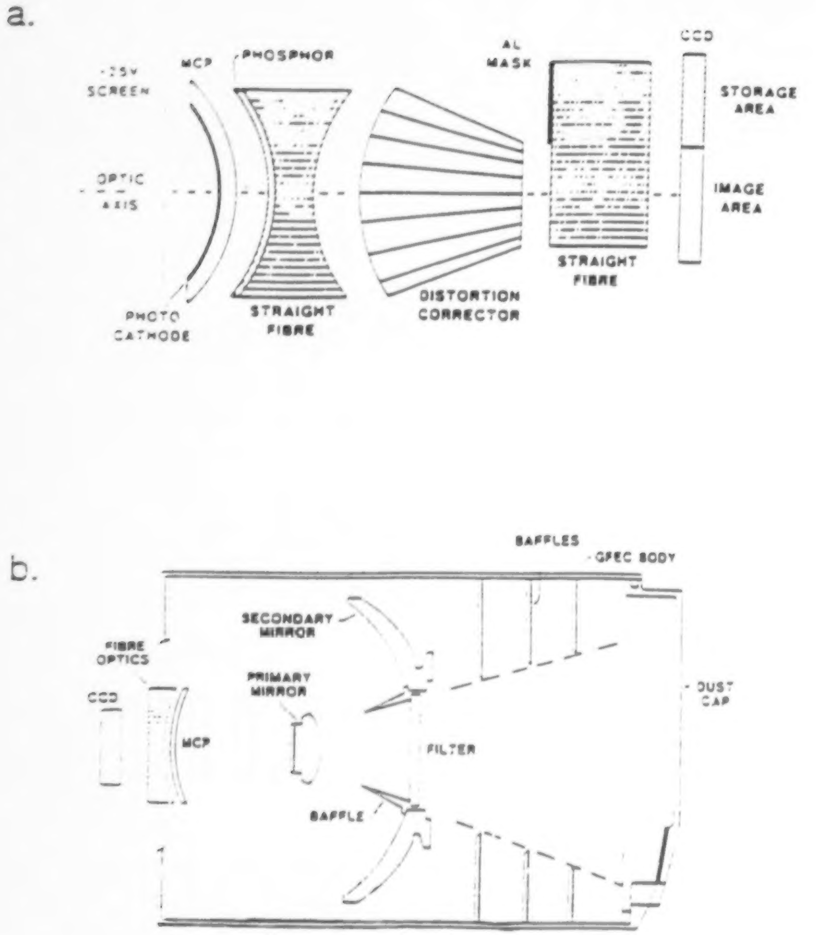

Figure 15a. A schematic cross section of the Viking camera's image processing apparatus. The initial image is formed at the photocathode surface of the curved microchannel plate (MCP). The image is then processed via three fibre optic bundles, which serve to map the initial image onto the CCD array for final processing.

15b. A schematic cross section of the camera, including the inverse Cassegrain optics in which primary and secondary mirrors produce a spherical image at the surface of the MCP. [*Anger et al.*, 1987]

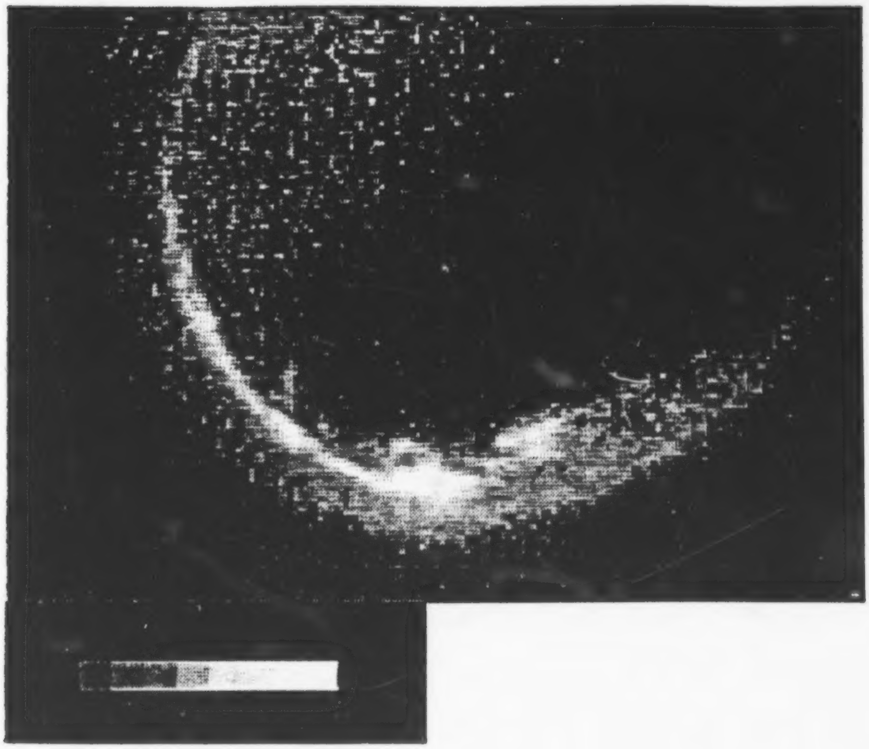

Figure 16. An auroral intensification in the nightside auroral oval, as recorded by the Viking imager. The colour bar varies linearly from 0 to 255 DN (left to right). The circular region of enhanced luminosity defines the auroral oval, where there is a precipitation of energetic electrons. The image has been provided by Martin Connors.

3. ESTABLISHING A QUIET TIME MAGNETOSPHERIC MAGNETIC FIELD AND CURRENT CONFIGURATION

REQUIREMENTS FOR MAGNETIC FIELD MODELLING

A substorm event is studied as part of this thesis. The regions in the ionosphere of auroral activation during this event are mapped into the magnetosphere by tracing magnetic field lines, as determined by a global magnetic field model, from the ionosphere outwards. The accuracy of such mappings therefore depends on how accurately the model approximates the magnetic field configuration for a given time. It is difficult to approximate a substorm magnetic field configuration because the magnetosphere magnetic field configuration is not in steady state, and varies throughout the period of enhanced activity. As noted in chapter 1, large-scale currents are enhanced during substorm growth phase. Such increases in current strength are accompanied by global magnetic field variations. The formation of a substorm current wedge at expansive phase onset causes localized magnetic field perturbations in the magnetotail (as in figure 10). While substorms generally develop in three phases, each substorm is unique in the magnitude of large-scale current variations, and in the extent and local time development of the substorm current wedge. There is no standard magnetosphere "substorm configuration" which accurately represents the instantaneous magnetospheric magnetic field during all substorm events. It is therefore necessary to best approximate the magnetosphere configuration for a given substorm by specifying as many parameters as the magnetic field model allows. Both the T87 and *Donovan* [1993b] magnetic field models will be used in this thesis to address these modelling considerations.

The Tsyganenko models are the most commonly used magnetic field models in magnetospheric physics and these models feature a Kp activity dependence. The T87 and T89 magnetic field configurations represent best fits to a set of magnetotail observations acquired over years for the specified Kp value. It is advantageous to have the magnetic field specified by such a large set of observations. However, the observations may not accurately represent the field configuration for a specific substorm event. The Kp value (as described in appendix B) is calculated for each three hour interval, and therefore reflects the difference between the maximum and minimum values of any of the three components of the perturbation field, whichever is the largest, during this interval. Magnetic field data obtained during intervals of a given Kp value may therefore include measurements for various magnetic field configurations. The use of the Kp index in developing and categorizing magnetospheric magnetic field configurations in the Tsyganenko models may lead to inaccuracies when using these models for a specific substorm event.

An alternative approach to magnetic field modelling is followed in this thesis, using the Donovan magnetic field model. The Donovan magnetic field model includes magnetopause, ring, cross-tail, and field-aligned currents which may be altered to allow for a specification of the current (and hence magnetic field) configuration for a specific event. Instead of attempting to best represent an average configuration for a disturbed activity level (as is done in the Tsyganenko models), the Donovan model is used to best approximate the global magnetic field at a given time during a substorm event, as determined from observations made at the time of the event. This approach is limited, however, by the lack of observations available at any one time. The substorm data set is restricted to a few point measurements in space, complemented by observations at ground stations, which must be used to determine the magnetic field at all locations in the magnetosphere. The magnetic field configuration determined from such a limited set of measurements is highly nonunique.

In order to use the Donovan model, some of this nonuniqueness must be removed. One way of achieving this is to place restrictions on the current configurations, such that parameters within the model are consistent with values that have been determined in previous studies of magnetospheric currents. It is also possible to better specify the magnetic field configuration during a substorm event by first establishing a quiet time magnetic field configuration, and then considering the substorm measurements as perturbations. This is the approach that will be taken in this thesis, and this necessitates a study of quiet time measurements at geostationary orbit in order to establish the quiet time magnetic field configuration.

A SURVEY OF QUIET TIME DATA AT GEOSTATIONARY ORBIT

In order to determine the quiet time magnetic field configuration at geostationary orbit, it is necessary to construct a data set from a large number of GOES measurements which range across all local times. This requires incorporating measurements made throughout the course of a year into the data set. A problem arises in developing such a data set, however, since seasonal and diurnal variations exist in the data when they are expressed in the VDH coordinate system (which is described in appendix A). Figure 17 shows the magnetic field VDH components during two quiet days (AE generally < 50 nT) in June and December 1986, as measured by the GOES 6 satellite. Seasonal variations are evident in the B_V and B_D components. *Rufenach et al.* [1992] studied these variations and developed two-dimensional Fourier series expressions, in time of year and season, for the VDH components at three geostationary meridians. They found that the B_D and B_V values may vary as much as 20 nT over the course of a year. It is necessary to determine the nature of these seasonal variations, in order to take these seasonal effects into account, when considering a set of geostationary magnetic field measurements acquired over the course of a year.

THE NATURE OF SEASONAL AND DIURNAL VARIATIONS AT GEOSTATIONARY ORBIT

McPherron and Barfield [1980] studied magnetic field substorm signatures at geostationary orbit over the course of a year and noted a seasonal change in the signatures of substorm wedge field-aligned currents. They proposed that these variations were the result of seasonal changes in the position of the neutral sheet with respect to the satellite. *Kokubun and McPherron* [1981] noted similar variations in geostationary magnetic substorm signatures at different times of year. They determined that the variations they observed were consistent with those expected for varying positions of the neutral sheet.

The neutral sheet is believed to "hinge" (deviate from the magnetic equatorial plane) in the near-earth tail region (as in figure 18). Hinging of the neutral sheet occurs when the geomagnetic dipole axis is inclined with respect to the Z_{gsm} axis (the gsm coordinate system is described in appendix A). The dipole tilt angle is defined as the angle between the Z_{gsm} axis and the dipole axis, and is positive for the north dipole pole tilted sunward of Z_{gsm}. In regions earthward of ~ 4 R_E [cf. *Lopez*, 1990], the neutral sheet is aligned with the geomagnetic equatorial plane (perpendicular to the dipole axis). In regions beyond ~ 12 - 15 R_E downtail [cf. *Fairfield et al.*, 1987], the neutral sheet near midnight is aligned with the Sun-Earth line (X_{gsm} axis). The neutral sheet makes a smooth transition between these two regions, such that the neutral sheet lies between the XY_{gsm} and XY_{mag} planes at the radial distance of geostationary orbit. The "hinging distance", the distance at which the neutral sheet deviates from the magnetic equatorial plane, is closer to the Earth during disturbed periods of activity such as substorms [*Fairfield*, 1980].

Lopez [1990] examined AMPTE/CCE data at radial distances $5 < R < 8.8\ R_E$ in the tail, and identified neutral sheet crossings by reversals in the sign of the magnetic field V component. He established an expression for the position of the neutral sheet from 1087 such neutral sheet crossings:

$$\theta_{ns} = -(.14Kp + .69)[\cos \Phi]^{\frac{1}{3}}(.065R - .16)\psi \qquad (16)$$

for $6 < R < 9\ R_E$, where $\theta \equiv$ the position in degrees of the neutral sheet relative to the magnetic equator, $\Phi \equiv$ magnetic local time in degrees such that midnight is at 0°, $R \equiv$ radial distance in R_E, $Kp \equiv$ 3-hourly magnetic activity index, and ψ $\equiv$ dipole tilt angle. The local time dependence in equation 16 implies that neutral sheet displacement from the magnetic equatorial plane is largest near midnight and falls to zero at dawn and dusk.

Seasonal variations in the position of the neutral sheet arise from the dependence of neutral sheet displacement on the dipole tilt angle. This angle varies with both time of day and season. Figure 19 shows the yearly dipole tilt angle variation for 12 UT. The dipole tilt angle is maximum negative at winter solstice, and maximum positive at summer solstice. These two values correspond to extremes where the neutral sheet is displaced maximum distances above and below the magnetic equatorial plane, respectively.

The maximum neutral sheet displacement at radial distances near geostationary orbit, at quiet times, may be approximated from equation 16. For Kp=0, $\Phi = 0$, and R=6.6 R_E, the maximum displacement latitudes are ~ 6° and -6° at winter and summer solstices, respectively. The geomagnetic latitudes of GOES 5 and 6, the two satellites whose data are used in this thesis, are 11° and ~ 9°, respectively. Therefore, the neutral sheet is closest to (farthest from) GOES 5 and 6 at winter (summer) solstice. Figure 20 illustrates the position of a GOES satellite with respect to the neutral sheet configuration predicted by equation 16, for the two maximum displacements. The satellite moves across the magnetotail, through positions 1, 2, and 3. In winter (summer), the satellite moves closer to (farther from) the neutral sheet as it approaches local midnight. If one assumes the sign and magnitude of the B_V component to be indicative of the satellite position with respect to the neutral sheet [cf. *Kokubun and McPherron*, 1981], one would expect the value of B_V to become more (less) negative in local time as the satellite approaches midnight during summer (winter) months. One would also expect B_V values to generally be lower in summer. From figure 17, it can be seen that such seasonal and diurnal variations exist at geostationary orbit, and variations in the magnetic field components may therefore be explained by the displacement of the neutral sheet predicted by equation 16.

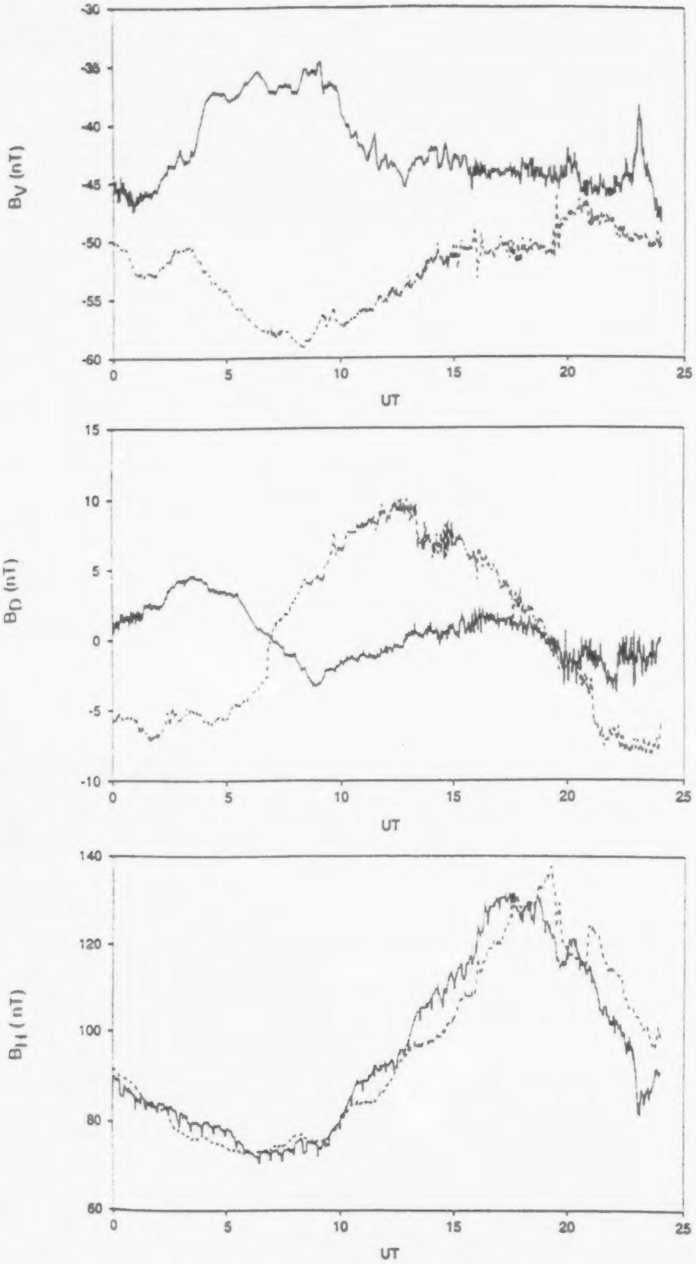

Figure 17. VDH components of the magnetic field, as measured by GOES 6 on June 19 (dashed line) and December 18 (solid line), in 1986.

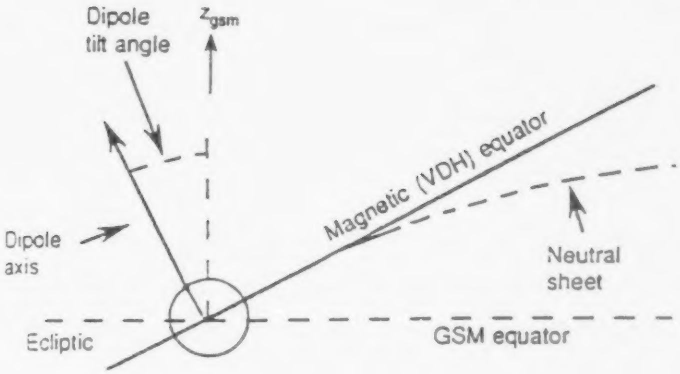

Figure 18. Hinging of the neutral sheet in the XZ_{gsm} plane. The neutral sheet is displaced below the magnetic equatorial plane ($-Z_{gsm}$ direction) for a positive dipole tilt angle. (as adapted from *Lopez* [1990]).

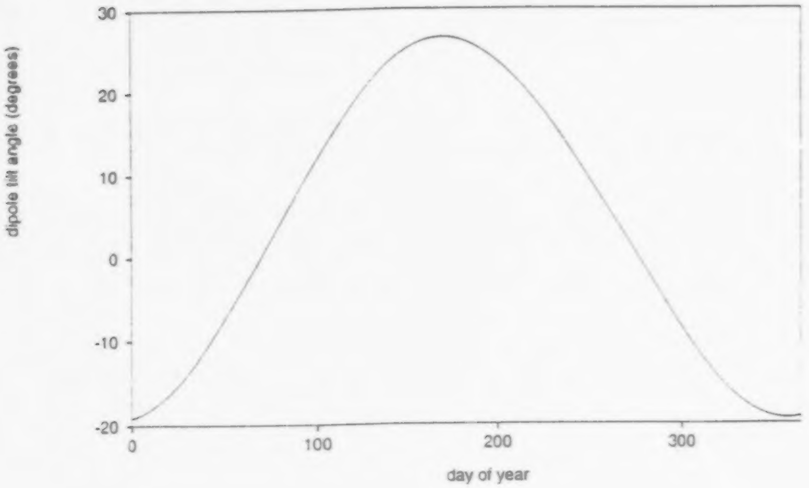

Figure 19. Dipole tilt angle as a function of the day of year, at a constant time of 12 UT.

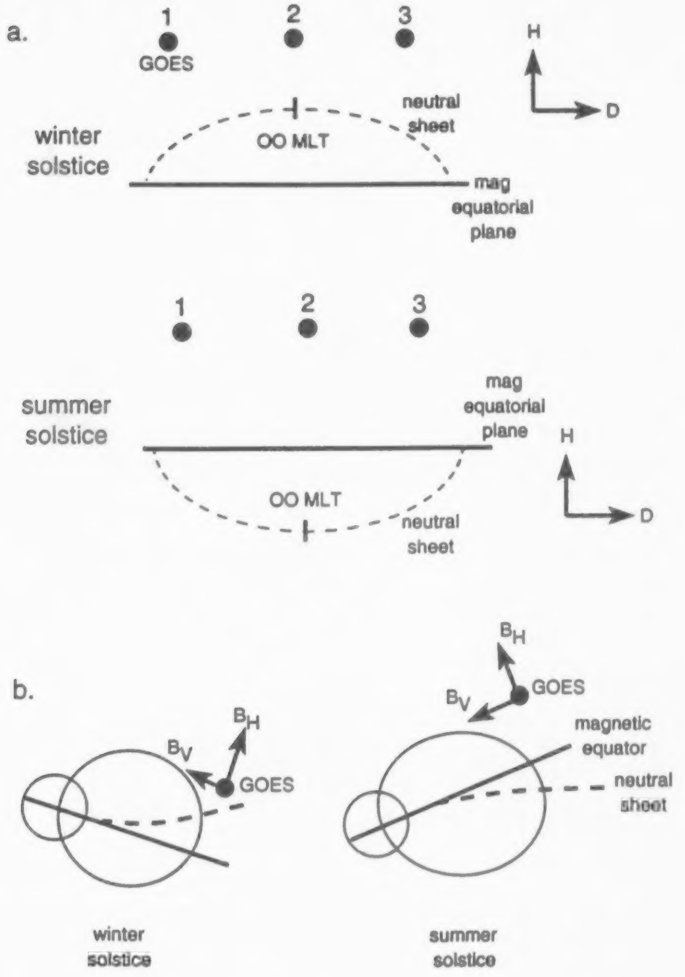

Figure 20.a. A projection of the neutral sheet configuration in the local HD plane, at winter ($\psi < 0$) and summer ($\psi > 0$) solstices for $R \sim 6.6$ R_E. The GOES satellite moves through nightside positions 1, 2, and 3 during the course of a day.

b. Neutral sheet configuration in the local HV plane, at winter and summer solstices. GOES is located at local midnight.

DEVELOPMENT OF THE DATA SET

For the purposes of determining the quiet time magnetic field at geostationary orbit, a data set was developed from a year of GOES 5 and 6 magnetometer data. In order to best determine the magnetospheric current configuration from this data set using the Donovan model, it is necessary to acquire measurements from different times of year, so as to obtain a large data set. The seasonal displacement of the neutral sheet implies a displacement of the central plane of current symmetry, consistent with $\vec{\nabla} \times \vec{B} = \mu_o \vec{J}$. It is therefore necessary to process the measurements such that seasonal effects are removed, and all data may be assumed normalized to a zero dipole tilt current configuration. This is achieved by rotating a given measurement from the VDH coordinate system into the local neutral sheet cylindrical coordinates (herein referred to as XYZ), as determined from equation 16, such that the Z axis is perpendicular to the local neutral sheet, positive northwards. Y lies in the DH plane, positive eastwards, and X is positive in the direction of $\vec{Y} \times \vec{Z}$. Equation 16 is valid only from 18 to 6 MLT, across midnight, and therefore only nightside values are considered. Distances from the local neutral sheet are calculated for each measurement. The final data set therefore consists of nightside measurements at different local times, and distances above the neutral sheet, over the course of a year. Each measurement has been resolved into components parallel and perpendicular to the plane of the neutral sheet such that all measurements may then be assumed relevant to a zero dipole tilt configuration. The quiet time current configuration may then be modelled from this data set using the Donovan model.

Data selection

The GOES 5 and 6 data were obtained during quiet periods in 1986, and underwent two selection processes. Measurements were initially selected for intervals where AE was generally less than 50 nT and remained low for a period of at least a few hours. This selection criterion assured that measurements were consistently chosen for quiet levels of activity. A graph of the AE index over a typical selected interval (10 - 17 UT) is shown in figure 21 (12 Jan). The AE index is calculated from an envelope of measurements at stations located at different meridians, as outlined in appendix B. Observations at Poste de la Baleine and Yellowknife contribute to the calculations of 1986 AE indices. These two stations lie on meridians close to the geographic meridians of GOES 5 and 6, respectively. In addition to the selection criterion of AE $<$ 50 nT, individual magnetograms were examined at these two stations to verify that no localized activity took place near the GOES 5 and 6 meridians. The UT distribution of the initial data set is illustrated in figure 22. The smaller amount of data near 12 UT may be explained by the results of *Rostoker* [1972]. He determined that the hourly average AE value, as determined over the course of a year, was greatest near 12 UT. This occurred as a consequence of the irregular spacing of observatories used in the calculation of the AE index, such that more complete coverage of the nightside oval occurs at $\sim$ 12 UT. One would therefore expect fewer cases of low AE values in this local time sector.

A second selection process was necessary in order to identify and discard satellite data which contained offsets. GOES 5 experienced a continual Hp offset of $\sim$ 20 nT during the period Jan 2 - Mar 13. This offset is included in all three magnetic field components after rotation into the VDH coordinate system. The GOES 5 data are therefore inaccurate, and hence are discarded, for this interval. There are also short term offsets in Hp and Hn for both GOES 5 and 6 throughout 1986. The Hp offsets are the result of spacecraft eclipses which occur near midnight at equinox. An example of this type of offset is shown in figure 23. Intervals containing such offsets were eliminated from the data set. Howard Singer [*private communication*] has carried out case studies of several Hn offsets for GOES 6. These offsets have magnitudes of a few nT, and it was concluded that they arose from instrument gain changes and calibrations that were not perfectly matched for the different ranges of operation of the detector. The effect is not cumulative, as the range change occurs in the opposite direction sometime later, usually within 5 or 6 hours. These offsets are difficult to detect when considering an interval of data on a time scale of less than 6 hours. It is therefore necessary to initially consider longer intervals of data (i.e. 24 hours); offsets, if they exist, can then be identified in the smaller interval of interest. An example of such an offset is shown in figure 24. These offsets were identified visually and eliminated from the data set. GOES 5 persistently experienced such offsets during the summer months, in the interval 2.5 to 12.5 UT. There were also small oscillations ($\sim$ 3 nT) in the GOES 6 Hp component from October to December. These oscillations resulted from the interference of other instruments onboard GOES, when they operated in certain modes. An example of these oscillations is shown in figure 25. Such oscillations have a period of $\sim$ 1/2 hour. The data were eventually binned in local time sectors of at least one hour, and intervals of data containing these oscillations were not discarded, as the oscillations were small, and the effects averaged out.

The final distribution of all data, in local time, including both GOES 5 and 6 measurements, is illustrated in figure 26. The average AE value for this data set is 40 nT, with a standard deviation of 15.

Coordinate Transformation

The rotation of the GOES 5 and GOES 6 magnetic field vectors into local neutral sheet coordinates entails rotations through two angles: α in the VH plane, and β in the DH plane. α, for a given local time and radial distance, is calculated numerically, and the geometry of the calculation is shown in figure 27 (where $\alpha > 0$ for $\psi < 0$).

$$\alpha = \tan^{-1}(\frac{\Delta h}{\Delta w})$$

where

$h \equiv$ height above magnetic equatorial plane

$= R\sin\theta_{ns}$

$w \equiv$ distance from the centre of the Earth, parallel to the magnetic equatorial plane

$= (R^2 - h^2)^{\frac{1}{2}}$

such that

$$\Delta h = h_2 - h_1 = R_2 \sin\theta_{ns2} - R_1 \sin\theta_{ns1}$$

where

$$\theta_{ns1} = -(.14Kp + .69)[\cos\Phi]^{\frac{1}{3}}(.065R_1 - .16)\psi$$

$$\theta_{ns2} = -(.14Kp + .69)[\cos\Phi]^{\frac{1}{3}}(.065R_2 - .16)\psi$$

and

$$\Delta w = (R_2^2 - h_2^2)^{\frac{1}{2}} - (R_1^2 - h_1^2)^{\frac{1}{2}}$$

Figure 28 is a graph of the neutral sheet displacement (in the HV plane) from the magnetic equatorial plane, h, as a function of R. This graph has an approximately linear form, such that the slope changes negligibly over a .2 $\mathrm{R_E}$ interval. R_1 and R_2 are therefore approximated by $R - .1\ \mathrm{R_E}$ and $R + .1\ \mathrm{R_E}$ in calculations of α.

α is evaluated at a radial distance, R, such that the axis perpendicular to the local neutral sheet (in the HV plane) passes through the GOES position. This condition requires that

$$R = 6.6 \frac{\sin c}{\sin b} \tag{17}$$

where angles b and c are defined in figure 29, and R is in $\mathrm{R_E}$. The values of these angles depend on R, and expression 17 is evaluated numerically, using an iterative procedure. The R values of the entire data set range over a .5 $\mathrm{R_E}$ interval, from 6.3 to 6.8 $\mathrm{R_E}$. It will be assumed, for purposes of later data analysis, that all measurements are made at $R \sim 6.6\ \mathrm{R_E}$.

The closest distance, in the HV plane, from the satellite to the neutral sheet is calculated as

$$\mathrm{z_{HV}} = 6.6 \frac{\sin a}{\sin b} \tag{18}$$

where angles a and b are defined in figure 29, and R is in $\mathrm{R_E}$.

The geometry for the calculation of the angle β is shown in figure 30 (where β is positive). β, for a given local time and radial distance, is calculated as follows:

$$\beta = \tan^{-1}(\frac{\Delta h'}{R\Delta\Phi})$$

where Φ is in radians, and

$$\Delta h' = R[\sin\theta_{ns2} - \sin\theta_{ns1}]$$

where

$$\theta_{ns1} = -(.14Kp + .69)[\cos\Phi_1]^{\frac{1}{3}}(.065R - .16)\psi$$

$$\theta_{ns2} = -(.14Kp + .69)[\cos\Phi_2]^{\frac{1}{3}}(.065R - .16)\psi$$

and

$$R\Delta\Phi = R(\Phi_2 - \Phi_1).$$

Figure 31 shows the neutral sheet displacement (in the HD plane) from the magnetic equatorial plane, h', as a function of magnetic local time, Φ. The slope is approximately constant over each 4° interval, except for the range 85° to 90°. The data in this local time sector, however, are discarded because equation 16 predicts that the neutral sheet joins the magnetic equatorial plane near dawn and dusk at a 90° angle (as shown in figure 31). As will be shown later, there is evidence that the neutral sheet does not necessarily join the magnetic equatorial plane abruptly at dawn and dusk. The height of the neutral sheet above the magnetic equatorial plane is a linear function of Φ in each 4° interval in the range 0° to 85°, and values of $\Phi_1 = \Phi - 2°$ and $\Phi_2 = \Phi + 2°$ are therefore used in the calculation of β.

The values of β are small ($< 6°$) so that the perpendicular distance of the satellite from the neutral sheet, z, may be approximated by the perpendicular distance in the HV plane: $\mathrm{z_{HV}}$, as calculated from equation 18. The values of β are small enough such that an iterative calculation of Φ (similar to that done in the HV plane for R) is unnecessary. The local time, Φ, at which an axis perpendicular to the local neutral sheet (in the HD plane) passes through the GOES position may be approximated as

$$\Phi = \Phi_{GOES} + \Delta\Phi = \Phi_{GOES} + \frac{1}{R} z_{HV} \sin\beta$$

$\Delta\Phi$ has a maximum value of $\sim 1.5°$, and the value of Φ used in the calculation of β is therefore approximated as Φ_{GOES}, the local time of the satellite.

The total coordinate transformation is the product of two rotation matrices:

$$< \alpha, D >= \begin{pmatrix} \cos\alpha & 0 & \sin\alpha \\ 0 & 1 & 0 \\ -\sin\alpha & 0 & \cos\alpha \end{pmatrix}$$

$$< \beta, V >= \begin{pmatrix} 1 & 0 & 0 \\ 0 & \cos\beta & \sin\beta \\ 0 & -\sin\beta & \cos\beta \end{pmatrix}$$

such that $(\mathrm{B_x}, \mathrm{B_y}, \mathrm{B_z}) = \begin{pmatrix} \cos\alpha & -\sin\alpha\sin\beta & \sin\alpha\cos\beta \\ 0 & \cos\beta & \sin\beta \\ -\sin\alpha & -\sin\beta\cos\alpha & \cos\alpha\cos\beta \end{pmatrix} \begin{pmatrix} \mathrm{B_V} \\ \mathrm{B_D} \\ \mathrm{B_H} \end{pmatrix}$

For the selected quiet intervals, Kp is set equal to zero in the α and β angle calculations.

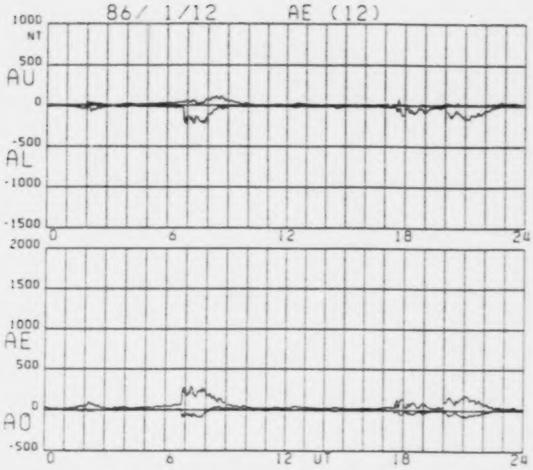

Figure 21. A plot of the AE, AU, and AL indices for January 12, 1986, where AE = |AU| + |AL|.

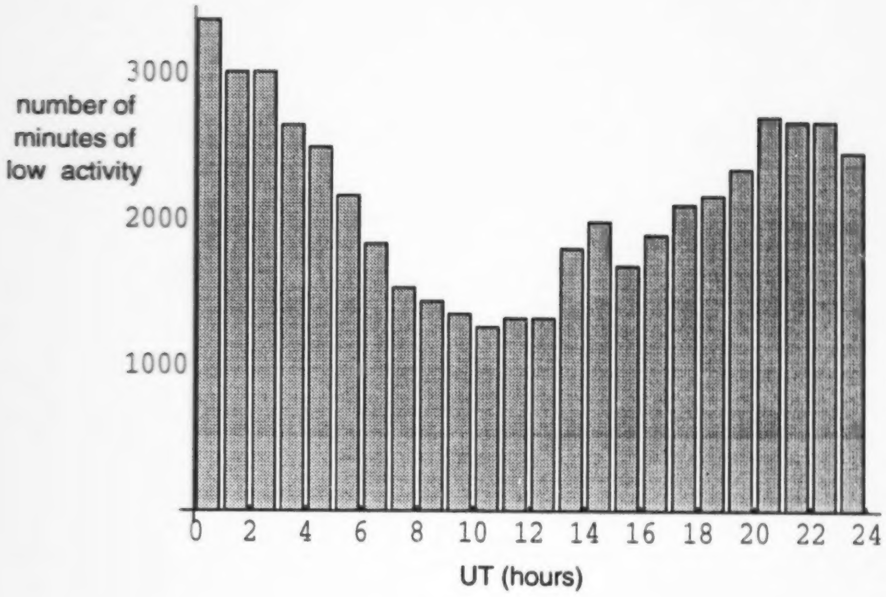

Figure 22. A histogram showing the distribution of low activity, per hour UT, in 1986.

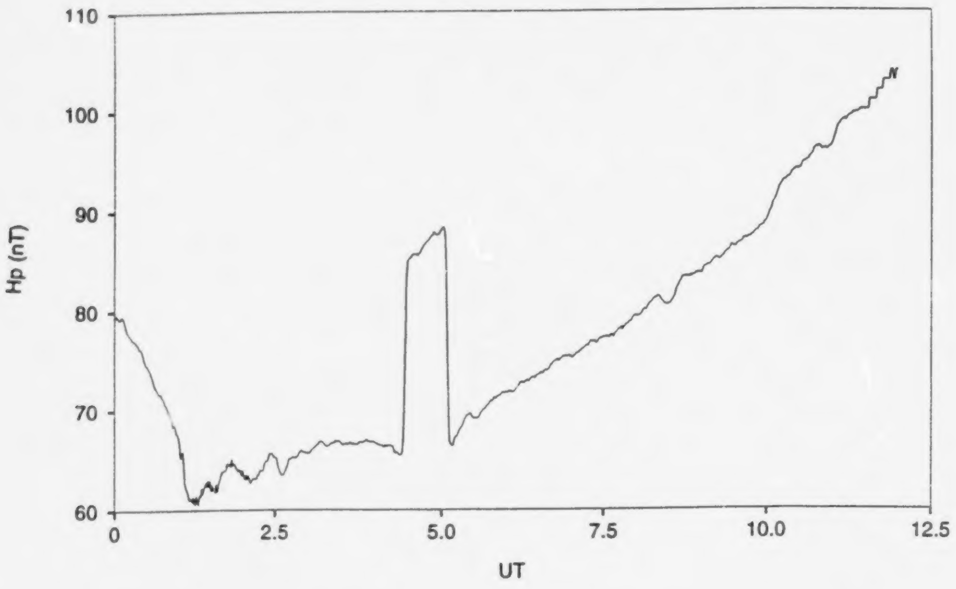

Figure 23. An offset in the Hp magnetic field component, as measured by GOES 5 on October 12, 1986. The offset occurs between ~ 0430 and 0500 UT.

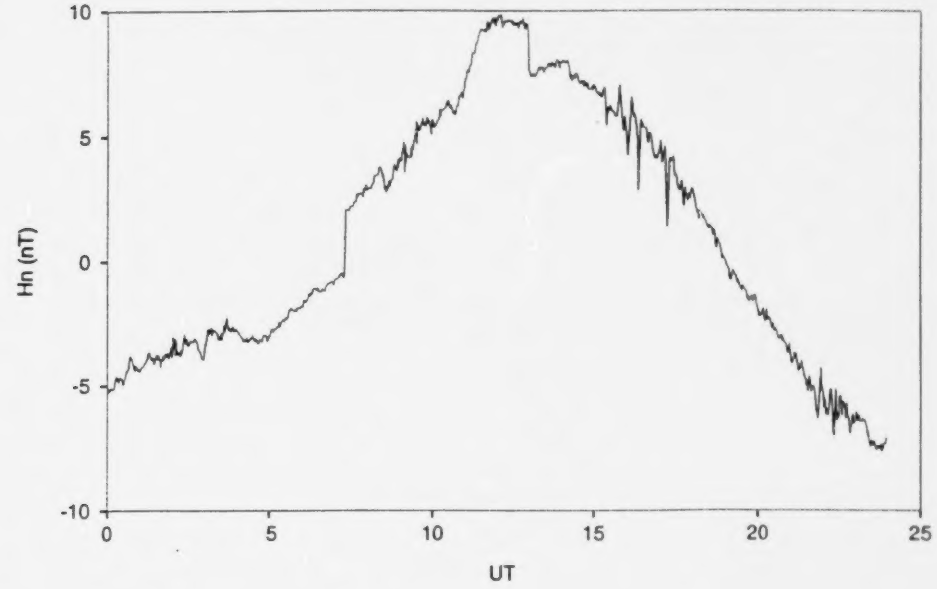

Figure 24. An offset in the Hn magnetic field component, as measured by GOES 6 on April 27, 1986. The offset occurs between ~ 0700 and 1230 UT.

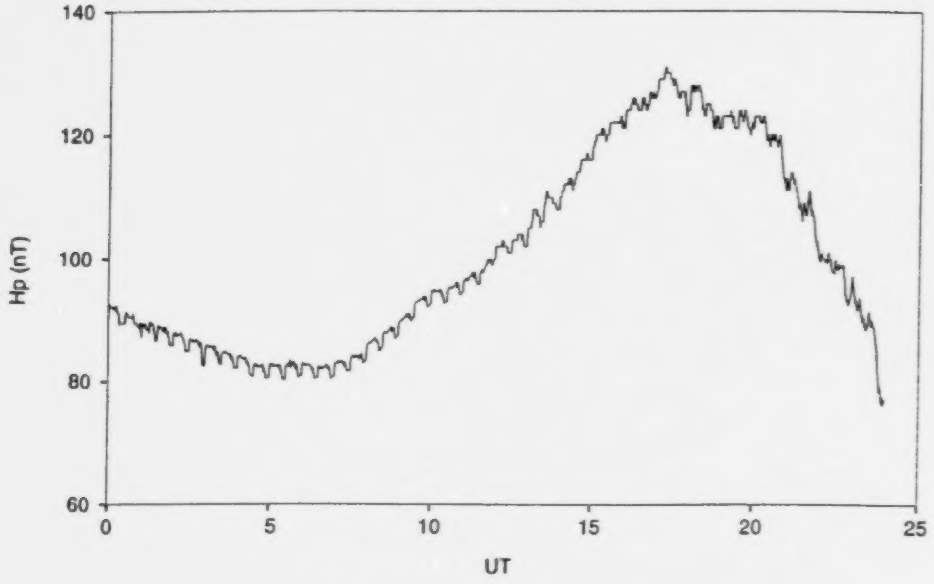

Figure 25. Oscillations in the Hp magnetic field component, as measured by GOES 6 on November 19, 1986.

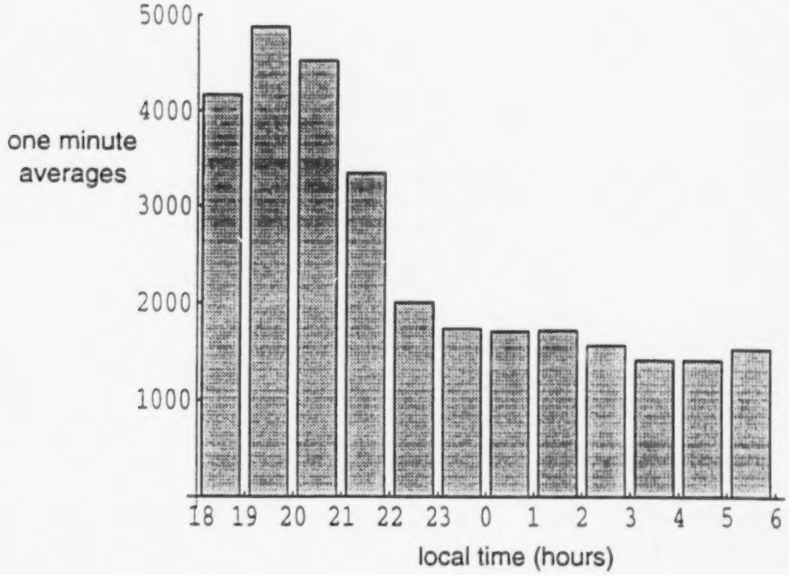

Figure 26. A histogram showing the total number of one minute average magnetic field measurements (from both GOES 5 and 6) included in the GOES data set, per hour of local time.

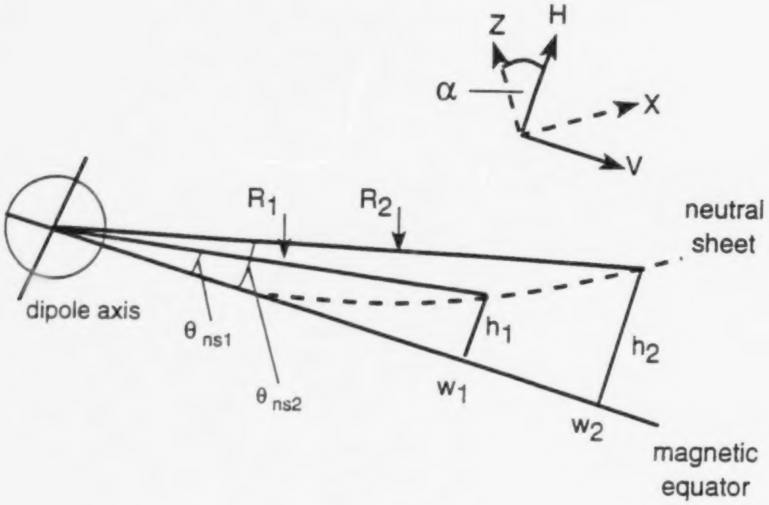

Figure 27. The geometry of the α angle calculation, in the local HV plane. h is the perpendicular distance above the magnetic equator, and w is the distance, parallel to the magnetic equator (measured from the centre of the Earth), at which h is measured. R is the radial distance to the position of the neutral sheet at which h is measured.

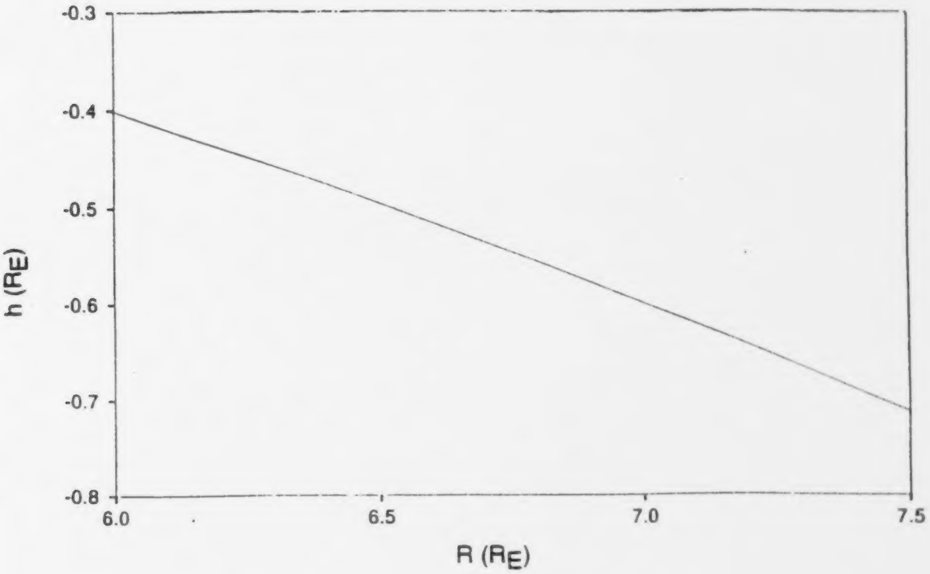

Figure 28. Displacement of the neutral sheet (in the HV plane) from the magnetic equatorial plane, *h*, as a function of radial distance, *R*, from the centre of the Earth to the position of the neutral sheet. *h* is calculated for Kp=3, $\psi = 15$, and $\Phi = 0$.

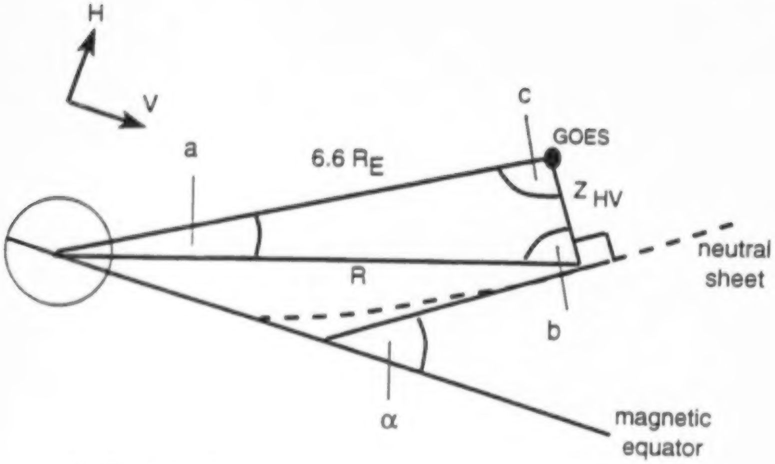

$a = \Theta_{GOES} - \Theta_{ns}$

$b = 90 - \alpha + \Theta_{ns}$

$c = 180 - a - b$

Θ_{GOES} = 11 degrees for GOES 5
= 9 degrees for GOES 6

Figure 29. Geometry of the calculation of R. R is the radial distance to the position of the neutral sheet which is closest to the GOES satellite in the HV plane.

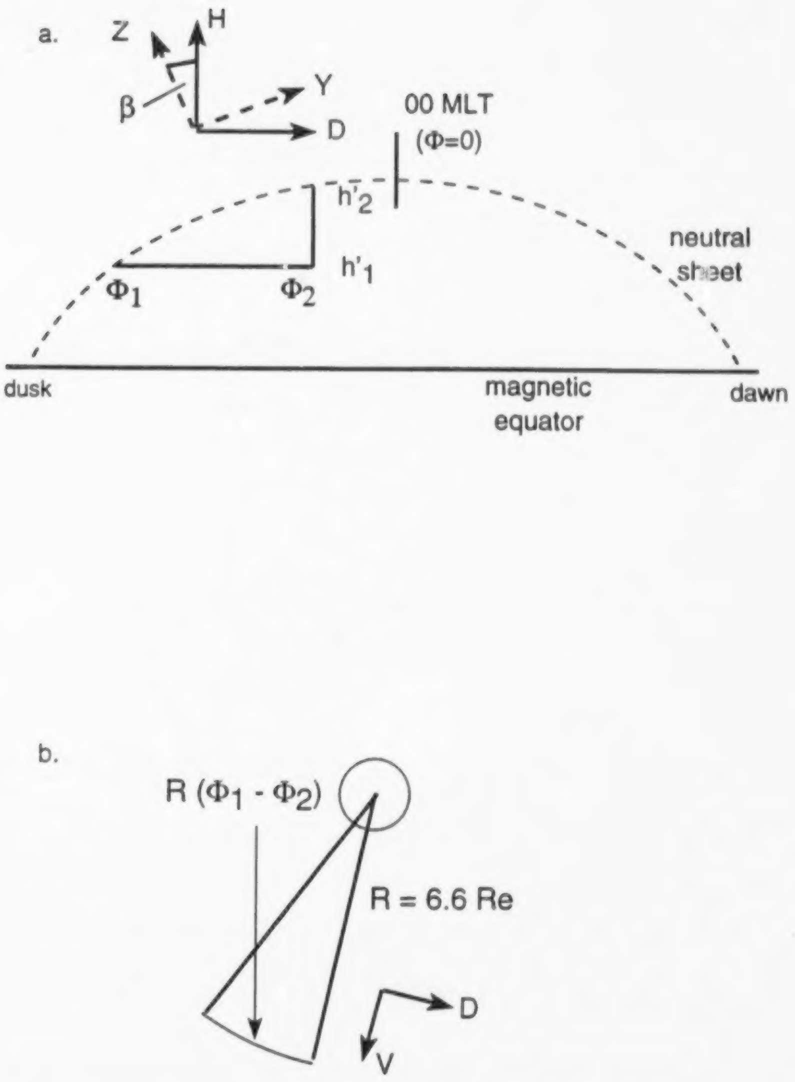

Figure 30.a. Geometry of the calculation of the angle β in the satellite local HD plane, at $R = 6.6\mathrm{R_E}$.

b. Geometry of the calculation of the angle β in the satellite local VD plane.

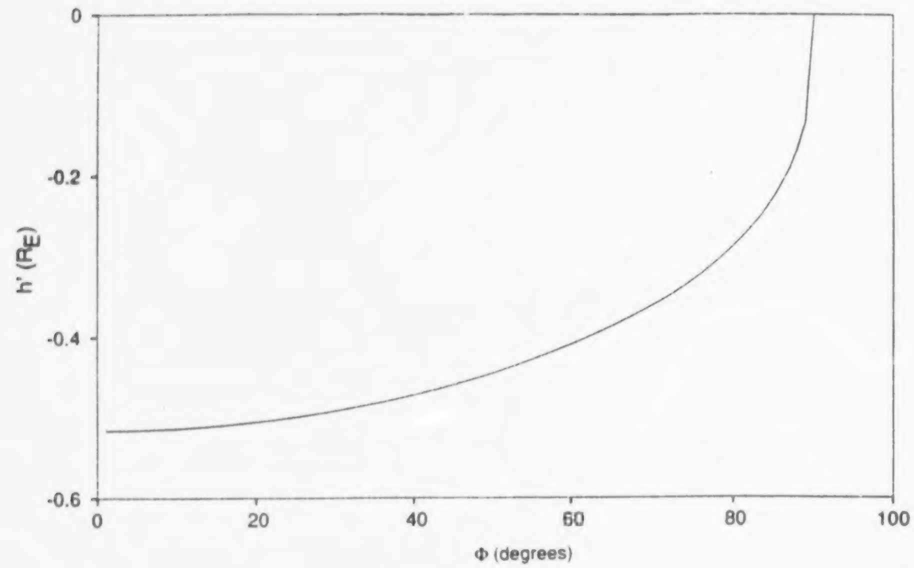

Figure 31. Displacement of the neutral sheet (in the HD plane) from the magnetic equatorial plane, h', as a function of local time Φ where $\Phi = 0$ at midnight. h' is calculated for Kp=3, $\psi = 15$, and $R = 6.6\mathrm{R_E}$.

ANALYSIS OF THE TRANSFORMED DATA SET

The transformed data set consists of B_x, B_y, and B_z values at different local times and perpendicular distances above the neutral sheet (.25 $R_E < z < 1.75$ R_E), at $x \sim 6.6$ R_E. In order to verify that this coordinate system, and calculated distances from the neutral sheet, are reasonable, measurements were separated into 2 hours MLT × .25 R_E bins and averaged. The least number of points in a bin was 191, and the greatest number of points was 2193. Figure 32 shows graphs of the magnetic field angle of inclination, η_{XYZ}, versus distance from the neutral sheet, in each 2 hour local time sector. The angle of inclination is calculated as

$$\eta_{XYZ} = \sin^{-1}(\frac{B_z}{B_{total}})$$

and is measured as positive northwards from the -X axis, such that $\eta = 90°$ at the neutral sheet. Standard deviations for each bin were calculated and plotted as error bars. The data are approximated by best fit lines, and the angles of inclination in VDH coordinates also plotted (calculated as $\eta_{VDH} = \sin^{-1}(\frac{\mathrm{H}}{\mathrm{B_{total}}})$). The angles of inclination for a dipolar configuration are also plotted on each graph. The graphs illustrate two things:

1. Values of η_{XYZ} at the neutral sheet (z=0) are between 85° and 90° degrees in each magnetic local time sector. This indicates that the transformed coordinate system, and calculated positions of the neutral sheet, are reasonable. The η_{VDH} values underestimate the angle of inclination at the neutral sheet by approximately 20°, and the data are better represented in the XYZ coordinate system. The discrepancies in η_{VDH}, as compared to η_{XYZ}, would be larger for disturbed periods when the neutral sheet is displaced farther from the magnetic equatorial plane.

2. The η_{XYZ} values, as compared to the angles of inclination for a dipole, indicate that the geostationary quiet time magnetic field is more taillike than a dipolar configuration. The falloff in η_{XYZ} differs for each local time sector. The η_{XYZ} functions decrease most steeply at the centre of the tail, and less steeply towards dawn and dusk. This implies that the field is less taillike towards dawn and dusk than at midnight.

Values of B_{total} as a function of the distance from the neutral sheet are plotted in figure 33 for the different magnetic local time sectors. The best fit line intercepts (neutral sheet values) are lowest at midnight, and larger towards dawn and dusk. The strength of the magnetic field in the neutral sheet is therefore lowest at the centre of the tail, again implying that the magnetic field configuration is more taillike in the noon-midnight meridian plane than at the flanks of the tail. The value of B_{total} at the neutral sheet is $\sim$ 79 nT near midnight. An expression for B in the neutral sheet at midnight is given by *Rostoker and Skone* [1993]:

$$B = 7.8e^{-.04x} + 125302x^{-4}$$

where x is in R_E and B is in nT. This expression predicts B=72 nT at midnight. This function was fit to a data set, however, with an average AE index of 120 nT, while the GOES data set has an average AE index of 40 nT. One would therefore expect the *Rostoker and Skone* expression to give a lower value of B, as the field becomes increasingly taillike for higher levels of activity.

The *Lopez* [1990] expression describing the position of the neutral sheet is valid for only nightside local times, implying that the neutral sheet abruptly deviates from the magnetic equatorial plane at a 90° angle at dawn and dusk (as in figure 31).

It is likely, however, that the neutral sheet deviates from the magnetic equatorial plane more gradually, at a smaller angle with respect to the magnetic equatorial plane. The effects of the tail currents, which cause a nightside displacement of the neutral sheet, also extend into the dayside. Figure 34 shows graphs of η_{VDH} versus dipole tilt angle for the local time sectors 16 to 18 MLT and 6 to 8 MLT. These graphs indicate that as the neutral sheet is displaced farther from geostationary orbit on the nightside (as for increasing values of dipole tilt angle), the magnetic field is inclined at less of an angle to the magnetic equatorial plane in these dayside regions. The angles of inclination in figure 34 only fall off by a small amount, but the falloff in η_{VDH} would be greater if the magnetic field components were rotated into the local neutral sheet coordinates, as in figure 32. It is therefore likely that the magnetic effects of the tail currents, which cause the neutral sheet to be displaced from the magnetic equatorial plane on the nightside, also extend into the dawn and dusk dayside regions. The *Lopez* [1990] function for displacement of the neutral sheet therefore predicts an unrealistic configuration of the neutral sheet in the local time sectors within $\sim 5°$ of dawn and dusk (the neutral sheet being almost perpendicular to the magnetic equatorial plane in these regions in figure 31). It is for this reason that the magnetic field data within 5° of dawn and dusk were not included in the transformed geostationary data set.

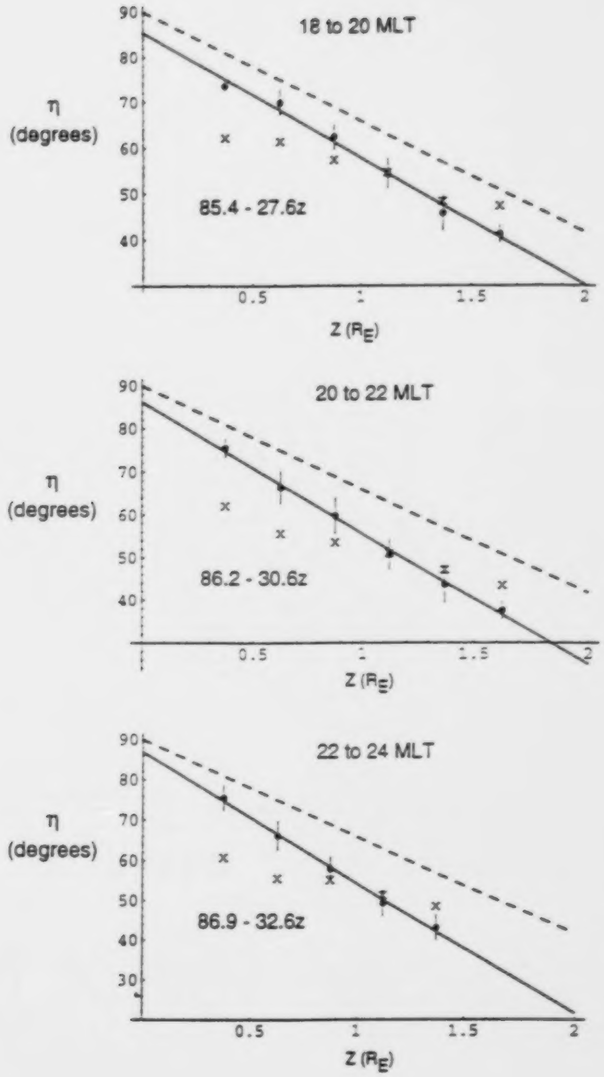

Figure 32. Magnetic field angles of inclination as a function of distance from the neutral sheet, for nightside MLT sectors. The points plotted with error bars are η_{XYZ}, while the "x" points are η_{VDH}. The linear best fit functions for η_{XYZ} are included in each graph. The linear function representing a dipole angle of inclination is plotted as a dashed line. This figure is continued on the next page.

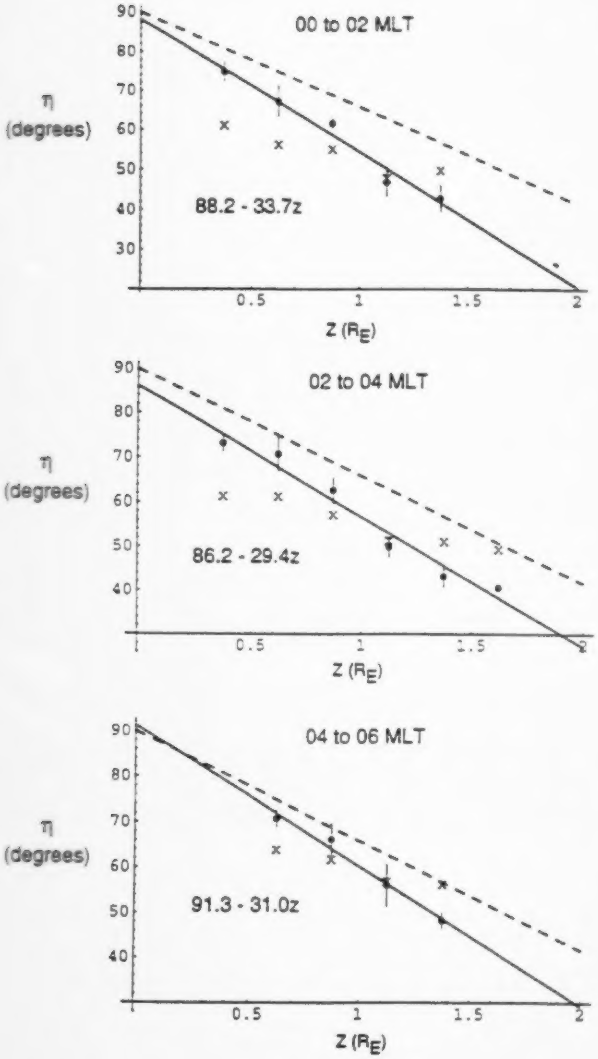

Figure 32 continued.

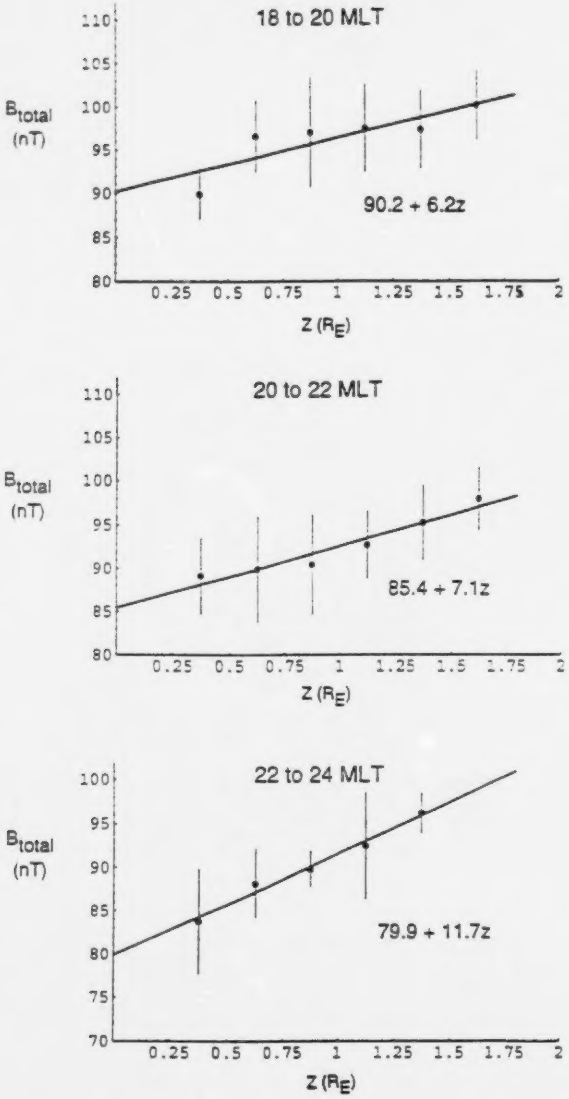

Figure 33. Magnitude of the magnetic field as a function of distance from the neutral sheet, for nightside local time sectors. The linear best fit functions for B_{total} are included in each graph. This figure is continued on the next page.

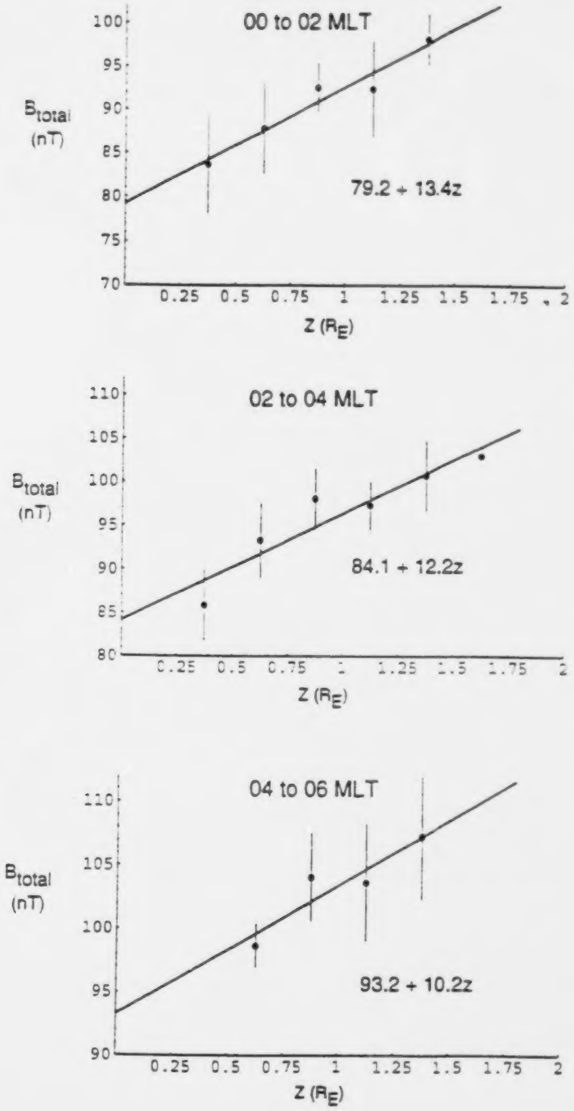

Figure 33 continued.

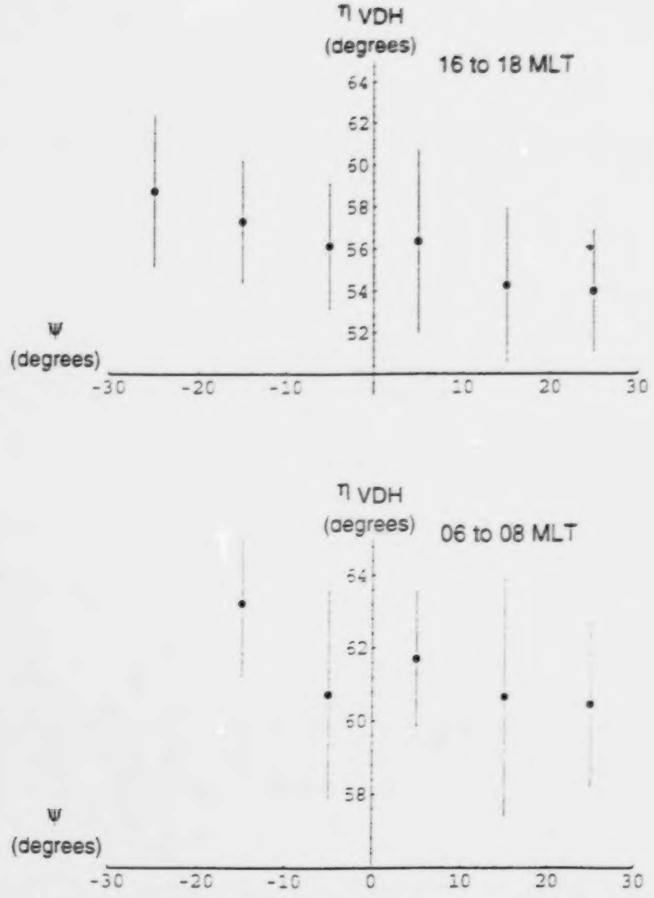

Figure 34. Angles of inclination, η_{VDH}, as a function of dipole tilt angle, for dayside local time sectors 16 to 18 MLT and 6 to 8 MLT.

QUIET TIME CURRENT CONFIGURATION

In order to determine the magnetotail current configuration, it is necessary to subtract the terrestrial magnetic field contribution from the B_{XYZ} values. The perturbation values, ΔB_{XYZ}, then represent the magnetic field contribution due to external currents ($\vec{B}_{ext} = (\Delta B_x, \Delta B_y, \Delta B_z)$). The terrestrial magnetic field may be approximated as the gradient of a scalar such that

$$\vec{\nabla} \times \vec{B}_{terr} = 0$$

$$\Longrightarrow \vec{B}_{terr} = -\vec{\nabla}\phi_{terr}$$

and

$$\nabla^2 \phi_{terr} = -\vec{\nabla} \cdot \vec{B}_{terr} = 0 \tag{19}$$

The International Geomagnetic Reference Field (IGRF) (*IAGA Commission 2 Working Group 4* [1969]) model of the geomagnetic field is used in this thesis to represent the terrestrial field contribution. The IGRF model is calculated from equation 19 as

$$\phi_{terr}(r,\theta,\phi) = a \sum_{n=1}^{\infty} \sum_{m=0}^{n} (g_n^m \cos(m\phi) + h_n^m \sin(m\phi))(\frac{a}{r})^{n+1} P_n^m(\theta)$$

where

$P_n^m(\theta) \equiv$ Legendre polynomials

$\phi \equiv$ geographic longitude

$\theta \equiv$ geographic colatitude

and the coefficients g_n^m, h_n^m are determined from ground and MAGSAT satellite (altitude 300 - 500 km) magnetic field measurements. The accuracy of the IGRF model is difficult to assess. *Langel* [1987] has studied the accuracy and uniqueness of such spherical harmonic terrestrial magnetic field models. The g_n^m and h_n^m coefficients are nonunique in that they are determined for a finite number of data points such that the field magnitude is not known at all points on the sphere. Accuracy of the model is also limited by the order of the spherical harmonics (n) at which the series is truncated. The 1985 and 1990 IGRF models are approximated to n=10. The values of g_n^m and h_n^m also vary slowly in time. Calculations of the terrestrial magnetic field values for 1986 therefore require an interpolation between the 1985 and 1990 IGRF model values, and this process again introduces some inaccuracies. Despite such inherent inaccuracies, however, the IGRF model is considered to be the best representation of the terrestrial field available, and this model is used by the international space physics community.

The IGRF values were transformed into VDH coordinates and subtracted from each GOES B_{VDH} measurement. The magnetic field measurements due to external currents, ΔB_{VDH}, were then rotated into local neutral sheet coordinates to obtain $\Delta B_x, \Delta B_y$, and ΔB_z. All rotated perturbation values were binned in the same manner as the B_{XYZ} values in the previous section. Figure 35 shows the ΔB_x and ΔB_y values for the local time sector 18 to 20 MLT. It is evident that $\Delta B_x = 0$ and $\Delta B_y = 0$ at distances above the neutral sheet position. This trend in ΔB_x and ΔB_y is observed in all local time sectors, and it appears that the *Lopez* [1990] expression (equation 16) must underestimate the displacement of the neutral sheet from the magnetic equatorial plane at geostationary orbit. It should therefore be possible to alter the parameters of equation 16 such that $\Delta B_x = 0$ and $\Delta B_y = 0$

at $z = 0$. However, figure 32 graphs of η_{XYZ} indicate that equation 16 slightly overestimates the neutral sheet displacement from the magnetic equatorial plane. This inconsistency is resolved if the central plane of magnetotail current symmetry is not colocated with the neutral sheet (i.e. the magnetic field is asymmetric above and below the neutral sheet plane). Values of $\Delta B_x > 0$ and $\Delta B_y > 0$ at distances above the neutral sheet indicate that the central plane of current symmetry must be displaced farther than the neutral sheet from the magnetic equatorial plane. This is a reasonable hypothesis if one considers the superposition of $\vec{B}_{terr}$ with $\vec{B}_{ext}$. The terrestrial magnetic field is curl free, such that $\vec{B}_{terr}$ may be superposed with $\vec{B}_{ext}$, without altering the external current configuration, $\vec{J}$:

$$\vec{\nabla} \times \vec{B}_{ext} = \vec{\nabla} \times (\vec{B}_{ext} + \vec{B}_{terr}) = \mu_o \vec{J}$$

The superposition of $\vec{B}_{terr}$ with $\vec{B}_{ext}$ results in a magnetic field geometry such that the neutral sheet defined by $\vec{B}_{terr}$ is now displaced from the magnetic equatorial plane in accordance with equation 16. The new magnetic field configuration is taillike, as in figure 32, such that $\vec{B}_{ext}$ serves to stretch the field tailwards from a dipolar configuration. Such a magnetic field configuration may be achieved by the superposition of $\vec{B}_{ext}$ and $\vec{B}_{terr}$ illustrated in figure 36. The current configuration defined by $\vec{B}_{ext}$ has not been altered by the addition of $\vec{B}_{terr}$ to $\vec{B}_{ext}$. Therefore, the displaced neutral sheet lies in a position between the central plane of current symmetry and the magnetic equatorial plane.

The parameters describing R dependence in equation 16 were altered, in order to best describe the displacement of the central plane of current symmetry from the magnetic equatorial plane, such that

$$\theta_{cs} = -(.14Kp + .69)[\cos\Phi]^{\frac{1}{3}}(C_1R + C_2)\psi \tag{20}$$

best represents the displacement of the central current plane. The values of C_1 and C_2 were determined from the condition that both $\Delta B_x = 0$ and $\Delta B_y = 0$ at z=0. This condition was met for values of $C_1 = .04$ and $C_2 = .3$. Figure 37 shows the displacement of the central plane of current symmetry from the magnetic equatorial plane, as calculated from equation 20, versus R. The displacement of the neutral sheet from the magnetic equatorial plane is also plotted on the same graph. Figure 38 similarly shows displacement of the central current plane and neutral sheet, from the magnetic equatorial plane, as a function of local time at R = 6.6 $\mathrm{R_E}$. The current sheet is displaced $\sim$ .35 $\mathrm{R_E}$ farther from the magnetic equatorial plane than the neutral sheet near midnight (for an average dipole tilt angle).

The ΔB_{VDH} values were rotated into $\Delta B_{X'Y'Z'}$, where the X'Y'Z' coordinate system was determined from equation 20, using the same method described in the previous section. The $B_{X'Y'Z'}$ values range over 6.3 $\mathrm{R_E} < R <$ 6.8 $\mathrm{R_E}$ and it is assumed, as it was for B_{XYZ}, that all $B_{X'Y'Z'}$ measurements are made at $R \sim 6.6\mathrm{R_E}$. The values were separated into 2 hours MLT × .4 $\mathrm{R_E}$ bins and averaged. The bin size differs from that for the B_{XYZ} values because the $\Delta B_{X'Y'Z'}$ values cover a larger range in z' (-.4 $\mathrm{R_E} < z' <$ 2 $\mathrm{R_E}$) than the B_{XYZ} values cover in z. The least number of points in a bin was 114, and the greatest number of points was 2122. Figures 39 and 40 show graphs of $\Delta B_{x'}$ and $\Delta B_{y'}$ versus distance from the central plane of current symmetry, for all nightside local time sectors. Values of ΔB_y and ΔB_x are also plotted on each graph, as a function of perpendicular distance from the neutral sheet. It is evident that the magnetic field values due to external currents are better represented in the X'Y'Z' coordinate system, especially in the dusk sector where results were determined from a large set of data points. The distribution of data in magnetic local time is given in figure 26.

Figure 41 shows $\Delta B_{z'}$ values in the 18 to 20 magnetic local time sector. Unlike the $\Delta B_{x'}$ and $\Delta B_{y'}$ values, $\Delta B_{z'}$ shows no clear linear dependence on z', within the error bars, in the range $0 < B_{z'} < 1.8$ R$_E$. This is reasonable, since B_H shows no significant seasonal dependence in figure 17, and therefore no dependence on the satellite position with respect to the neutral sheet (or central plane of current symmetry).

Modelling the Quiet Time Current Configuration

Figure 42 shows $\Delta B_{x'}$ and $\Delta B_{y'}$ values, as calculated from the linear expressions in figures 39 and 40, versus local time at $z'= 0.5$, 1.0,and 1.5 R$_E$. Figure 43 shows $\Delta B_{z'}$ values (averaged in the range $0 < B_{z'} < 1.8$ R$_E$) as a function of local time. The $\Delta B_{x'}$, $\Delta B_{y'}$, and $\Delta B_{z'}$ curves at geostationary orbit, as calculated from the quiet time Donovan magnetic field model, are also plotted on each graph. The quiet time magnetic field model includes the contributions of magnetopause, ring, and cross-tail currents. Model parameters were altered such that the model magnetic field values best fit the quiet time data.

The magnetopause current contribution has been provided, in the form of magnetic field values, by Karl Pfitzer. These magnetic field values have been calculated at various points in the magnetosphere for a model magnetopause current system. The shape and location of the magnetopause is calculated from parameters determined by *Sibeck et al.* [1991] for an average magnetopause configuration in which the subsolar point is located ~ 10.5 $\mathrm{R_E}$ from the Earth. The ring and cross-tail currents are constructed from cylindrical current elements of finite radius [cf. *Donovan*, 1993b]. The range and extent of the ring current are calculated from a profile of the current density, j, in the equatorial plane developed by *Lui et al.* [1987], and the modelling techniques used to construct the ring current are described by *Donovan et al.* [1993]. A ring current in the range -2 $\mathrm{R_E}$ $< R_{XY_{gsm}} < -9$ $\mathrm{R_E}$, with a dipole moment equal to 3.5 % of the Earth's dipole moment, is used in order to best fit the GOES quiet time data. $R_{XY_{gsm}}$ is the radial distance in the XYgsm plane. This ring current contains 0.8 MA of westward current (distributed in the range -9 $\mathrm{R_E}$ $< R_{XY_{gsm}} < -3.5$ $\mathrm{R_E}$) and 0.2 MA of eastward current (distributed in the range -3.5 $\mathrm{R_E}$ $< R_{XY_{gsm}} < -2$ $\mathrm{R_E}$). The inner edge of the cross-tail current is placed at $X_{gsm} = -7.5$ $\mathrm{R_E}$, at local midnight, and follows a circular path which intersects dawn and dusk at $Y_{gsm} = \pm 10.5$ $\mathrm{R_E}$. The radius of curvature increases with distance downtail (to ∞ at $X_{gsm}{=}-40\mathrm{R_E}$). The distribution of ring and cross-tail currents in the XYgsm plane is shown in figure 44. In order to best fit the quiet time data, it was necessary to concentrate the cross-tail current in the neutral sheet, and at the high latitude edges of the CPS. The CPS thickness is approximated as 3 $\mathrm{R_E}$ at midnight, increasing to 6 $\mathrm{R_E}$ at the flanks of the magnetotail. The model contains no field-aligned currents since such currents are expected to be small during quiet periods.

The local time dependence of all three magnetic field components is well reproduced by the model in figures 42 and 43, and the trend in the $\Delta B_{y'}$ component is due almost entirely to cross-tail current effects alone. The curves produced by the model approximate the $\Delta B_{y'}$ and $\Delta B_{z'}$ values to within a few nT. The model $\Delta B_{x'}$ values are as much as 6 nT lower than the quiet time GOES values, however, and the model produces a magnetic field which is more taillike than the data suggest. The model magnetic field lines are stretched farther downtail than is consistent with the data. A possible reason for this discrepancy between the model and the data may be that the raw GOES data has a long term offset in the Hp component (which is parallel to the satellite spin axis). *Lopez and von Rosenvinge* [1993] determined that such an offset exists in the GOES 5 data, and is caused by currents in the circuitry involving the satellite solar panels. This offset is between -11 and -6.5 nT during 1986. The GOES data set considered in this thesis consists of mostly GOES 6 measurements, but the GOES 6 data are consistent with the GOES 5 values in the treatment of the data in this chapter, and it is therefore likely that a similar offset exists in the GOES 6 satellite measurements. A negative offset in the Hp magnetic field component may therefore be responsible for the discrepancy between the best fit model values and the quiet time data set.

Overall, the model magnetic field values match the quiet time data reasonably well, and a quiet time magnetospheric current configuration has therefore been established for the Donovan model. The quiet time magnetic field values provide a reference field which will be compared to the magnetic field configuration during a substorm event. Such a comparison will give an indication of the relative enhancement of the directly driven currents, and the unique disturbance of the substorm wedge, during the substorm activity. The relative enhancement of the current systems can then be modelled, using the Donovan model, for the specific substorm event.

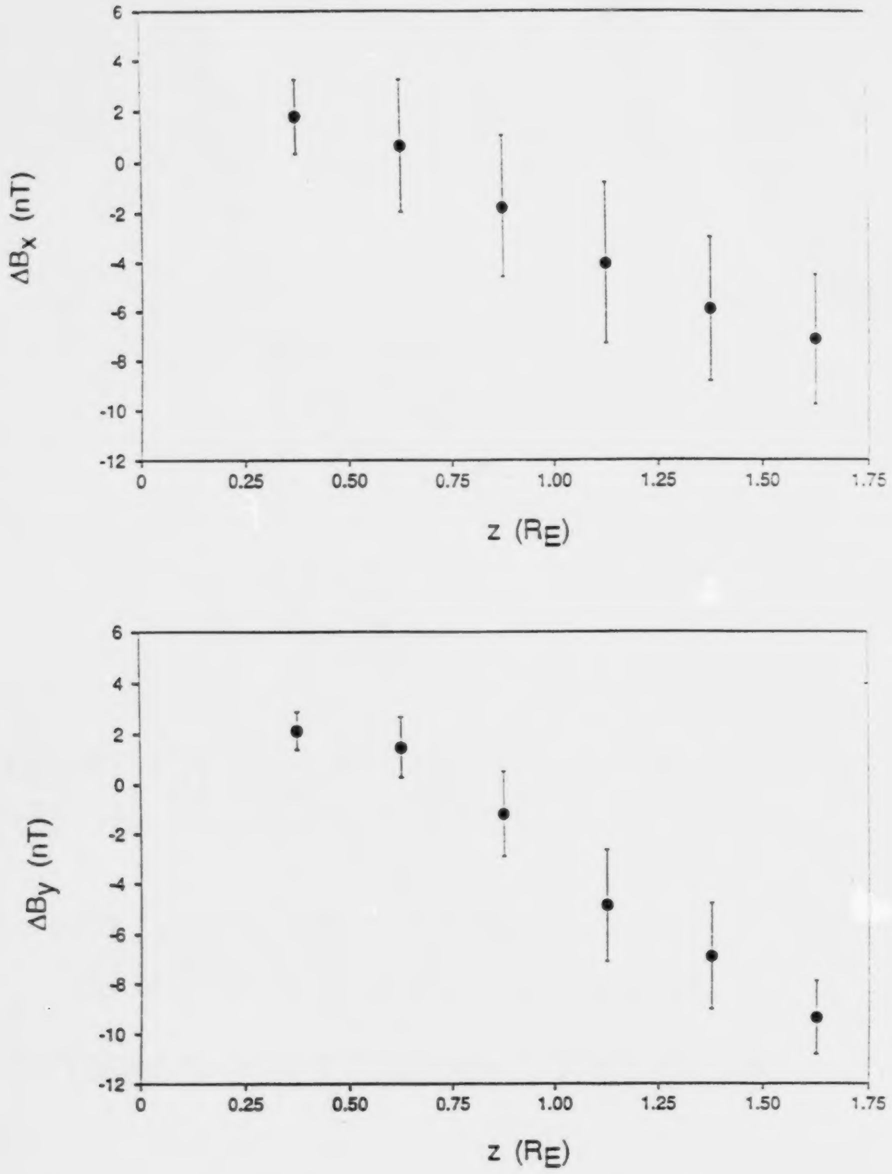

Figure 35. ΔB_X and ΔB_y as a function of perpendicular distance from the neutral sheet, for 18 to 20 MLT.

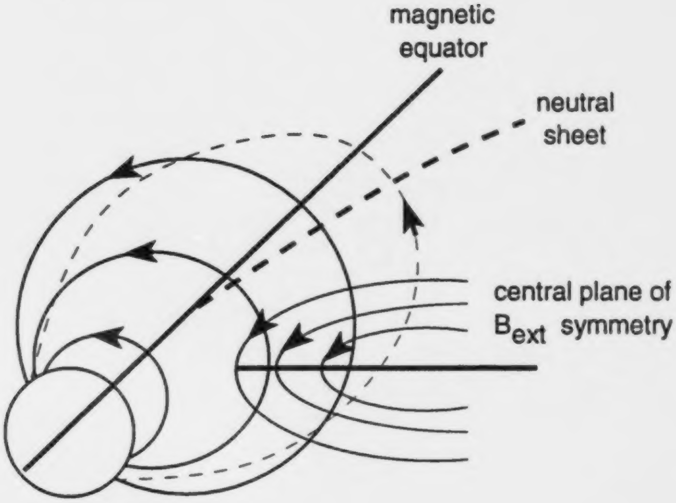

Figure 36. Displacement of the neutral sheet from the magnetic equatorial plane, resulting from a superposition of $\vec{B}_{terr}$ and $\vec{B}_{ext}$. The resultant field is represented by the lighter dashed curve.

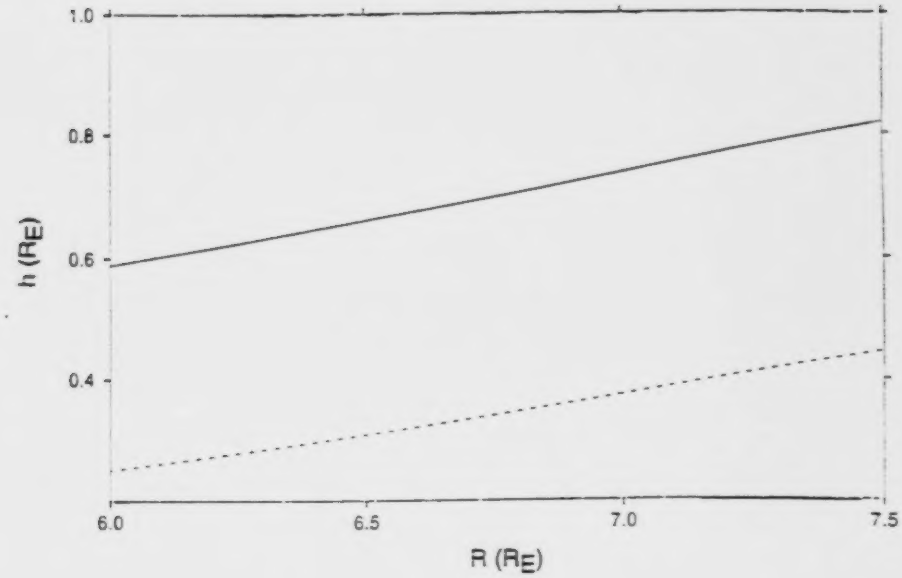

Figure 37. Displacement of the neutral sheet (dashed curve), and displacement of the central plane of current symmetry (solid curve), from the magnetic equatorial plane as a function of radial distance, R. The h values were calculated for Kp=0, $R = 6.6\mathrm{R_E}$, and $\psi = -15$ in the HV plane.

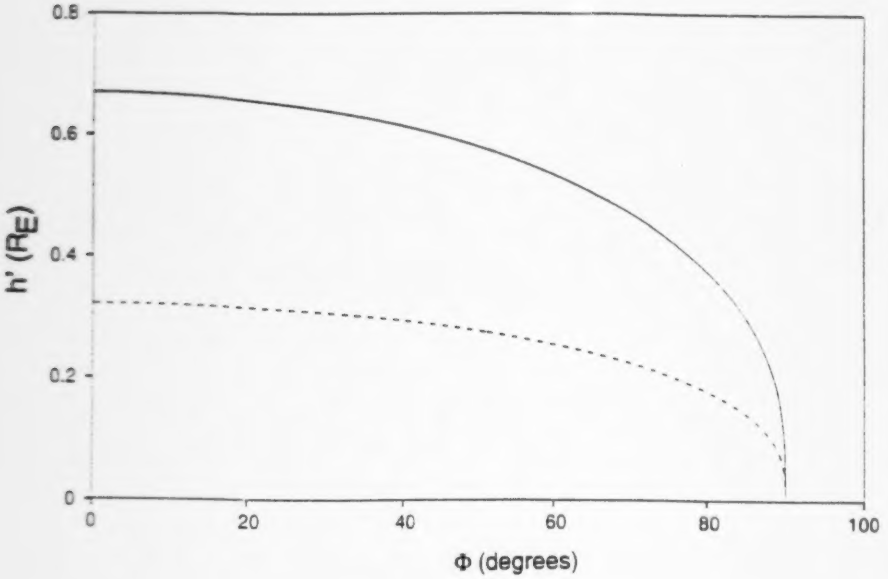

Figure 38. Displacement of the neutral sheet (dashed curve), and displacement of the central plane of current symmetry (solid curve), from the magnetic equatorial plane as a function of local time, Φ, where $\Phi = 0°$ at midnight. The h' values were calculated for Kp=0, $R = 6.6\mathrm{R_E}$, and $\psi = -15$ in the HD plane.

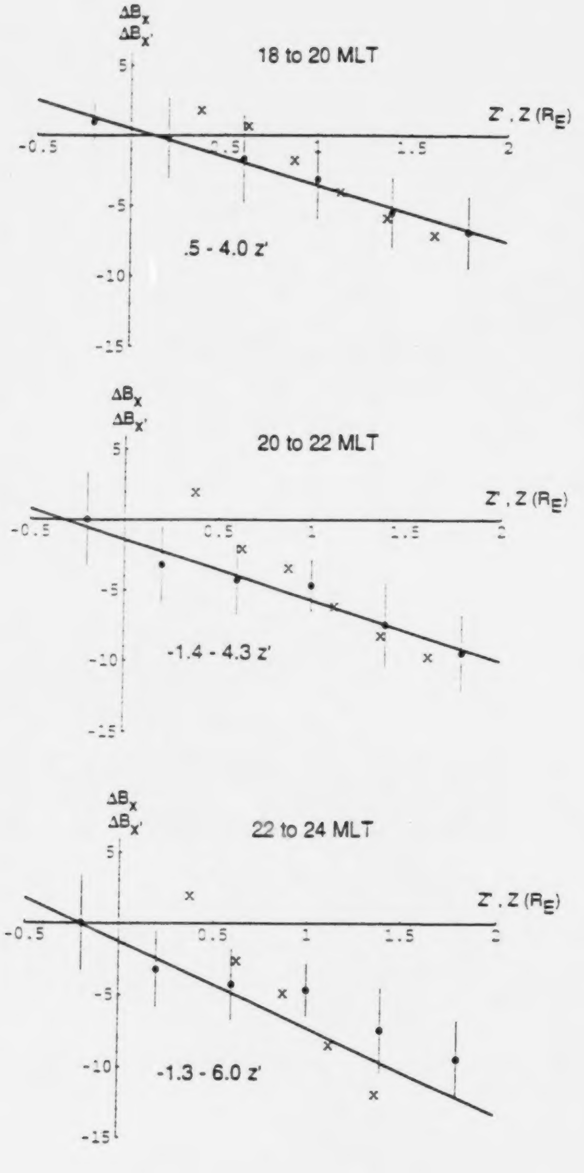

Figure 39. $\Delta B_{x'}$ as a function of distance from the central plane of current symmetry (z'), and ΔB_x as a function of distance from the neutral sheet (z) for different nightside local time sectors. The points plotted with error bars are $\Delta B_{x'}$ and the linear best fit equation for $\Delta B_{x'}$ is included in each graph. ΔB_x are represented by the "x" symbols. This figure is continued on the next page.

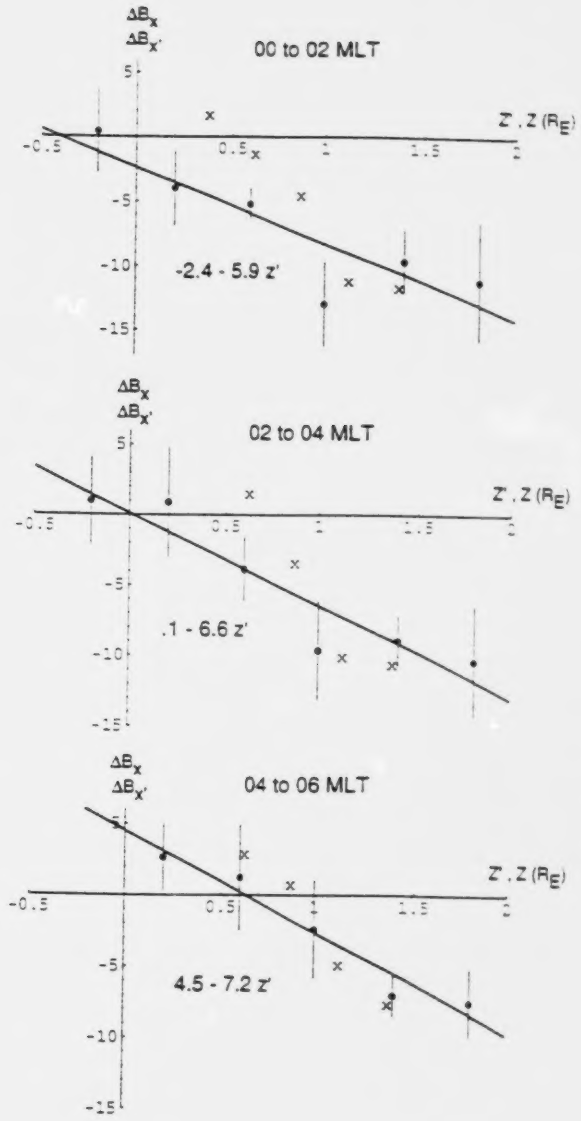

Figure 39 continued.

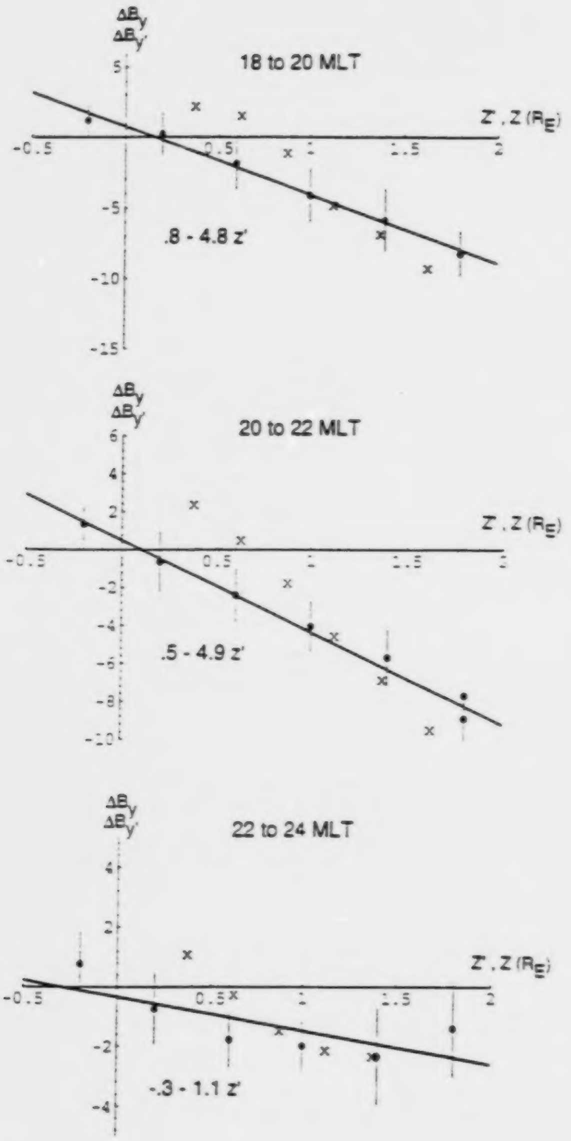

Figure 40. $\Delta B_{y'}$ as a function of distance from the central plane of current symmetry (z'), and ΔB_y as a function of distance from the neutral sheet (z) for different nightside local time sectors. The points plotted with error bars are $\Delta B_{y'}$ and the linear best fit equation for $\Delta B_{y'}$ is included in each graph. ΔB_y are represented by the "x" symbols. This figure is continued on the next page.

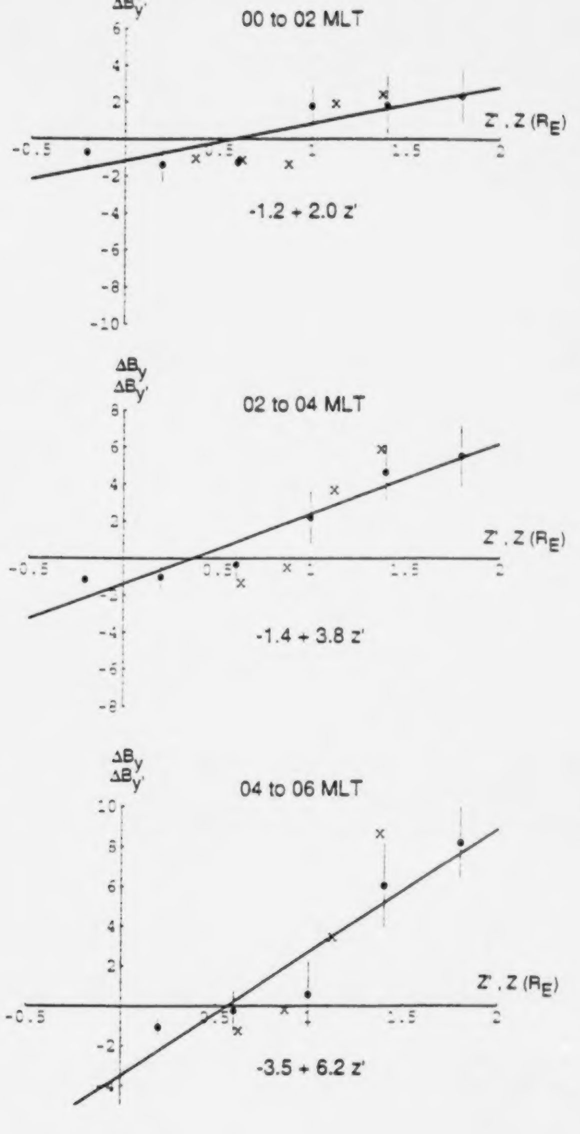

Figure 40 continued.

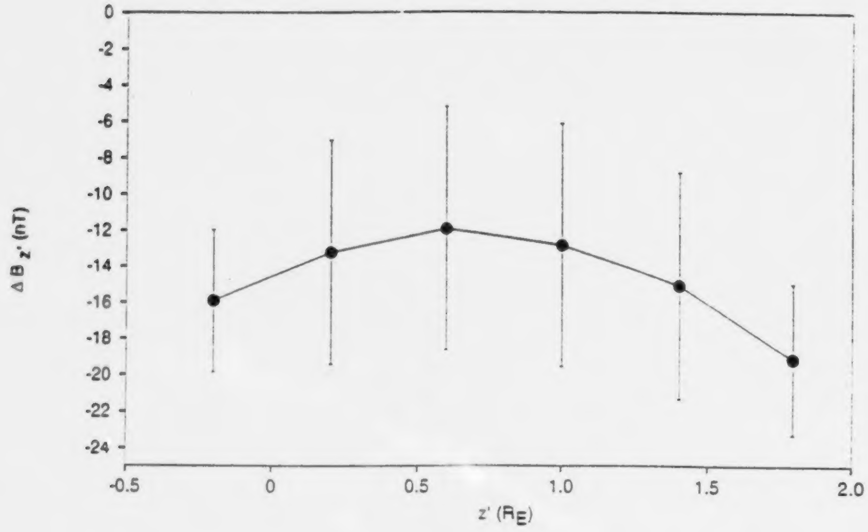

Figure 41. $\Delta B_{z'}$ as a function of distance from the central plane of current symmetry (z'), for the local time sector 18 to 20 MLT.

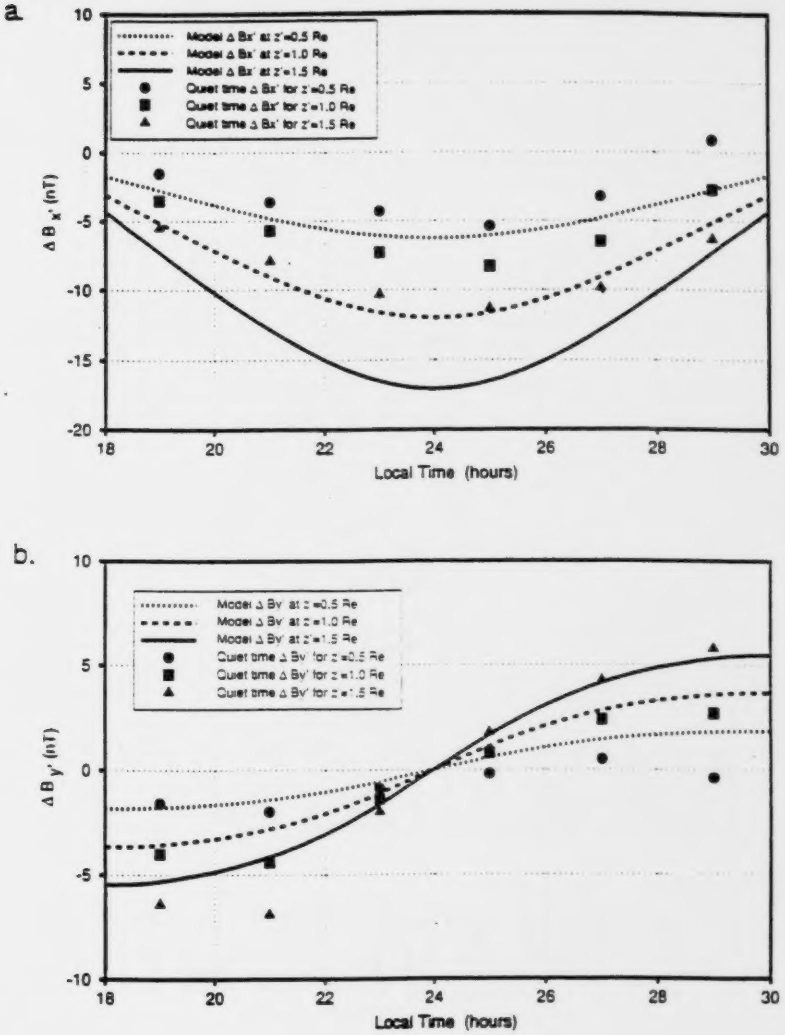

Figure 42a. $\Delta B_{x'}$ as a function of local time for $z' = 0.5$, 1.0, and 1.5 $\mathrm{R_E}$.
b. $\Delta B_{y'}$ as a function of local time for $z' = 0.5$, 1.0, and 1.5 $\mathrm{R_E}$.

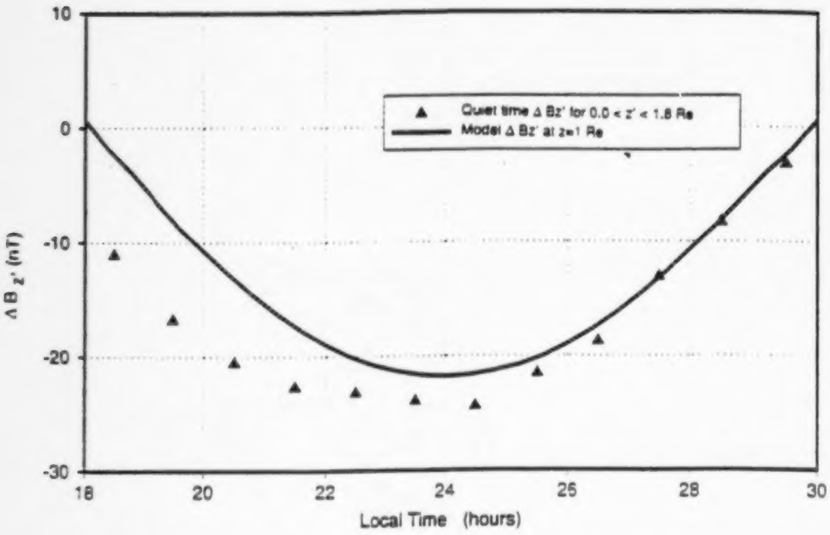

Figure 43. $\Delta B_{z'}$ as a function of local time, averaged for the range $0.0 < z' < 1.8$ $\mathrm{R_E}$.

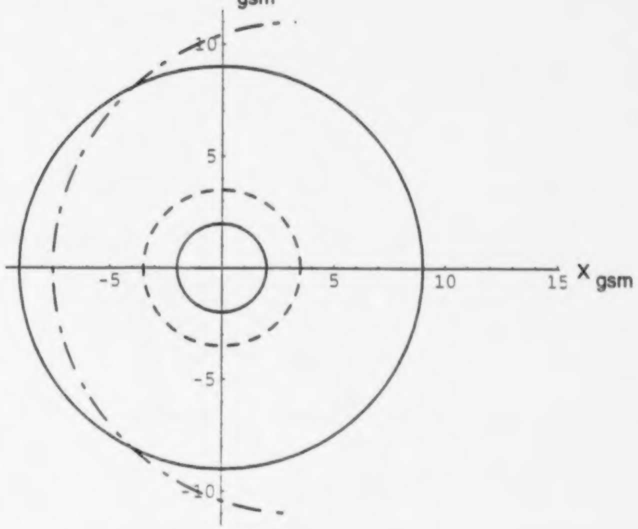

Figure 44. The distribution of ring and cross-tail currents in the XYgsm plane for the quiet time Donovan model. The solid curves represent the boundaries of the ring current region, with the dashed curve separating the east and west ring currents. The dot-dashed curve represents the inner edge of the cross-tail current.

4. SUBSTORM EVENT

A series of auroral substorm intensifications took place in the duskside oval on 3 April, 1986, during the interval ~ 0025 - 0300 UT. This activity was monitored by various ground and satellite detectors. The sector of auroral activity was in the Viking imager field of view during the period 0054 – 0150 UT, and images of the substorm auroral development are therefore available during part of this substorm event. Auroral intensifications identified during the interval of the Viking coverage will be mapped into the magnetosphere. The substorm activity recorded by the Viking imager took place over North America, and U.S. and Canadian ground stations were well positioned in order to measure magnetic signatures associated with this event. The GOES 5 and GOES 6 satellites were also located near field lines threading the sector of auroral activity (near the Poste de la Baleine and Yellowknife geographic meridians, respectively) and made measurements in the near-earth magnetotail throughout the series of intensifications. Additional measurements during this event are also available from the IMP-8 satellite, which is located sunward of the Earth in the solar wind.

EVENT OVERVIEW

Several substorm intensifications are identified in the interval ~ 0025 – 0300 UT, four of which will be discussed in this section. The first intensification began at ~ 0025 UT, near 21.5 MLT. The term "intensification" will be used in the discussion of this substorm event to denote enhanced auroral activity, as identified from Viking images or ground magnetograms, which may be associated either with enhanced directly driven activity or with a substorm current wedge at expansive phase onset. Magnetic field perturbations associated with the ~ 0025 UT intensification are detected at Narssarssuaq, Greenland, which is located at 61.18° N, 314.57° E geographic (70.60° N, 38.66° E geomagnetic). The Narssarssuaq magnetogram is shown in figure 45, and the magnetic field measurements are expressed in the HDZ coordinate system. There is a negative perturbation in the H component of the magnetic field at ~ 0025 UT, indicating the presence of an enhanced westward electrojet across the Narssarssuaq meridian. The Z component of the magnetic field decreases initially, at ~ 0025 UT, and then increases at 0030 UT. These magnetic field perturbations indicate that the intensification begins at high latitudes north of Narssarssuaq, and then expands south of this station at ~ 0030 UT. No similar signatures of this intensification are detected at North American ground stations; this intensification is therefore limited to the sector east of North America.

Two subsequent substorm intensifications, at 0054 UT and at 0116 UT, are recorded by the Viking imager. These intensifications, for which the regions of auroral activity can be determined from the images, are of primary interest during this event, and the regions of auroral activity will be mapped into the magnetosphere for both intensifications. The 0054 UT image is the first available image in the Viking coverage during this orbit and the auroral oval is not entirely in the imager field of view. This initial image, and the next two images in the series, are shown in figure 46. The 0054 UT image shows high latitude intensifications which cover a large longitudinal extent of the oval, from 16.5 MLT to 20.3 MLT. The intensifications have grown stronger in the sector east of Fort Churchill at 0056 UT, and the region of intensification spans a limited latitudinal width: a minimum of .5° of latitude at 1700 MLT, and a maximum of ~ 1.5° of latitude at 2000 MLT. This region of substorm enhanced upward field-aligned current is limited to the North American sector, and signatures associated with the westward electrojet of the substorm current wedge are only detected east of this sector. The Narssarssuaq magnetogram (figure 45) shows large negative perturbations in H and Z at ~0054 UT. Narssarssuaq is therefore located south of the enhanced westward electrojet associated with the substorm current wedge. The initial wedge signature at Narssarssuaq occurs at approximately the same time that the first Viking image is available. The series of Viking images in figure 46 therefore records the initiation and evolution of the auroral features of this intensification.

North American auroral zone stations measure signatures associated with increased directly driven activity at the time of the 0054 UT intensification. The locations of the North American ground stations are shown in figures 13 and 14. Fort Churchill and Poste de la Baleine are located south of the equatorward edge of the surge intensifications, as can be seen in figure 46 where the positions of these stations are marked on the images. Neither of these auroral zone stations measure signatures associated with the substorm wedge, but instead detect an enhancement of the eastward electrojet at the time of this intensification. Figures 47 and 48 show the magnetograms at Fort Churchill and Poste de la Baleine during the interval 0000 to 0300 UT. At 0054 UT, Fort Churchill measures positive perturbations in the X and Y magnetic field components. The X perturbation reflects an increase in eastward electrojet strength, while the Y perturbation may be explained by the effects of an enhanced eastward electrojet which is tilted with respect to the Y axis, and/or the effects of enhanced upward field-aligned current north of Fort Churchill (as identified in the 0054 UT image). Poste de la Baleine measures a positive X perturbation at ~0054 UT. This signature is similar to that seen at Fort Churchill, and Poste de la Baleine also measures an enhancement of the eastward electrojet at 0054 UT. The Z component at Poste de la Baleine is initially negative at 0054 UT, and then becomes positive at ~0056 UT indicating that Poste de la Baleine is located near the equatorward edge of the enhanced electrojet.

The absence of substorm current wedge signatures in the North American sector is also observed in magnetograms at middle latitude stations. Figures 49, 50, and 51 show the magnetograms at Fresno, Tucson and Fredericksburg. None of these stations measure any small-scale wedge signatures at 0054 UT (the middle latitude magnetic signatures associated with a substorm wedge are described in chapter 1). Fredericksburg, however, measures a positive Y perturbation at ~ 0100 UT. This positive perturbation in Y persists until after 0200 UT, and is likely caused by an enhancement of the net upward field-aligned current associated with the directly driven system near 2000 MLT.

Figure 52 shows the Viking images for the period 0114 to 0121 UT. A localized intensification occurs at 0116 UT, and further intensifications (regions of enhanced luminosity) develop in subsequent images, until activity begins to decrease at 0120 UT. The 0116 UT surge develops at the 2000 MLT meridian. The only auroral zone station to measure magnetic signatures associated with this intensification is Poste de la Baleine (figure 48), which is located near the surge meridian. Poste de la Baleine measures a negative Z perturbation, which is larger in magnitude than a simultaneous negative perturbation in X. This is consistent with Poste de la Baleine being located at a lower latitude than the region of intensification (the location of Poste de la Baleine with respect to the surge is shown in figure 52). Middle latitude stations near the sector of the surge intensification, such as Tucson and Fredericksburg (figures 50 and 51), do not measure any signatures of the current wedge associated with the surge. This implies that the wedge is longitudinally localized, such that the field-aligned currents of the wedge are close together, and the effects of the opposing current sheets cancel out at Fredericksburg and Tucson.

Ground magnetograms indicate that an intensification, with a magnetic signature larger in magnitude than those for intensifications recorded by the Viking imager, takes place at 0215 UT in the sector from ~19.5 MLT to ~22 MLT. The magnetic signature of this later intensification is seen at Poste de la Baleine (figure 48). Negative perturbations in the X and Z components occur at ~ 0210 UT, indicating that the intensification is initially north of Poste de la Baleine. The westward electrojet associated with this intensification then expands southwards over Poste de la Baleine such that Z becomes positive. The longitudinal extent of this intensification spans North America. Magnetic field perturbations at Fresno and Fredericksburg (figures 49 and 51) indicate that these stations are inside the wedge (X perturbations are positive at both stations), and in the east and west sectors of the wedge, respectively (Y perturbation negative at Fredericksburg and positive at Fresno).

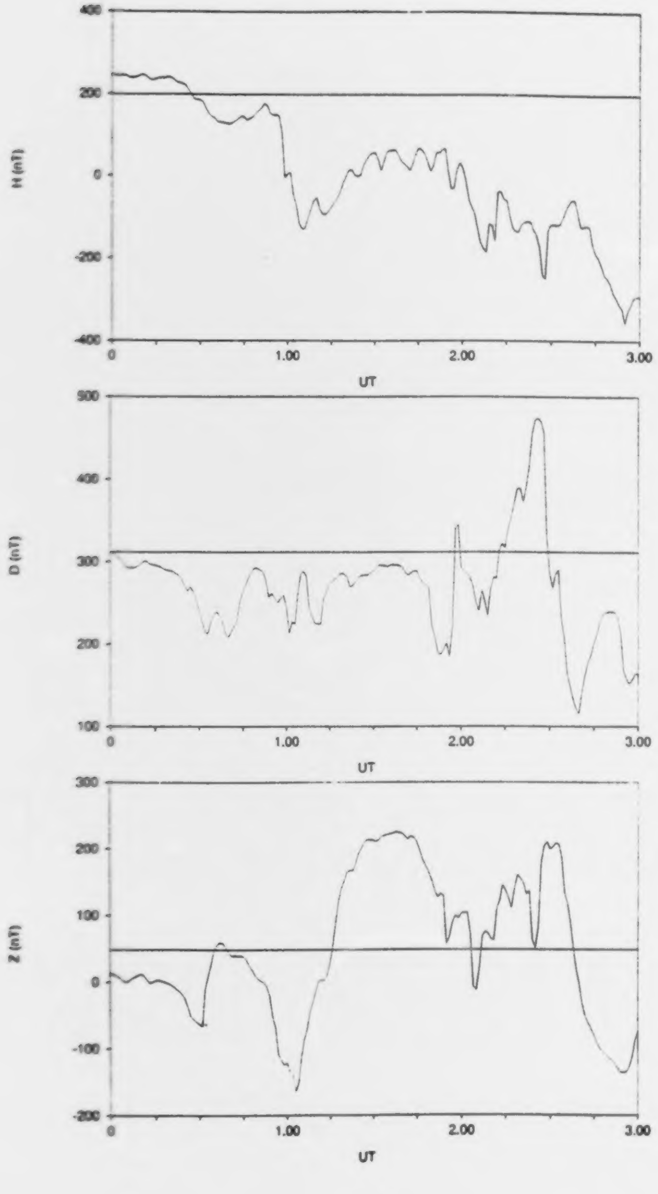

Figure 45. Magnetogram at Narssarssuaq, Greenland for 3 April, 1986. The magnetic field components are expressed in local magnetic (HDZ) coordinates. A quiet time baseline is plotted as a solid line on each graph.

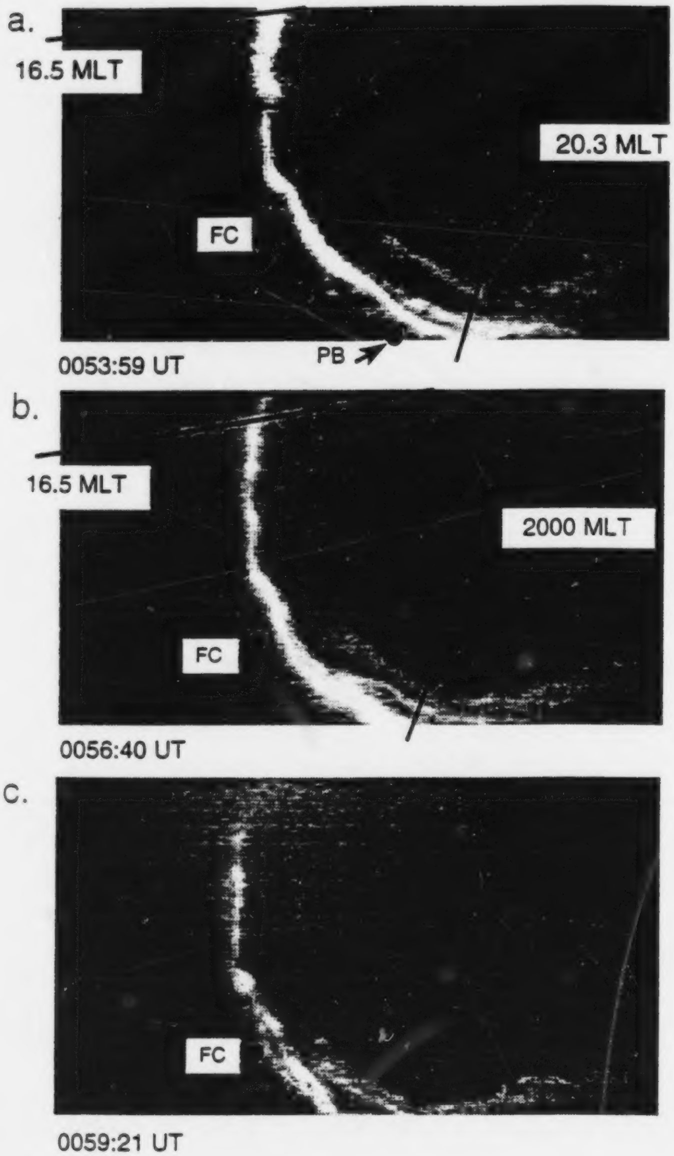

Figure 46. Viking images of auroral intensifications during the interval 0054 to 0100 UT on 3 April, 1986. Magnetic local times are indicated on images a and b. The locations of Fort Churchill (FC) and Poste de la Baleine (PB) are also indicated on the images. Poste de la Baleine is south of the imager field of view after 0054 UT. The images have been provided by Martin Connors.

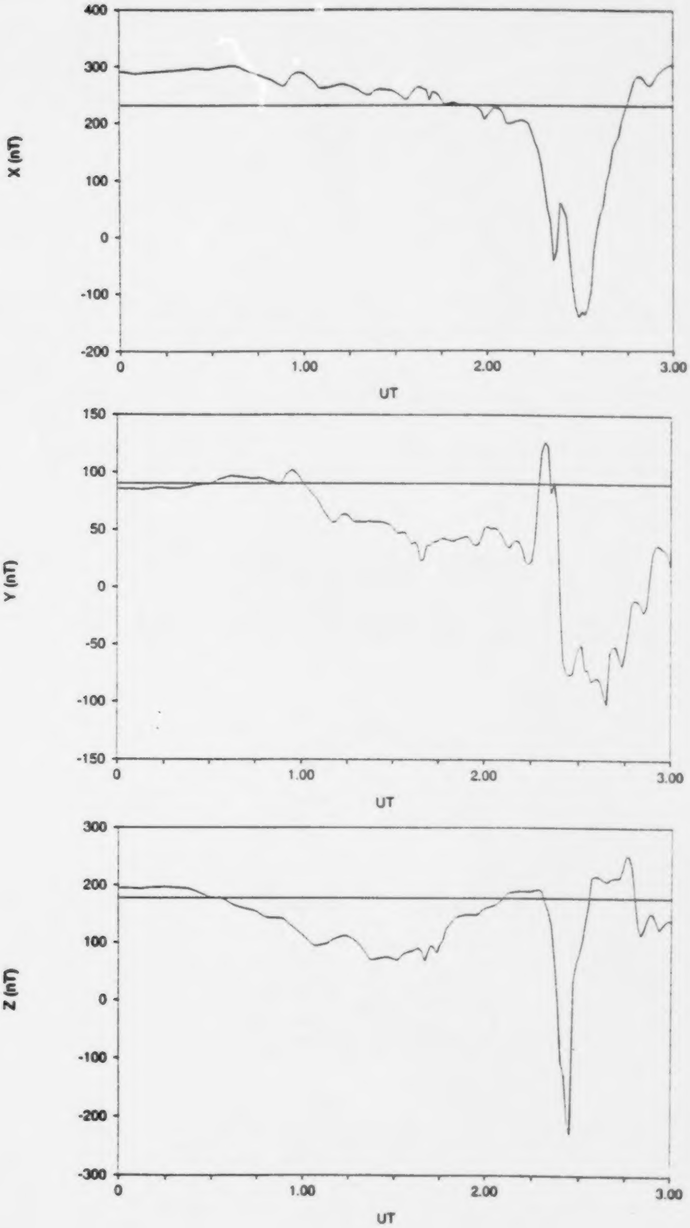

Figure 47. Magnetogram at Fort Churchill for 3 April, 1986. The magnetic field components are expressed in local geomagnetic (XYZ) coordinates. A quiet time baseline is plotted as a solid line on each graph.

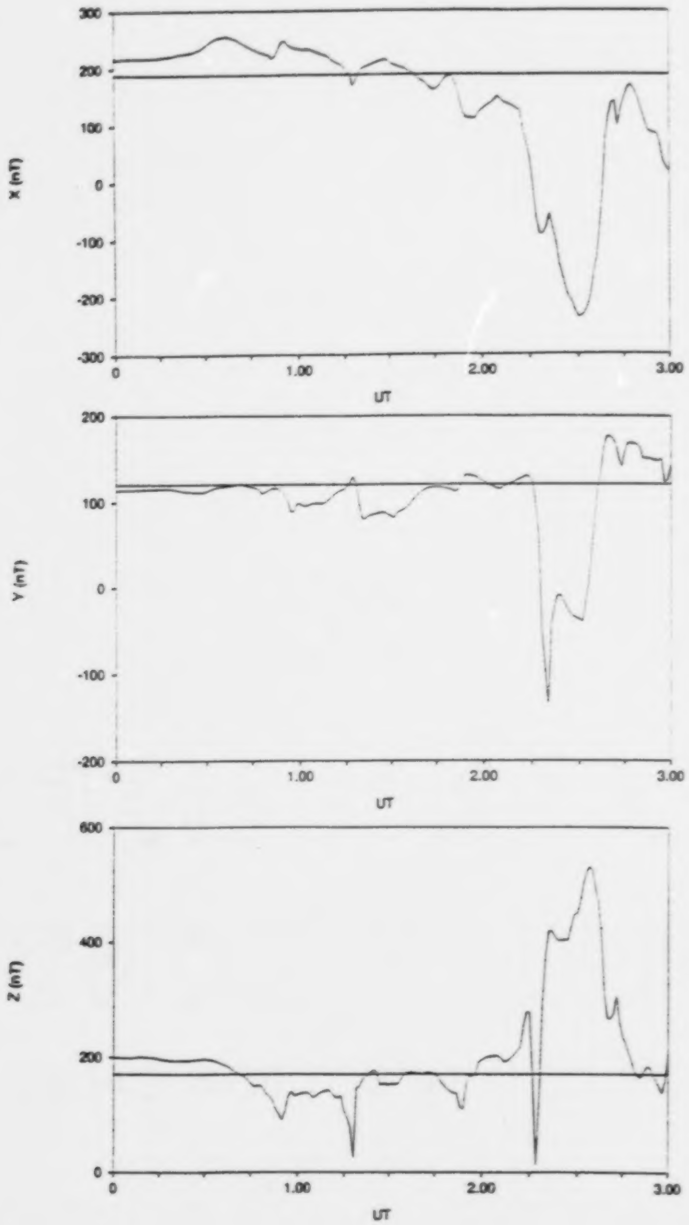

Figure 48. Magnetogram at Poste de la Baleine for 3 April, 1986. The magnetic field components are expressed in geomagnetic (XYZ) coordinates. A quiet time baseline is plotted as a solid line on each graph.

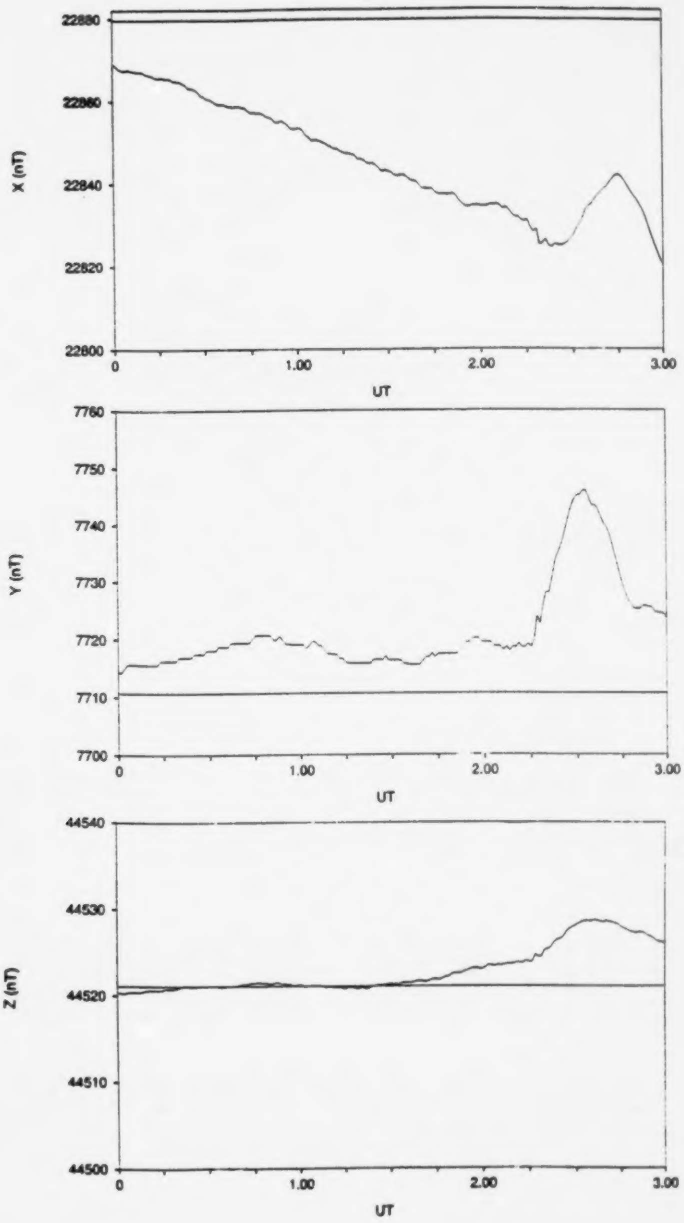

Figure 49. Magnetogram at Fresno for 3 April, 1986. The magnetic field components are expressed in geomagnetic (XYZ) coordinates. A quiet time baseline is plotted as a solid line on each graph.

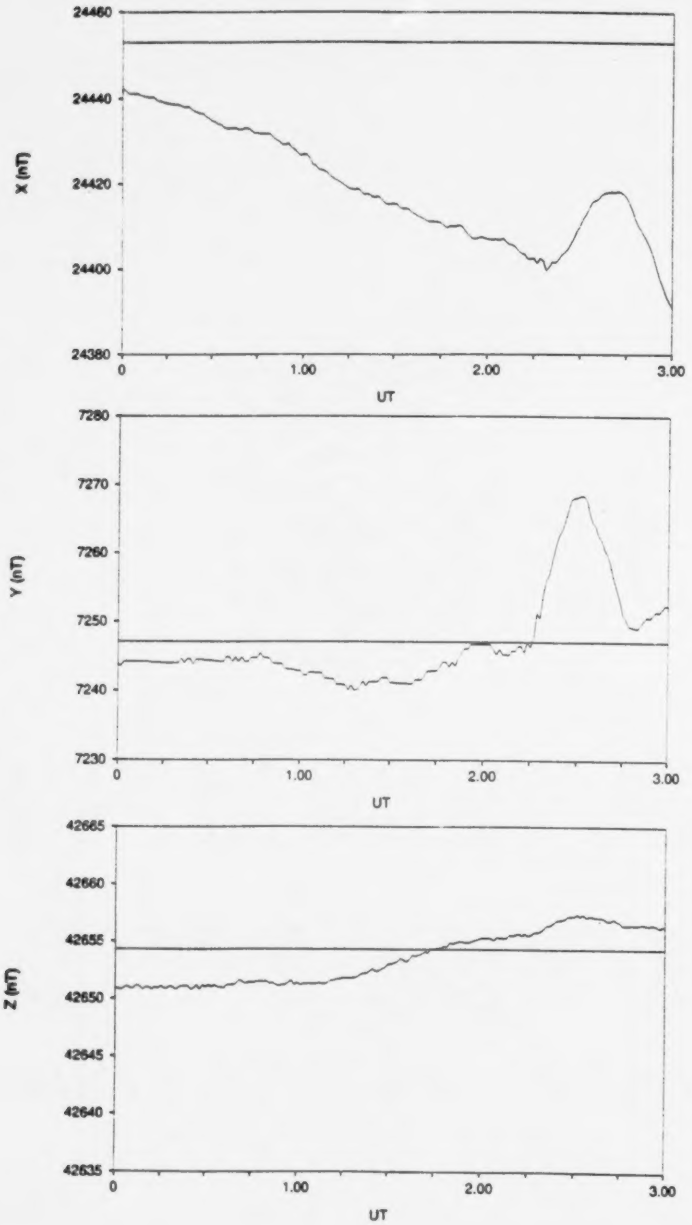

Figure 50. Magnetogram at Tucson for 3 April, 1986. The magnetic field components are expressed in geomagnetic (XYZ) coordinates. A quiet time baseline is plotted as a solid line on each graph.

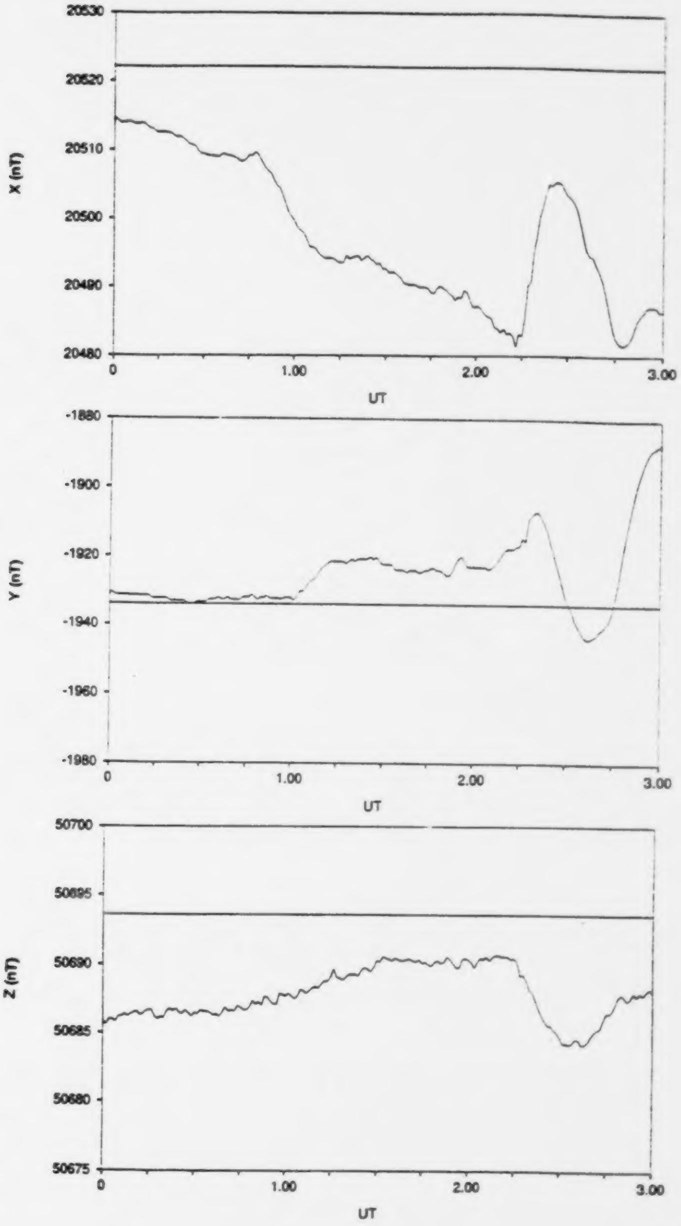

Figure 51. Magnetogram at Fredericksburg for 3 April, 1986. The magnetic field components are expressed in geomagnetic (XYZ) coordinates. A quiet time baseline is plotted as a solid line on each graph.

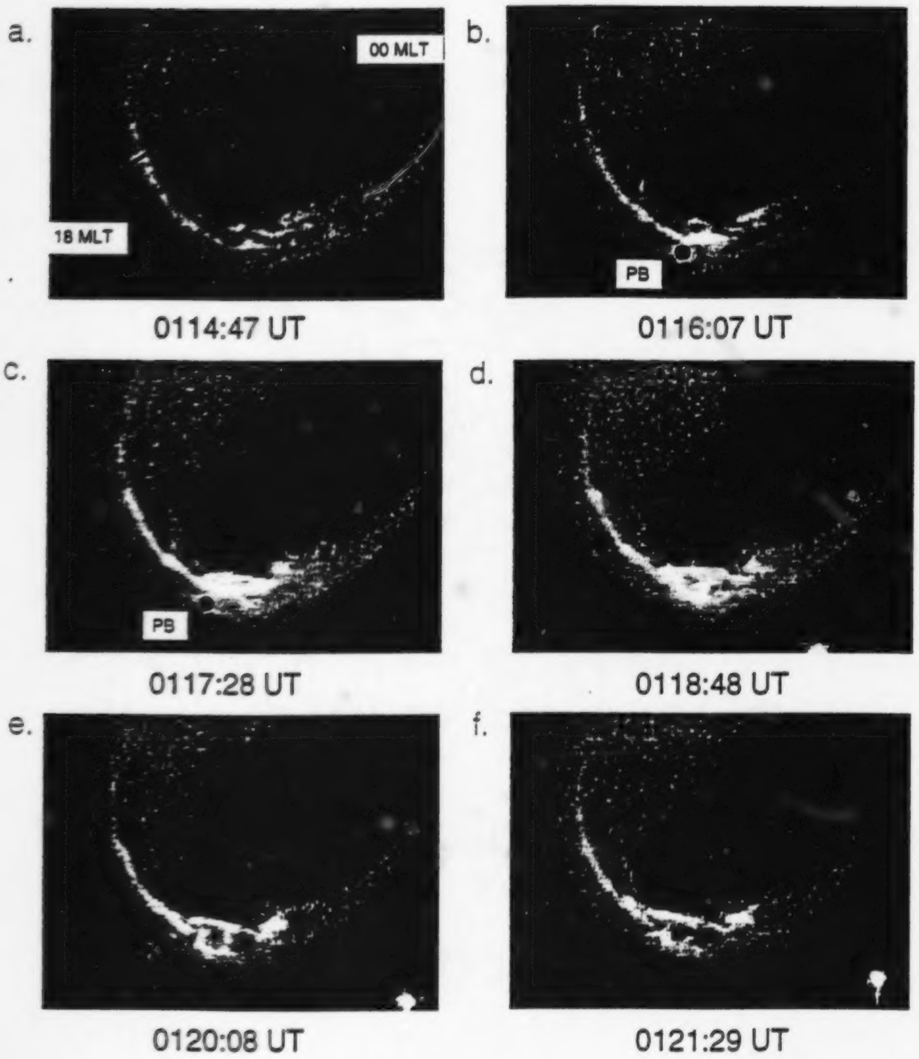

0114:47 UT

0116:07 UT

0117:28 UT

0118:48 UT

0120:08 UT

0121:29 UT

Figure 52. Viking images of auroral intensifications during the interval 0114 to 0121 UT on 3 April, 1986. Magnetic local times are indicated on image a. The location of Poste de la Baleine (PB) is indicated on images b and c. The images have been provided by Martin Connors.

NEAR-EARTH MAGNETOTAIL SIGNATURES AT GOES 5 AND GOES 6

As determined in the event overview, no large substorm current wedge signatures are detected at North American ground stations prior to the 0215 UT intensification. The GOES satellites are located in the North American sector and similarly observe an absence of large wedge signatures during this interval. The development of auroral forms in the North American sector is, however, consistent with the growth of directly driven activity prior to 0215 UT. The magnetic field perturbations at both GOES satellites prior to 0215 UT may be explained in terms of large-scale current systems.

GOES 5 and GOES 6 magnetic field data are plotted in figures 53 and 54 for the interval 0000 to 0300 UT. The IGRF terrestrial magnetic field values have been subtracted from the data in order to consider the magnetic field due to external current systems alone. The magnitude of the dipole tilt angle is less than 2° during the interval 0000 to 0300 UT. Therefore, the neutral sheet, and central plane of current symmetry, are located approximately in the magnetic equatorial plane throughout the interval of interest, and it is appropriate to represent the data in the VDH coordinate system.

Quiet time values of ΔB_V and ΔB_D are calculated from the expressions for $\Delta B_{x'}$ and $\Delta B_{y'}$ in figures 39 and 40, at the positions of GOES 5 (z'=1.28 $\mathrm{R_E}$) and GOES 6 (z'=1.0 $\mathrm{R_E}$). These quiet time values are plotted on the respective graphs in figures 53 and 54. The quiet time values of $\Delta B_{z'}$ from figure 43 are also plotted on the ΔB_H graphs, in figures 53 and 54.

In general, the ΔB_H and ΔB_V components at GOES 5 are lower, and decrease more rapidly across local time, than the quiet time magnetic field values during the interval 0000 UT to 0300 UT. Similar trends in the ΔB_H and ΔB_V components are observed at GOES 6. The magnetic field configuration at geostationary orbit is therefore more taillike in the dusk sector during the period of substorm intensifications than for a quiet time magnetic field configuration. This taillike field configuration during a substorm has been observed by *Lui* [1978] and *Sauvaud and Winckler* [1980], and is caused by a growth in the ring and cross-tail currents downtail of geostationary orbit.

GOES 5 measures a 10 nT increase in ΔB_D at ~0045 UT, such that ΔB_D becomes larger than the quiet time ΔB_D values. Individual ground stations near the GOES 5 meridian do not detect any perturbations associated with a substorm wedge at this time. The increase in ΔB_D at GOES 5 is therefore caused not by field-aligned currents associated with a small-scale substorm wedge, but by the effects of large-scale current systems. A decrease in the strength of the cross-tail current would explain such a positive ΔB_D perturbation. However, the magnetic field at geostationary orbit is more taillike than the quiet time configuration at the time of the positive ΔB_D perturbation, which implies that the cross-tail currrent is in fact stronger than at quiet times. The perturbation in ΔB_D is instead explained in terms of field-aligned current effects.

The positive perturbation in ΔB_D at GOES 5 takes place at approximately the same time as an enhancement and equatorward movement of the eastward electrojet. The Churchill line latitude profile is shown in figure 55. The general construction and interpretation of latitude profiles is discussed in chapter 1. The latitude profiles at 0040 UT and 0050 UT in figure 55 show a ~ 4° equatorward shift in the peak value of X, which is located at the same latitude as the centre of the eastward electrojet. An increase in the peak X value during the interval

0040 to 0050 UT reflects an increase in the strength of the eastward electrojet. The equatorward shift of the electrojet, and auroral oval, is accompanied by an earthward motion of the inner edge of the CPS in the magnetotail. Measurements of energetic electron flux at GOES 5 (figure 56) show a decrease in the energetic electron flux at 0045 UT. This corresponds to an earthward motion of the trapping boundary such that the energetic particle population, and inner edge of the CPS, move earthward of GOES 5. This movement of the trapping boundary takes place in conjunction with an increasingly negative perturbation in the ΔB_H magnetic field component at GOES 5, suggesting that the field becomes more taillike at the GOES 5 meridian. There is therefore an increase and/or earthward motion of the ring and cross-tail currents at 0045 UT which occurs in conjunction with the enhancement of ionospheric currents associated with the substorm. The earthward motion of the CPS is accompanied by an earthward motion of the region 2 field-aligned currents in the equatorial plane, such that the region 2 currents move earthward of the GOES 5 satellite position at ~0045 UT. The GOES 5 ΔB_D perturbation at 0045 UT may therefore be attributed to the effects of region 2 field-aligned currents earthwards of GOES 5, which contribute to ΔB_D in the positive sense. Further ΔB_D perturbations are also explained by a motion of the region 2 field-aligned currents, relative to the satellite position.

At 0054 UT, the time of an auroral intensification, GOES 5 measures an increase in ΔB_H, accompanied by a decrease in ΔB_D and ΔB_V. These magnetic perturbations occur in conjunction with an increase in energetic electron flux at GOES 5. The magnetic field signature in ΔB_D may again be explained in terms of a motion of the trapping boundaries and inner edge of the CPS. The trapping boundaries and region 2 field-aligned currents move tailwards, and there is a corresponding decrease in ΔB_D at GOES 5. A similar decrease in ΔB_D occurs at the time of the 0116 UT intensification, again accompanied by an increase in energetic electron flux and a tailward motion of the region 2 field-aligned currents, at GOES 5. GOES 5 also measures a small dipolarization of the field at 0116 UT, which is most likely the tail signature associated with the localized wedge structure measured at Poste de la Baleine.

Similar explanations describe the ΔB_D perturbations at GOES 6. GOES 6 measures an increase in ΔB_D at 0100 UT, which takes place in conjunction with a sharp decrease in ΔB_H. Particle data at GOES 6 (figure 57) show a decrease of energetic electron flux at $\sim$ 0100 UT, similar to the decrease observed at GOES 5 at 0045 UT. The positive ΔB_D perturbation, relative to quiet time values, at GOES 6 persists until 0215 UT, as does the decrease in particle flux. GOES 6 is near dusk throughout the series of substorm intensifications, and it is likely that the increase in ΔB_D at 0100 UT is due to the satellite moving into the CPS and remaining inside the region 2 field-aligned currents until after 0200 UT. In contrast to GOES 5, no particle injections or magnetic field perturbations associated with substorm intensifications prior to 0215 UT are measured at GOES 6. Small-scale reconfigurations of the magnetic field, and motions of the trapping boundaries, are observed only at GOES 5 in conjunction with the substorm intensifications. The effects at GOES 5 are therefore azimuthally localized.

The magnetotail magnetic field signatures at 0215 UT are consistent with the effects of a substorm current wedge. At $\sim$ 0150 UT, both GOES 5 and GOES 6 measure a decrease in ΔB_H, which indicates a growth in the tail currents just prior to the 0215 UT onset. This growth is also evident in the large negative ΔB_V perturbation at GOES 5. At $\sim$ 0215 UT, the same time that wedge signatures are detected at ground stations in the North American sector, GOES 5 measures perturbations associated with a substorm wedge. There is a dipolarization of the field and an injection of energetic electrons, such that GOES 5 is inside the current wedge. The ΔB_D perturbation from the quiet time baseline changes sign, indicating that GOES 5 is near the centre of the substorm wedge. At GOES 6, both ΔB_V and ΔB_H decrease at 0215 UT, which indicates that GOES 6 is outside the substorm current wedge initially. At 0220 UT, GOES 6 measures a dipolarization of the magnetic field (an increase in ΔB_H and ΔB_V in figure 54) and an injection of energetic electrons (an increase in particle flux in figure 57) as the current wedge passes over the satellite. The ΔB_D component at GOES 6 has a positive peak at the time that the upward field-aligned current of the substorm wedge passes over the GOES 6 satellite. The westward expansion of the wedge is also seen at middle-latitude stations: Fredericksburg measures a positive perturbation in X at 0215 UT, and the same signature is seen at Fresno at 0220 UT.

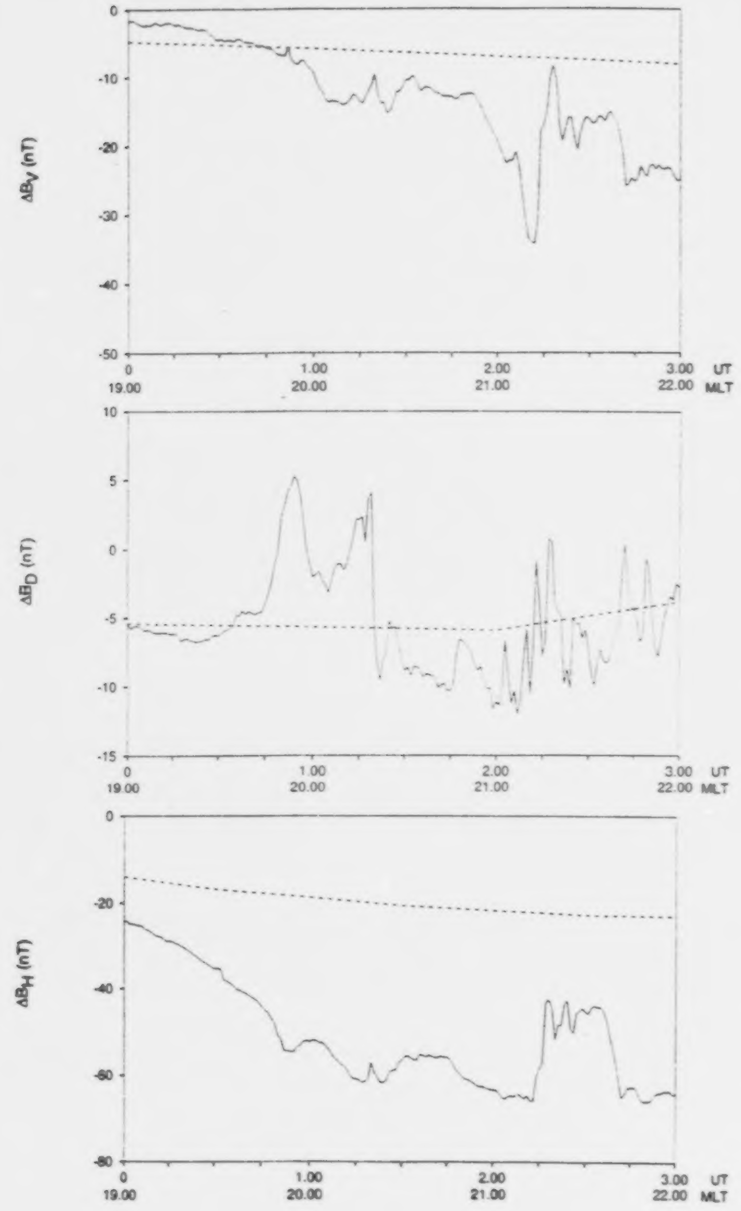

Figure 53. GOES 5 magnetic field measurements, in VDH coordinates, during the interval 0000 to 0300 UT on 3 April, 1986. Quiet time values of the magnetic field are plotted as dashed lines.

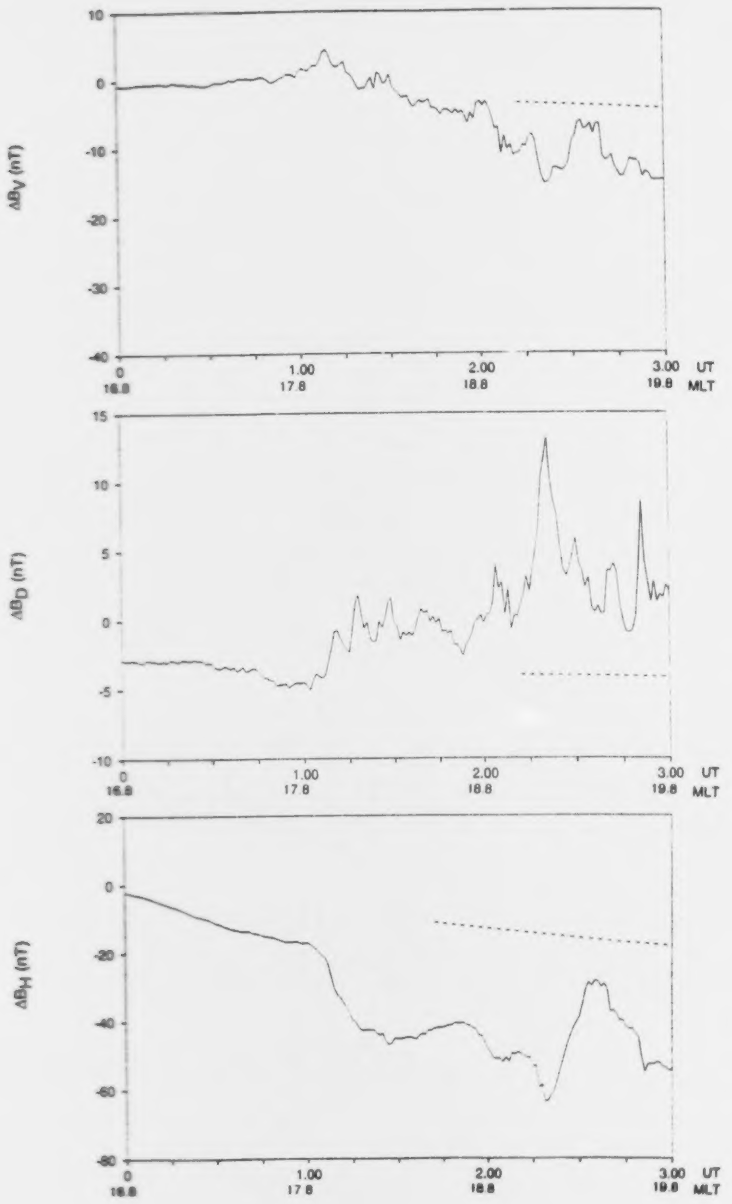

Figure 54. GOES 6 magnetic field measurements, in VDH coordinates, during the interval 0000 to 0300 UT on 3 April, 1986. Quiet time values of the magnetic field are plotted as dashed lines.

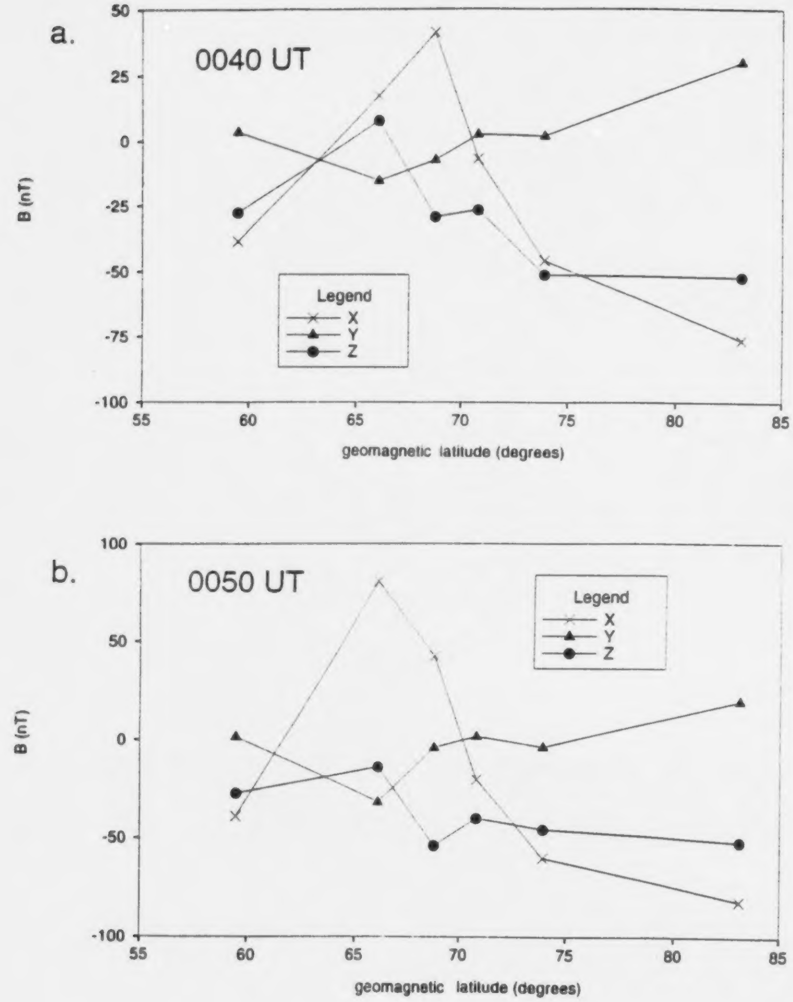

Figure 55. Latitude profiles for the Churchill line at 0040 and 0050 UT, 3 April 1986 in XYZ geomagnetic coordinates. Note the equatorward movement of the *X* peak from ~ 70° at 0040 UT to ~ 66° at 0050 UT.

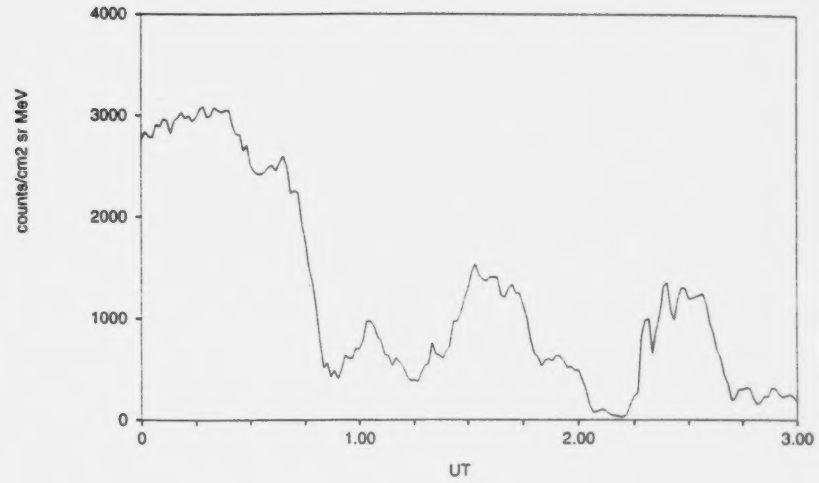

Figure 56. Particle flux at GOES 5, for electrons of energy > 2 MeV, during the interval 0000 to 0300 UT on 3 April 1986.

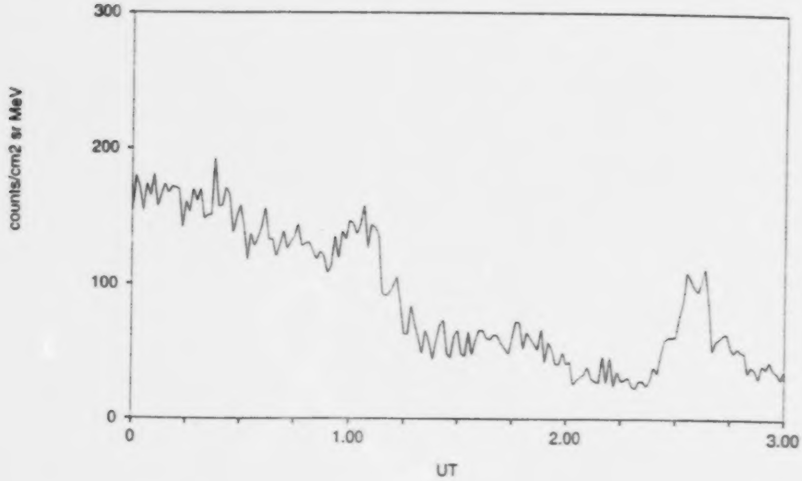

Figure 57. Particle flux at GOES 6, for electrons of energy > 2 MeV, during the interval 0000 to 0300 UT on 3 April 1986.

NATURE OF THE SUBSTORM ACTIVITY

Both the ground and GOES data indicate that there is an enhancement of the directly driven currents during the entire interval of substorm intensifications. Narssarssuaq and Yellowknife are located in the regions of westward and eastward electrojets, respectively, during the interval 0000 to 0300 UT. Magnetic field perturbations in H and X, relative to the quiet time baselines, are negative and positive, respectively, at Narssarssuaq (figure 45) and Yellowknife (figure 58) throughout the interval 0000 to 0215 UT. These magnetic field perturbations are consistent with the presence of enhanced electrojet currents.

As was determined in the previous section, the magnetic field at geostationary orbit becomes increasingly more taillike during the interval 0025 to 0215 UT. This reflects a growth in the ring and cross-tail currents downtail of the GOES satellites. Measurements of X at Fresno, Tucson, and Fredericksburg also indicate a growth of directly driven tail currents during the interval 0000 to 0215 UT. The X values at these middle latitude stations are lower than the quiet time X values, and decrease throughout the interval 0000 to 0215 UT, reflecting a growth in the ring, cross-tail, and magnetopause currents. The cross-tail and magnetopause currents are driven by the solar wind-magnetosphere dynamo and are part of the directly driven system.

IMP 8 is located in the solar wind (at $X_{gsm} \sim 13$ R$_E$ and $Y_{gsm} \sim 33$ R$_E$) during the interval 0025 to 0300 UT and measures a consistently negative $B_{Z_{gsm}}$ component of the IMF during the interval 0000 to 0230 UT (figure 59). Therefore $\theta > 90°$ in the expression for the ε parameter (equation 7) and energy is being injected into the magnetosphere via reconnection throughout the interval of substorm intensifications.

The presence of enhanced directly driven activity throughout the interval prior to 0215 UT is characteristic of the substorm growth phase, as is the increase in ring current strength during the same interval. The buildup of ring current reflects an increase in the deposition of energy in the inner magnetosphere, and this occurs in conjunction with a continued injection of energy into the magnetosphere, as identified in the IMF measurements at IMP 8.

The intensifications prior to 0215 UT are therefore small releases of energy associated with enhanced directly driven activity during the substorm growth phase. The large intensification at 0215 UT is most likely an "unloading" of stored magnetosphere energy which is characteristic of the expansive phase onset. The 0215 UT intensification does not coincide with a northward turning of the IMF, however, and the continued presence of directly driven activity is observed for several hours after the 0215 UT onset.

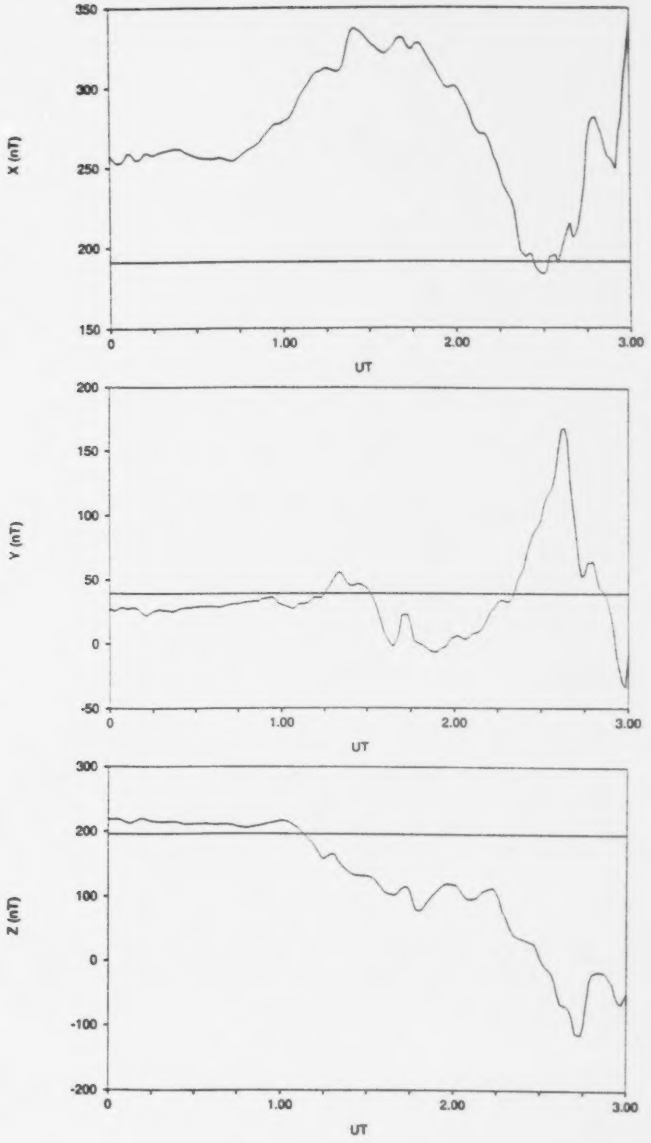

Figure 58. Magnetogram at Yellowknife for 3 April, 1986. The magnetic field components are expressed in geomagnetic (XYZ) coordinates. A quiet time baseline is plotted as a solid line on each graph.

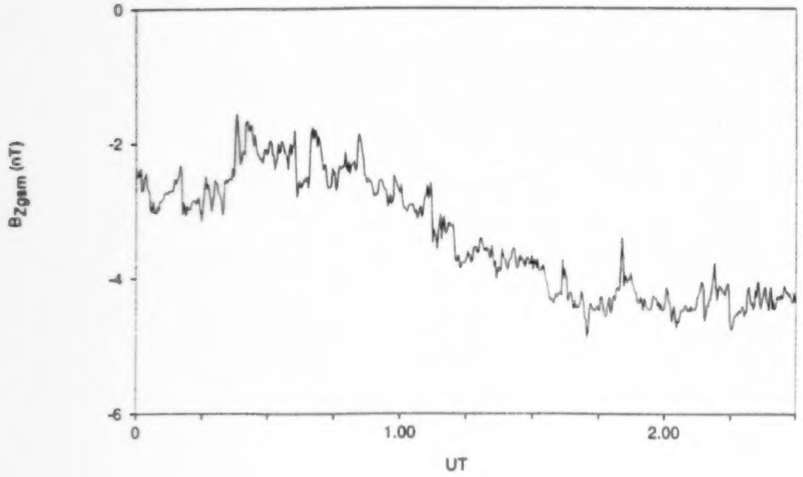

Figure 59. The $B_{Z_{gsm}}$ component of the IMF, as measured at IMP 8, during the interval 0000 to 0300 UT, 3 April 1986.

MODELLING THE SUBSTORM MAGNETOSPHERIC MAGNETIC FIELD AND CURRENT CONFIGURATION

The auroral activity at 0054 UT and 0116 UT, as identified in the Viking images, will be mapped into the magnetosphere using the *Donovan* [1993b] and *Tsyganenko* [1987] magnetic field models. The nature of the magnetospheric activity at the time of these intensifications, as determined in the previous section, is such that these intensifications take place during the substorm growth phase. It is therefore necessary to specify the parameters in each model so as to best represent a magnetospheric growth phase configuration at the time of the intensifications.

The current configuration in the Donovan model was adjusted from the quiet time configuration so as to reproduce the measured magnetic field perturbations from quiet time values at GOES 5 and 6 during the 0054 to 0116 UT interval. The magnetic field perturbations from quiet time values at geostationary orbit, as measured during this interval, are explained in terms of the effects of large-scale directly driven current systems. The Donovan ring, cross-tail, and magnetopause currents were therefore adjusted, and field-aligned currents added to the model, so as to simulate a growth phase current configuration which best matches the magnetic field values at geostationary orbit.

The inner edge of the cross-tail current was placed at X_{gsm} = -7 $\mathrm{R_E}$ at midnight, and the strength of the current was estimated as 30 % larger than the quiet time cross-tail current at this inner edge (so as to simulate the growth of cross-tail current downtail of geostationary orbit during substorm growth phase). The cross-tail current thickness was decreased to one half the value of the quiet time thickness across all local times. This was done in order to simulate the thinning of the CPS during substorm growth phase. The curvature of the cross-tail current was not altered from the quiet time curvature. The magnetic field values representing magnetopause current effects were increased by a factor of 1.50 from the quiet time values. The magnetopause configuration, however, was not changed from the *Sibeck et al.* [1991] average configuration used for the quiet time modelling; it is not possible to alter the magnetopause configuration in the Donovan model.

The ring current configuration in the Donovan model was altered so as to be consistent with ring current profiles calculated by *Lui et al.* [1987] for periods of high activity, as well as match the disturbed magnetic field values at GOES 5 and 6 during the interval 0054 to 0116 UT. Several ring current density profiles from *Lui et al.* [1987], as calculated for periods of high activity, contain peaks in the westward ring current strength that extend over a limited range (less than 2 R_E in radial distance). This peak is not a characteristic of the quiet time ring current. In modelling the ring current during the April 3 substorm event, it was necessary to include such a localized peak of current, in the region -8 $R_E < R_{XY_{gsm}} < -6.5$ R_E downtail, in order to match the GOES 5 and 6 values during the interval 0054 to 0116 UT. The strength of the ring current was also altered throughout the range -9 $R_E < R_{XY_{gsm}} < -2$ R_E so as to match the Dst value measured at the surface of the Earth. The substorm ring current contains 2.8 MA of westward current (distributed in the range -9 $R_E < R_{XY_{gsm}} < -3.5$ R_E), and 0.3 MA of eastward current (distributed in the range -3.5 $R_E < R_{XY_{gsm}} < -2$ R_E). This ring current gives a contribution of -16 nT in the H component at the Earth's surface. The Dst values for 3 April 1986 are shown in figure 60 (the derivation of the Dst index is described in appendix B). At 0100 UT, the Dst value is -25 nT. Multiplying this value by 2/3, to account for induction effects at the surface of the Earth, gives a measured magnetic field at the Earth's surface, due to external currents alone, of -17 nT. The model ring current magnetic field therefore matches the measured value at the Earth's surface very well. This ring current has a dipole moment that is 13 % that of the Earth.

The strength of the field-aligned current at the time of the 0054 UT intensification was estimated from a Churchill line latitude profile (figure 61). The Churchill line was located at 1900 MLT, a sector which is generally in the region of large-scale directly driven eastward electrojet. A one-dimensional Fourier series has been fit to the X values in figure 61b, and the centre of the eastward electrojet is estimated at $\sim 64°$ geomagnetic latitude. A similar fit to the Z values is not possible, due to the lack of stations at lower latitudes in the latitude profile, such that the lower latitude Z peak is not clearly defined. It is evident, however, that a negative Z peak exists at high latitudes which is approximately 60 % of the maximum X value.

Kisabeth [1972] modelled the nightside ionospheric electrojets, including field-aligned currents feeding the electrojets. Figure 62a shows a latitude profile of the magnetic field disturbance for a westward electrojet, with a total electrojet current of 1 MA. The electrojet is fed by field-aligned currents as illustrated in figure 62b. The ratio of the maximum Z value to the maximum H value is 0.67 in the Kisabeth profile, which is within 7% of the Churchill line ratio computed from the data in figure 61. The X component peak in figure 61b is approximately 0.17 of the H peak in figure 62a. Therefore, the total amount of eastward electrojet current at 0054 UT is approximately 0.17 MA. Dividing by the meridian length of the electrojet in figure 62, $Rd\phi = (6.39 \times 10^6 m)(0.09 rad)$, gives an electrojet current density of 0.30 A/m.

Figure 63 shows the Heppner-Maynard model ionospheric electric potential pattern for enhanced activity levels. Near dusk, the electric field is approximately north-south. The Hall currents therefore flow east-west, such that the eastward electrojet is primarily a Hall current and $j_y = 0.30$ A/m (the Y direction is ~ east-west). The ratio of ionospheric conductivities is $\Sigma_H/\Sigma_P = 2/1$ near dusk for high levels of activity [*Wallis and Budzinski*, 1981]. Therefore,

$$\vec{J}_\perp = \Sigma_P \vec{E}_\perp + \Sigma_H \hat{B} \times \vec{E}_\perp$$

gives

$$j_y = \Sigma_H E_x$$

$$j_x = \Sigma_P E_x$$

such that

$$\frac{j_y}{j_x} = \frac{\Sigma_H}{\Sigma_P} = \frac{2}{1}$$

where the X direction is ~ north-south.

The Pedersen current density, j_x, is therefore approximately one half of the Hall current density, and $j_x = .15$ A/m. The strengths of the region 1 and region 2 currents are approximately equal at 1900 MLT [*Kamide*, 1988], and it is therefore assumed that the field-aligned currents close completely through Pedersen currents. The strength of the field-aligned current is therefore equal to the calculated j_x, such that $j_z = .15$ A/m. A similar calculation gives j_z=.20 A/m at 0116 UT. A field-aligned current strength of .16 A/m was used in the Donovan substorm model for the period 0054 to 0116 UT.

The poleward boundary of the Donovan model field-aligned currents was placed along the poleward boundary of the auroral oval. The geographic position of the oval poleward boundary was traced from the images using Viking software, which calculates positional information for an altitude of 120 km. This altitude corresponds approximately to the emission height of the LBH bands to which the Viking camera 0 (which provided the 0054 and 0116 UT images in figures 46 and 52) is sensitive, and the field-aligned currents were placed at an ionospheric height of 120 km in the Donovan model. The equatorward boundary of the field-aligned currents was placed 6 ° south of the poleward boundary. This latitudinal extent of the field-aligned current is consistent with the ionospheric pattern of field-aligned currents developed by *Iijima and Potemra* [1978]. The boundary between region 1 and 2 was placed halfway between the poleward and equatorward boundaries. The region 1 and 2 field-aligned currents were assumed to be of equal strengths and were closed via Pedersen currents in the ionosphere, and via equatorial radial currents in the magnetosphere, in the Donovan model.

Figure 64 shows the magnetic field values produced by the Donovan model at geostationary orbit for the interval 0054 to 0116 UT, across all local times at a height of 1.0 R_E above the neutral sheet (which is approximately the same height as the GOES satellites). Figures 65 and 66 show the model magnetic field values from figure 64, as compared to the observed values at GOES 5 and GOES 6. At both GOES 5 and 6, the model ΔB_H values are generally larger than the measured magnetic field values, while the model ΔB_V values are lower than the measured ΔB_V values, during the interval 0054 to 0116 UT. The model ΔB_D values match the measured ΔB_D values well at GOES 5 and 6 for field-aligned currents included in the model. The addition of field-aligned currents to the model causes model

ΔB_D values to be positive, such that the ΔB_D component is dominated by the effects of field-aligned currents. The 0054 and 0116 UT peaks in ΔB_D at GOES 5 are within a few nT of the model values, while the model ΔB_D matches the ΔB_D value at GOES 6 at 0116 UT. The footprint of the GOES 5 satellite maps to the equatorward edge of the auroral oval for this model magnetic field configuration, which is consistent with the argument that GOES 5 is located near the inner edge of the region 2 field-aligned currents in the magnetotail, such that the ΔB_D perturbations at GOES 5 are caused by a movement of this inner edge with respect to the satellite.

In order to use the Tsyganenko model to map the 0054 and 0116 UT intensifications, only specifications of the Kp index and dipole tilt angle are required. The values of these parameters during the 0054 to 0116 UT interval were Kp = 4 and ψ = -1.0°.

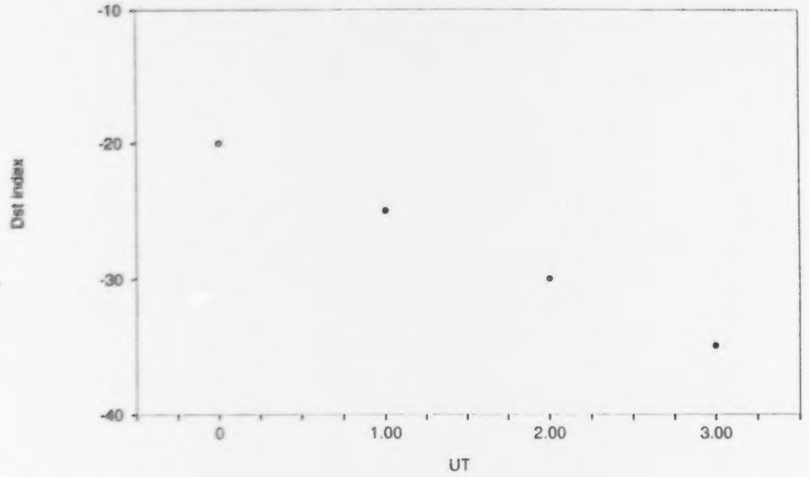

Figure 60. A plot of the Dst index during 0000 to 0300 UT, 3 April 1986.

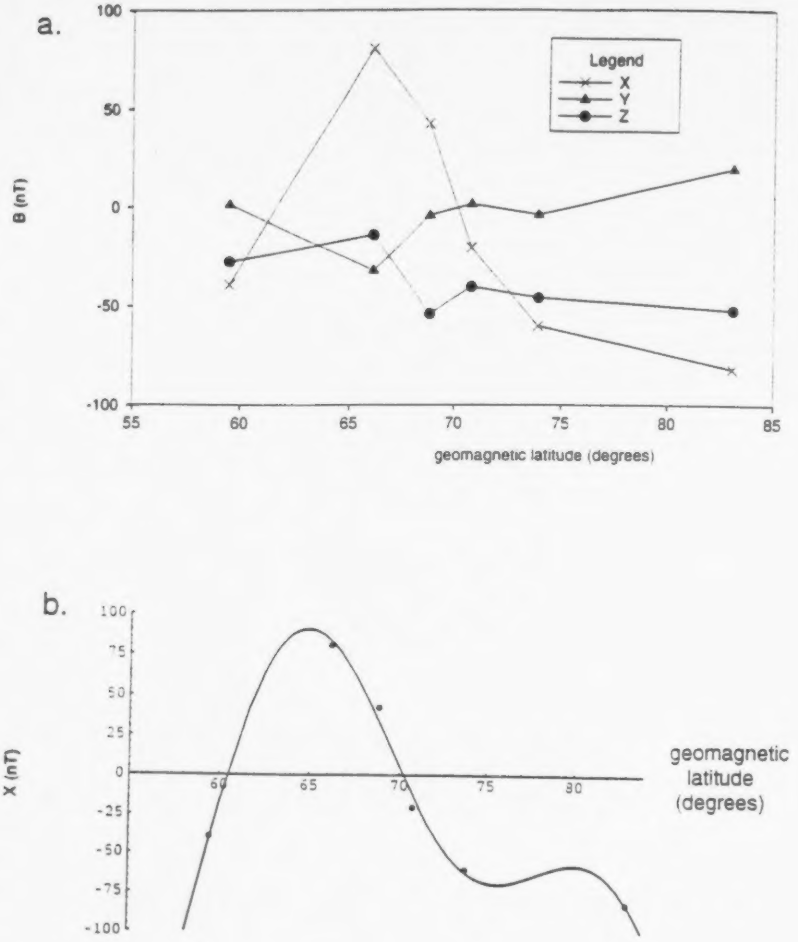

Figure 61a. The Churchill line latitude profile at 0054 UT on 3 April, 1986, in XYZ geomagnetic coordinates.

b. A best fit to the *X* Churchill line values using a Fourier series function.

Figure removed due to copyright restrictions.

Figure 62a. Latitude profile for a westward electrojet and associated field-aligned currents, from *Kisabeth* [1972].

b. Longitudinal current distribution, including field-aligned currents, used to create the latitude profile.

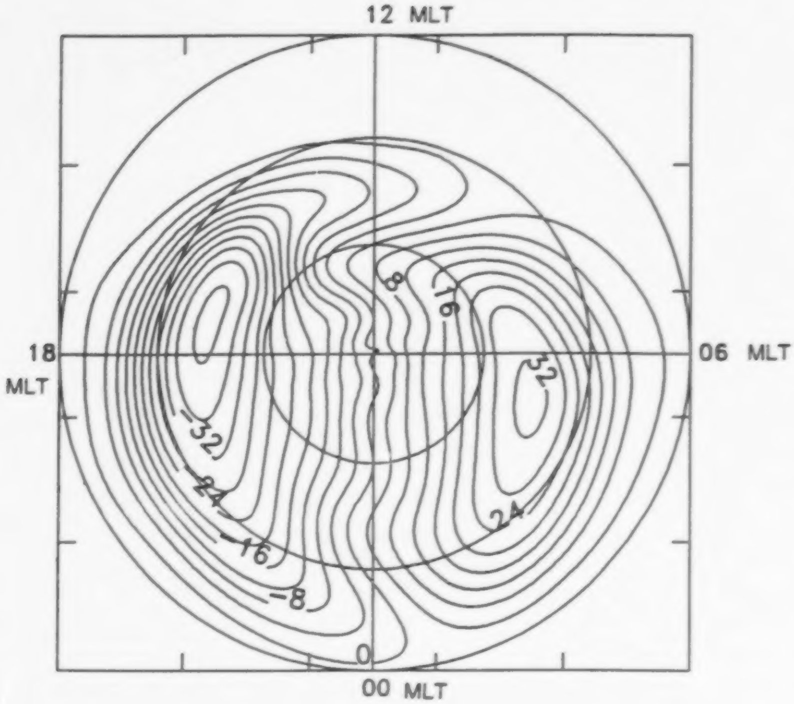

Figure 63. A model ionospheric potential, as calculated for enhanced activity levels from the Heppner-Maynard model. (modified from *Donovan and Rostoker* [1991]).

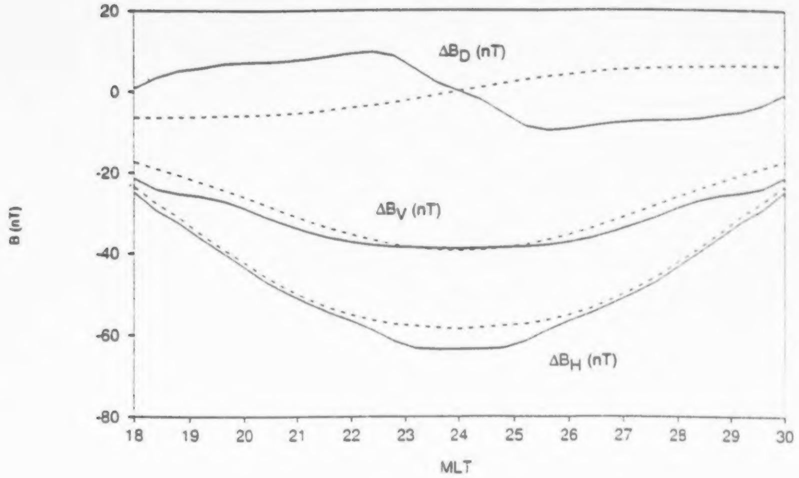

Figure 64. A plot of the Donovan model magnetic field values, as determined for the interval of substorm intensifications 0054 to 0116 UT, 3 April 1986. The solid (dashed) curve represents the magnetic field values for the model with (without) field-aligned currents added. The values are calculated at geostationary orbit, at a height of 1.0 R_E above the neutral sheet.

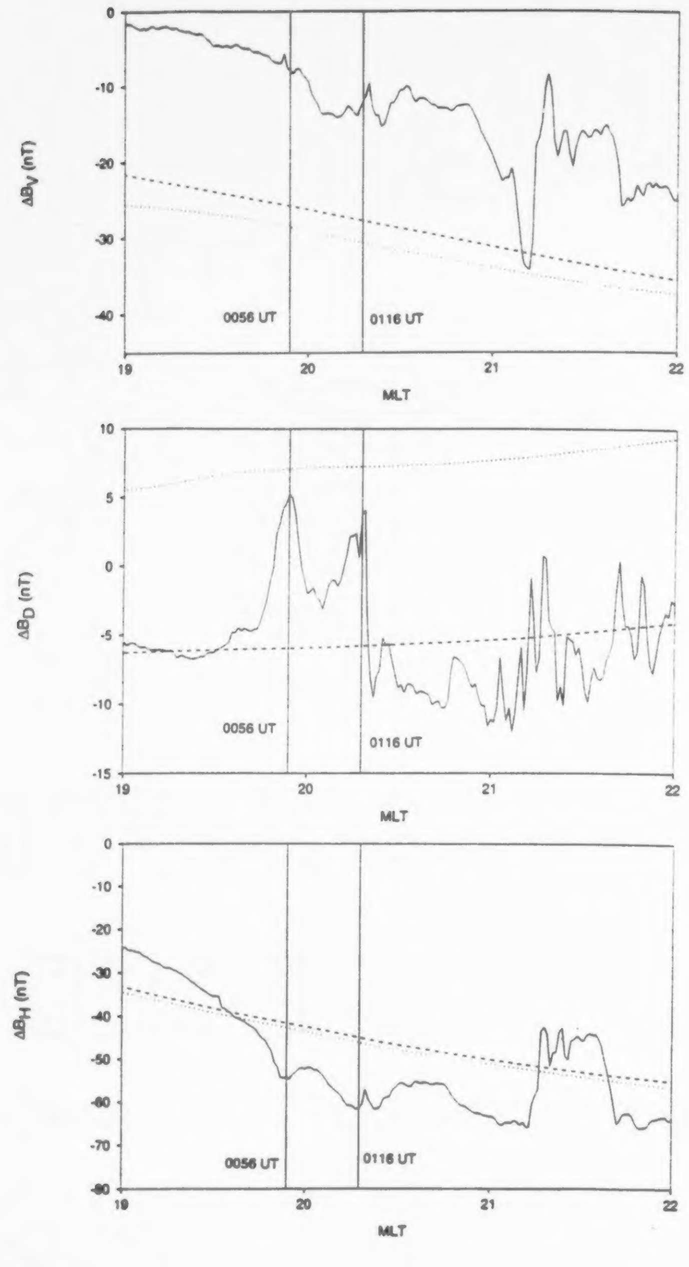

Figure 65. GOES 5 data for 3 April, 1986. Solid vertical lines mark the times of substorm intensifications. The dotted (dashed) curve represents the magnetic field values at geostationary orbit produced by the Donovan model with (without) field-aligned currents for the interval 0054 to 0116 UT.

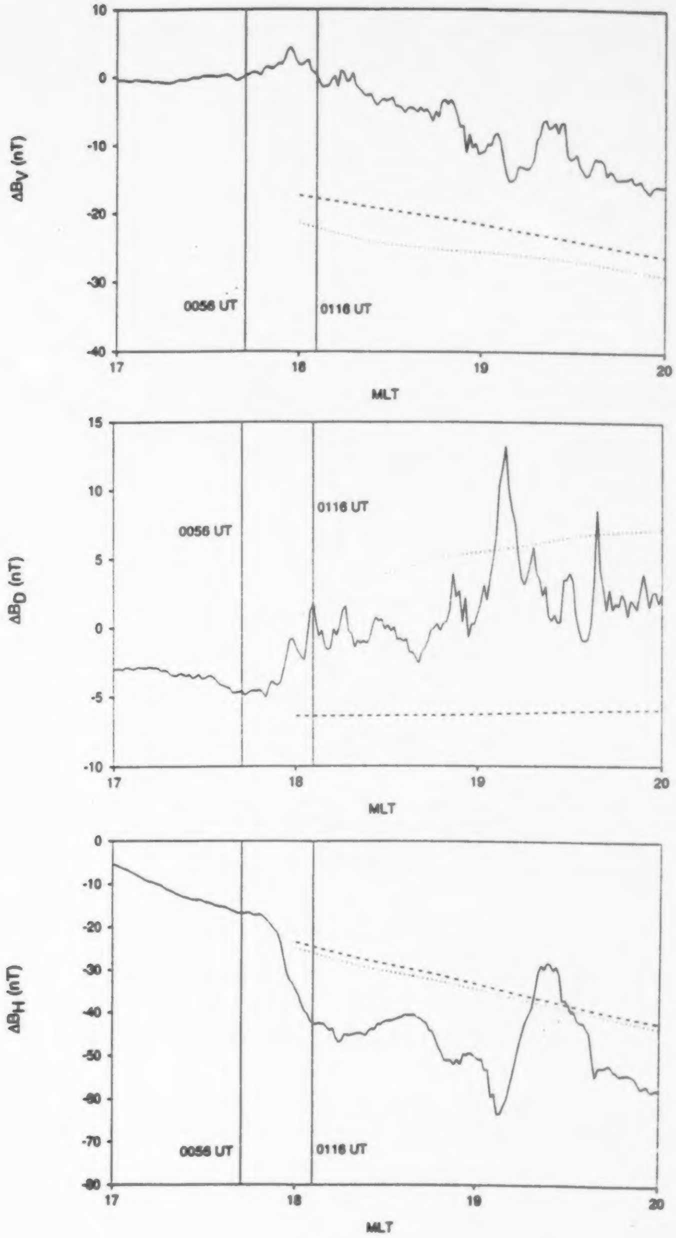

Figure 66. GOES 6 data for 3 April, 1986. Solid vertical lines mark the times of substorm intensifications. The dotted (dashed) curve represents the magnetic field values at geostationary orbit produced by the Donovan model with (without) field-aligned currents for the interval 0054 to 0116 UT.

MAPPING THE AURORAL INTENSIFICATIONS INTO THE MAGNETOSPHERE

Both the 0054 UT and 0116 UT intensifications were mapped in the following manner. The geographic boundary of the region of auroral intensification (where DN = 255) in the Viking image was digitized using the Viking software for both the 0054 and 0116 UT intensifications. The longitudinal extent of the 0054 UT intensification and the boundary of the 0116 UT surge are shown in figure 67. The digitized geographic boundaries (as calculated by the Viking software for a height of 120 km) were then transformed into gsm coordinates, and the magnetic field line passing through each point on the boundaries was traced into the gsm equatorial plane, which was assumed to be colocated with the neutral sheet during this event (since the dipole tilt angle is small). The mappings were done using either the Donovan or T87 magnetic field models to represent the magnetic field values due to sources external to the Earth, and using the 1985 IGRF model to represent the terrestrial magnetic field contribution. The mappings done using the Donovan and T87 models are shown in figures 68 and 69, respectively. The expected position of the magnetopause, as calculated from *Sibeck et al.* [1991], is plotted on both figures 68 and 69.

The points A and B in figure 67 correspond to points A' and B' in figures 68 and 69. In the Donovan mapping, point A (the western ionospheric boundary of the 0054 UT intensification) maps to the dayside magnetopause. Point B (the eastern ionospheric boundary of the 0054 UT region of intensification) maps to approximately the same Y_{gsm} value as point A , but farther downtail. The 0116 UT surge maps to a region which is localized in Y_{gsm}, but covers a range of ~ 10 R_E in X_{gsm}.

The T87 mapping differs greatly from the Donovan mapping for the 0054 UT intensification. Point A maps to the magnetopause, at a distance of 20 R_E downtail, while point B maps closer to the centre of the tail, at a distance of 10 R_E downtail. The T87 model therefore maps the western region of the 0054 UT intensification farther downtail than the eastern region, while the opposite is true for the Donovan mapping of this intensification. The T87 mapping of the 0116 UT surge is in approximately the same X_{gsm} range as the Donovan mapping of the surge, but is closer to the centre of the tail.

The differences in the Donovan and T87 mappings are a reflection of inherent differences between the models. The magnetotail currents in the Donovan model are restricted to the region along, or inside of, the magnetopause. The magnetotail currents in the T87 model, however, are not confined to a region of space inside a defined magnetopause. The cross-tail current is instead modelled with current sheets that extend infinitely in the dusk-dawn and antisunward directions, the magnetic effects of which are tapered for increasing values of Y_{gsm}. The lack of a magnetopause bounding the cross-tail current in the T87 model leads to inaccuracies in the model magnetic field near the flanks of the magnetotail. Figure 70 shows T87 mappings for circles of constant geomagnetic latitude and for lines of constant local time. The mappings were done for Kp=0,0+ and Kp=2,2+. In figure 70b, for the higher activity level, there are regions near the flanks of the tail (in the range $|Y_{gsm}| > 16$ R_E and -15 R_E $< X_{gsm} < -3$ R_E) where the magnetic field is extremely weak and no magnetic flux crosses the equatorial plane. *Fairfield* [1991] refers to these regions as "neutral regions". The closed field lines which cross the XY_{gsm} equatorial plane in figure 70b are restricted to the range inside of these neutral regions: $|Y_{gsm}| < 16$ R_E. This boundary value of $Y_{gsm} = \pm 16$ R_E does not, however, correspond to the position of the magnetopause. The magnetopause configuration can be calculated from *Sibeck et al.* [1991] for an average level of activity, and the magnetopause is located at $Y_{gsm} = 22$ R$_E$ for $X_{gsm} = -15$ R$_E$ and $Z_{gsm} = 0$ R$_E$. The T87 neutral regions therefore lie inside of the true magnetopause, and model magnetic field values are unrealistic at the flanks of the tail. The T87 magnetic field model is too taillike in the near-earth magnetotail range $|Y_{gsm}| > 16$ R$_E$ for Kp=2,2+.

The existence of similar neutral regions in the T87 model for Kp=4 would explain why point A maps farther downtail than point B in figure 69. Regions of extremely weak magnetic field near the flanks of the tail cause field lines originating near dusk in the ionosphere to extend far downtail before crossing the equatorial plane. In figure 70b, field lines with ionospheric footprints on the dayside are swept back into the "neutral regions" predicted for the near-earth flank regions of the tail. *Fairfield* [1991] compared mappings for two ionospheric points on the dayside that were done using the T87 model with Kp=2. *Fairfield* noted that a field line originating at 74° latitude and 8.100 MLT in the ionosphere mapped to X_{gsm}=-3.2, Y_{gsm}=-17.2, while a field line originating at the same latitude, but at 8.107 MLT, mapped far back into the tail. It therefore seems reasonable that the magnetic field line passing through point A (which is located at 16.3 MLT, $\sim 73°$ N geomagnetic latitude) is swept into the tail, and along the flank, such that the field line passes through the neutral region of weak magnetic field and is stretched far downtail. Such effects cause the western region of the 0054 UT intensification to map farther downtail than the eastern region near point B. The Donovan model does not contain such neutral regions near the flanks, and point A maps to the dayside using the Donovan model. The regions of weak magnetic field near the flanks of the tail are an unrealistic feature of the T87 model, and mappings of ionospheric activity into these regions of the tail must be considered unreliable. It is likely that the western region of the 0054 UT intensification actually maps much closer to the Earth.

The Donovan and T87 mappings are more similar for the activity which takes place closer to midnight in the ionosphere. The 0116 UT surge develops at 2000 MLT. This surge maps to the region -17 $\mathrm{R_E} < X_{gsm} < -7\ \mathrm{R_E}$ in the magnetotail for both models, but the T87 model maps this intensification closer to midnight than does the Donovan model.

The difference between the two mappings may be attributed to the lack of field-aligned current effects in the T87 model. The effects of field-aligned current were incorporated into the Donovan model, but it has been shown that the T87 model does not include these effects [*Donovan*, 1993b]. Figure 71 shows a comparison of the ΔB_D components at geostationary orbit, as calculated from the Donovan and T87 models for the interval 0054 to 0116 UT. The Donovan ΔB_D is approximately 10 nT larger than the T87 ΔB_D in the evening sector. It was shown in the previous section that the Donovan model ΔB_D matched the ΔB_D observations at geostationary orbit, which were attributed to the effects of field-aligned currents, during the interval 0054 to 0116 UT. The effects of field-aligned currents are therefore present in the Donovan model, but not in the T87 model. The presence of a positive ΔB_D in the dusk sector suggests that the field lines in the Donovan model are flared towards the flanks of the magnetotail in the near-earth region, while the field lines in the T87 model are flared in the opposite sense.

Donovan [1993a] added field-aligned currents to the T87 model and found that the mapping of a high latitude field line into the near-earth region, for a field-aligned current strength similar to that observed during the 0054 and 0116 UT intensifications, was altered by ~5 R_E in a direction towards the flanks of the tail. The T87 mapping of the 0116 UT surge is ~5 R_E closer to the centre of the tail than the Donovan mapping of this surge. An addition of field-aligned current effects to the T87 model would therefore cause the T87 mapping to be comparable to the Donovan mapping for the 0116 UT intensification.

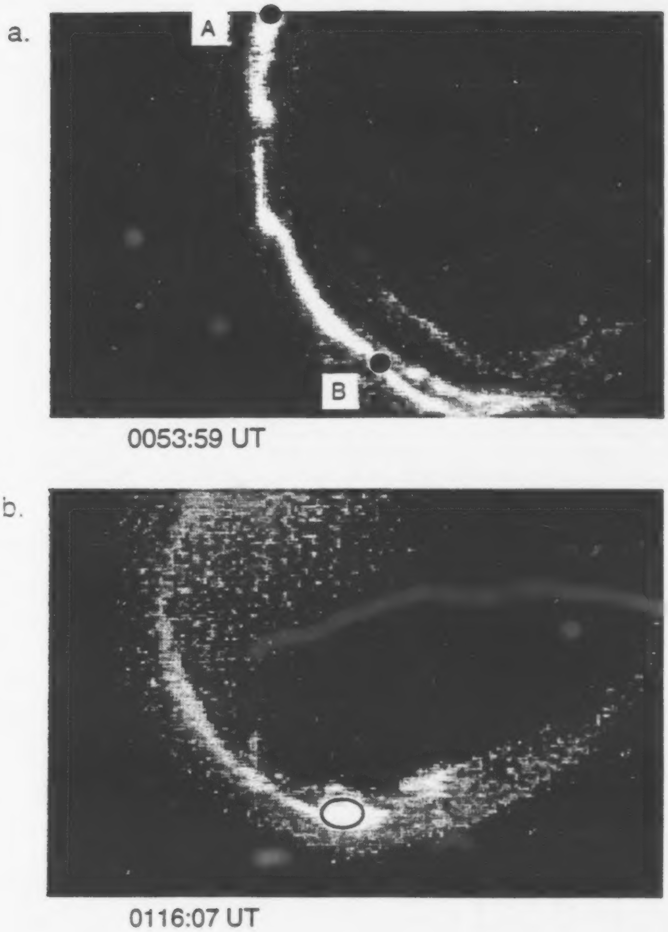

Figure 67a. The region of intensification in the auroral oval at ~ 0054 UT. The thin band of greatest luminosity between points A and B is traced and mapped into the magnetosphere. The region of intensification has a latitudinal width between .5° and 1.5°.

b. The surge at ~ 0116 UT. The region of greatest luminosity within the circular boundary is traced and mapped into the magnetosphere.

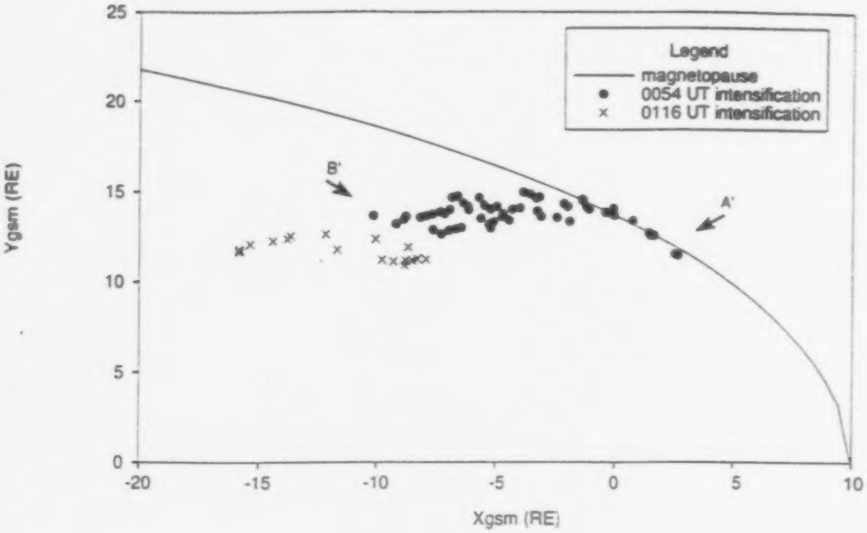

Figure 68. Donovan model mappings of the substorm intensifications at 0054 and 0116 UT in the XY_{gsm} plane.

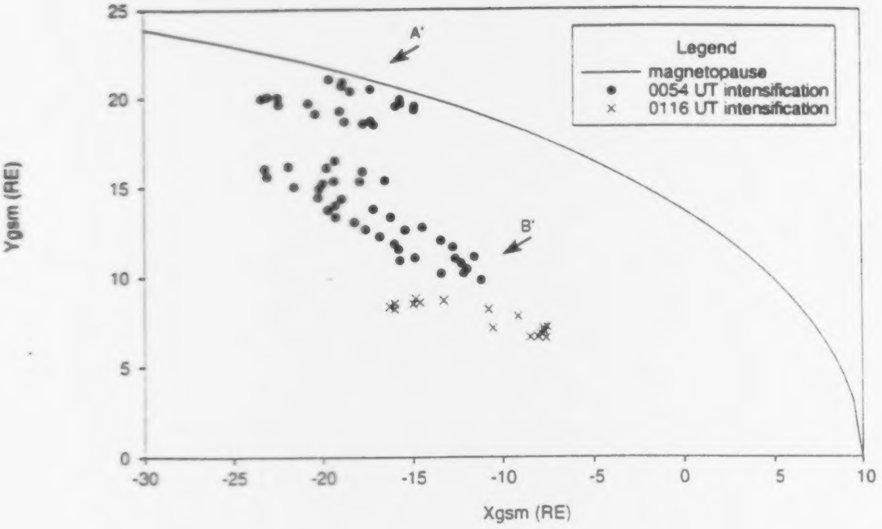

Figure 69. T87 model mappings of the substorm intensifications at 0054 and 0116 UT in the XY_{gsm} plane.

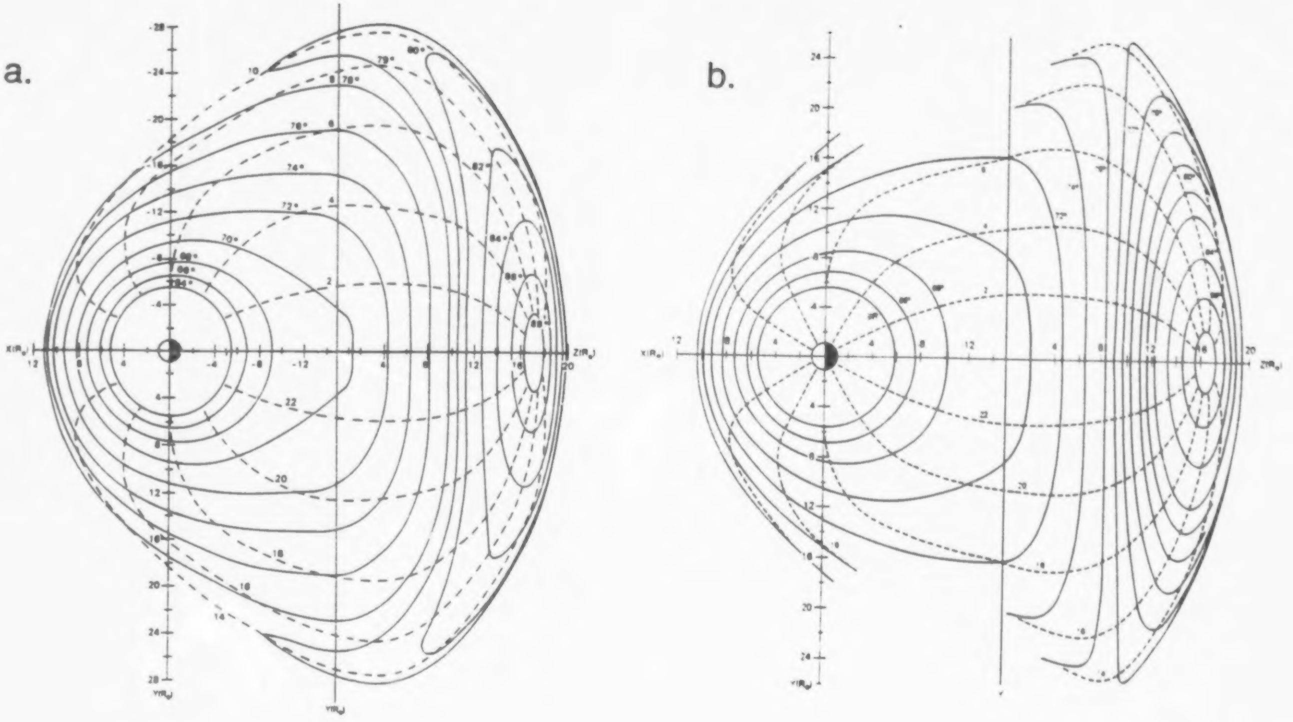

Figure 70a. Mappings of circles of constant geomagnetic latitude, and lines of constant MLT, into the XY_{gsm} equatorial plane (to the left of the X_{gsm}=-15 R_E line) and into the orthogonal YZ_{gsm} plane (to the right of the X_{gsm}=-15 R_E line). The mappings were done using the T87 model for Kp=0,0+. [*Fairfield*, 1991].

b. The same as in a., but for the T87 model with Kp=2,2+.

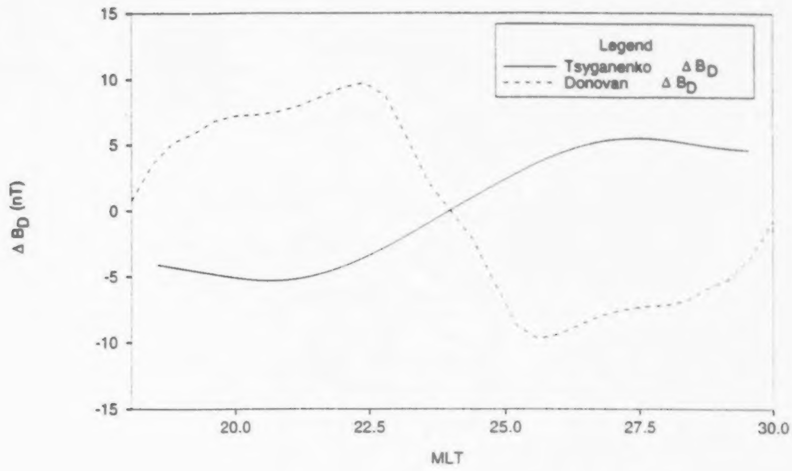

Figure 71. ΔB_D values, as calculated for the interval 0054 to 0116 UT on 3 April 1986 using the Donovan and T87 models. The ΔB_D values are plotted for all nightside MLT at geostationary orbit, at a height of 1 R_E above the gsm equatorial plane.

5. DISCUSSION AND CONCLUSIONS

DISCUSSION

Mappings of substorm activity in this thesis were performed using two different magnetospheric models. The approach taken in using the Donovan model required first establishing a quiet time magnetospheric magnetic field and current configuration. The substorm magnetospheric magnetic field configuration was then modelled by using parameters consistent with the nature of the substorm activity, and adjusting the model to fit the disturbed magnetic field values at geostationary orbit.

As part of the modelling considerations for the Donovan model, a survey was conducted of one year of magnetic field data at geostationary orbit. In this survey of GOES data, seasonal variations were identified in quiet time magnetic field measurements made in the VDH coordinate system; these seasonal variations were attributed to a hinging of the neutral sheet in the nightside near-earth region. In order to remove such seasonal effects from the quiet time GOES data set, a method of data analysis was developed in which the geostationary magnetic field measurements were transformed, such that all data were then representative of a zero dipole tilt configuration. The transformed data set predicted an angle of inclination of $\sim 85\,^\circ$ for the magnetic field at the neutral sheet position, and this result confirmed the *Lopez* [1990] expression for the displacement of the neutral sheet. The hinging distance is therefore located earthward of geostationary orbit, even during quiet times, and this is an important consideration in studies of near-earth magnetic field data.

There is a great deal of interest in the near-earth magnetotail close to, and a few R_E beyond, geostationary orbit. It is believed that an enhancement of the cross-tail current takes place in this region during substorm growth phase, with a subsequent disruption of the current occuring at expansive phase onset. Many studies are therefore conducted of this near-earth region, in order to investigate and understand the magnetotail involvement in magnetospheric substorms. It is almost always necessary to construct data sets for such studies from measurements made at different times of year, due to the lack of measurements available from an array of satellites at any one time. Previous studies of the location of the neutral sheet had determined the average hinging distance to be $X_{gsm} \sim$ - 10.5 R_E [*Fairfield*, 1980]. It has therefore been assumed in previous studies of near-earth magnetic field measurements, such as those done by *Iijima et al.* [1990] and *Zanetti et al.* [1991], that the neutral sheet is located in the magnetic equatorial plane in this near-earth region, such that the hinging of the neutral sheet is not considered to have any effects on measurements made earthwards of $\sim X_{gsm}$ -10.5 R_E. The previous studies of near-earth magnetic field data, and the inferred current configurations, are therefore not necessarily correct in the treatment of the data. As determined in chapter 3 of this thesis, any data set acquired over a period of time in the near-earth nightside magnetosphere must be processed to remove seasonal effects, in order for the data set to be properly represented.

The displacement of the neutral sheet from the magnetic equatorial plane not only has a seasonal dependence, but also varies with the level of magnetic activity. It is therefore necessary to account for the position of the satellite with respect to the neutral sheet when comparing disturbed geostationary magnetic field measurements with quiet time values, even when both measurements are made for approximately the same value of dipole tilt angle. Studies of the magnetic field at geostationary orbit, such as those carried out by *Ohtani et al.* [1991], have been used to infer the relative enhancement of currents during substorm activity, as compared to quiet time values. In the *Ohtani et al.* study, quiet time magnetic field values were subtracted from measurements of the disturbed magnetic field. Both the quiet time and disturbed measurements were made within weeks of each other, in order to remove seasonal effects. The satellite position with respect to the neutral sheet changes with the level of activity, however, and this effect is not removed from the data in the *Ohtani et al.* study. The perturbation values reflect changes in the magnetic field configuration at the satellite position which are caused not only by the enhancement of currents, but also by the movement of the neutral sheet with respect to the satellite. It is therefore necessary to instead calculate quiet time magnetic field values at the height of the satellite above the disturbed position of the neutral sheet (as was done in chapter 4). The substorm perturbations from these quiet time values then represent the effects of enhanced current strengths, or changes in the current configuration, with the effects due to relative differences in the quiet and disturbed positions of the neutral sheet removed.

The perturbations observed at geostationary orbit during the substorm event were modelled by increasing the strength of the cross-tail, ring, magnetopause and field-aligned currents in the Donovan model from the quiet time configuration. Variations in the ΔB_D component at GOES 5 were attributed to a movement of the inner edge of the CPS, such that the satellite was located at different positions with respect to the region 2 field-aligned currents. Measurements made at geostationary orbit during a substorm event therefore reflect not only an enhancement, but also the motion, of the large-scale magnetospheric currents. It is important to consider the relative effects of both the enhancement and the reconfiguration of current systems when interpreting variations in the disturbed magnetic field values at geostationary orbit. The geostationary satellites are located close to the inner edge of the CPS, where the B_D component of the magnetic field is sensitive to an earthward motion of the CPS and the associated field-aligned currents. A large increase in B_D may not necessarily reflect a sudden increase in the field-aligned current strength, but a movement of the region 2 boundary earthward of the satellite. Only from a detailed study of the individual substorm event can the nature of such B_D variations be determined.

The mappings of substorm auroral features presented in chapter 4 revealed differences between the T87 and Donovan magnetic field models. The Donovan mapping of the high latitude 0054 UT intensification extended from dusk to X_{gsm} $\sim$ -10 R_E, along a region near the magnetopause. The T87 model mapped the same intensification farther downtail, to a region beyond $X_{gsm} < -10$ R_E where the auroral activity closest to dusk mapping farthest downtail. The discrepancies between the mappings can be attributed to the presence of "neutral regions" near the flanks of the T87 model magnetotail. These "neutral regions" in the model lie inside the actual magnetopause position, and such unrealistic regions of magnetic field make the T87 model unreliable for mapping high latitude auroral features near dusk. The Donovan model includes a model magnetopause, and the Donovan mapping of the 0054 UT intensification is more ordered in the magnetotail than the T87 mapping.

The Donovan model maps the 0116 UT surge into the region -17 $R_E < X_{gsm} <$ -7 R_E, 11 $R_E < Y_{gsm} <$ 13 R_E. The T87 model maps this surge closer to the centre of the tail. The discrepancies in the two mappings can be attributed to the lack of field-aligned currents in the T87 model. When these effects are taken into account, the different approaches taken in developing the T87 and Donovan models give similar results for mapping the auroral activity located near 2000 MLT. The discrepancies between the two models become larger for mappings of activity closer to dusk, such as the 0054 UT intensification.

The magnetotail source regions of auroral activity, and possible underlying physical processes leading to such activity, can be inferred from the mappings done in this thesis. There are several theories which attempt to explain, in terms of physical processes, the observations associated with substorm activity. *Lui* [1991] has discussed the various theories of substorm development and has proposed a synthesis model for substorms. *McPherron* [1991] has also written a review of the competing substorm theories, and the reader is referred to both the *Lui* and the *McPherron* references for descriptions of various substorm theories. Only physical processes relevant to an interpretation of the mappings performed in this thesis will be mentioned in subsequent discussions of magnetotail sources of substorm activity.

The LLBL is $\sim 0.4\ R_E$ thick at dusk on average [*Eastman and Hones*, 1979], and the dusk region of the Donovan mapping therefore lies along the LLBL for the 0054 UT intensification. As discussed in chapter 1, there are vorticities and velocity shears in the LLBL which are thought to generate the region 1 field-aligned currents. The 0054 UT intensification takes place during a substorm growth phase, in which there is an enhancement of directly driven activity. It is therefore likely that at least part of the region of enhanced upward field-aligned current observed in the ionosphere at 0054 UT is generated at the boundary regions, via an enhancement of the solar wind-magnetosphere dynamo processses and an increased transfer of energy into the magnetosphere at the LLBL.

The 0116 UT surge maps to a region of the magnetotail that lies between the LLBL and the centre of the tail. As determined from ground and satellite magnetic field measurements, this intensification takes place during substorm growth phase, and is not associated with a disruption of the cross-tail current accompanied by a large unloading of stored magnetotail energy. The azimuthally localized disturbance at 0116 UT is caused by an instability in the magnetotail which extends over $\sim 10\ \mathrm{R_E}$ in the X_{gsm} direction. The terms in equation 12 indicate that field-aligned currents are generated by vorticity and/or pressure gradients in the magnetotail plasma. The nature of the mapping for this intensification therefore suggests that the surge is an auroral manifestation of localized vorticity, or a pressure gradient, along a locus of constant X_{gsm} in the magnetotail.

Two explanations may account for such an X_{gsm} - aligned discontinuity in the magnetotail plasma properties. It is possible that the region 1 field-aligned current may be stronger than the values used in the Donovan model for this event. In this case the magnetic field lines carrying the field-aligned current may be flared more towards the flanks than the mapping indicates. Increasing the field-aligned current strengths in the Donovan model for this event could lead to the region 1 current mapping to the LLBL, as suggested by *Rostoker and Eastman* [1987]. Another explanation of this activity is that a region of fast earthward plasma flow may develop during a burst of reconnection, in an azimuthally localized region in the center of the tail, bounded on both sides by slower earthward flows, as suggested by *Hesse and Birn* [1991]. The velocity shear along the dusk interface between the slow and fast flowing plasma could generate upward field-aligned current carried by the hot electrons responsible for the auroras detected by Viking.

CONCLUSIONS

In summary, magnetic field data from the GOES 5 and 6 geostationary satellites have been used to determine the quiet time magnetic field configuration in the nightside magnetosphere at a radial distance of 6.6 R_E. The magnetic field model developed by *Donovan* [1993b] was then used to model a quiet time magnetospheric current configuration which matched the quiet time magnetic field measurements. The quiet time results allowed a better understanding of the origin of transient disturbances detected at geostationary orbit during substorm activity, for which Viking imager data were available. The Donovan magnetic field model, modified for higher activity levels, was successful in permitting a proper interpretation of some geostationary orbit magnetic field disturbances in terms of a movement of the large-scale (directly driven) field-aligned currents, rather than a manifestation of the substorm current wedge. Mappings of auroral forms in the poleward portion of the evening sector auroral oval placed the sources of these disturbances along a locus aligned in the X_{gsm} direction, stretching over distances from $X_{gsm} \sim 2$ R_E to as far downtail as $X_{gsm} = -17$ R_E.

APPENDIX A. COORDINATE SYSTEMS AND TRANSFORMATIONS

Many coordinate systems are used in the field of space physics. The different systems have arisen from a need to express ground and satellite measurements, and theoretical calculations, in the most convenient coordinate system possible. The choice of coordinate system depends on the nature of the physical processes being studied, and the geometry in which calculations are most easily performed. Measurements of magnetospheric phenomena are best expressed in geocentric coordinates, while measurements of solar phenomena are best expressed in heliocentric coordinate systems. Only geocentric coordinates systems are considered in this thesis. The choice of a convenient geocentric coordinate system depends on the local magnetic field geometry in which measurements are made. The Earth's dipole magnetic field is dominant in the near-earth region, while the magnetospheric magnetic field plane of symmetry becomes aligned with the Sun-Earth ecliptic plane in the magnetotail (at distances of $\sim$ 12-15 R_E [*Fairfield et al.*, 1987]). The coordinate systems described in this appendix are classified acccording to whether they are used for ground or magnetotail (satellite) measurements in this thesis.

COORDINATE SYSTEMS FOR GROUND MEASUREMENTS

Ground-based magnetometer records are usually expressed in geographic, geomagnetic coordinates, or local magnetic (HDZ) coordinate systems. The Z axis is the same in all three systems, and is perpendicular to the local surface of the Earth, positive downwards. X and H are tangent to the local surface of the Earth, and X points towards the north geographic pole (north dipole pole) for the geographic (geomagnetic) coordinate system, while H points towards the north magnetic pole.

$\vec{Y}$ is defined as $\vec{Z} \times \vec{X}$, positive eastwards. $\vec{D}$ is similarly defined as $\vec{Z} \times \vec{H}$. D is often measured in degrees of declination from the geographic X axis, but the D component is expressed in nanoteslas for the HDZ coordinates used in this thesis.

COORDINATE SYSTEMS FOR MAGNETOTAIL MEASUREMENTS

GSM: The X_{gsm} axis is aligned with the the Sun-Earth line, positive sunwards. The Y_{gsm} axis is perpendicular to the Earth's magnetic dipole such that the dipole axis is parallel to the XZ_{gsm} plane. Z_{gsm} is positive northwards.

VDH: H is antiparallel to the geomagnetic dipole axis, V lies parallel to the magnetic equatorial plane, and is positive radially outwards from the centre of the Earth. $\vec{D}$ is in the direction of $\vec{H} \times \vec{V}$ (positive eastwards).

COORDINATE TRANSFORMATIONS

Transformations from one coordinate system to another are conducted using rotation matrices. Any transformation can be represented as the product of up to three matrices, each matrix describing a rotation about one of the principal axes:

$$(\mathrm{B}'_{\mathrm{x}}, \mathrm{B}'_{\mathrm{y}}, \mathrm{B}'_{\mathrm{z}}) = < \alpha, \mathrm{X} >< \beta, \mathrm{Y} >< \gamma, \mathrm{Z} > \begin{pmatrix} \mathrm{B}_{\mathrm{x}} \\ \mathrm{B}_{\mathrm{y}} \\ \mathrm{B}_{\mathrm{z}} \end{pmatrix}$$

The general rotation matrices, $< \alpha, X >, < \beta, Y >, < \gamma, Z >$, are described in *Hapgood* [1992]. Rotation angles are determined by the nature of the transformation. Several coordinate rotations are performed in this thesis:

Rotation from geographic to geomagnetic ground coordinates:

The rotation matrix for a transformation from geographic coordinates into geomagnetic coordinates, at a given ground station, is

$$< \gamma, Z >= \begin{pmatrix} \cos\gamma & \sin\gamma & 0 \\ -\sin\gamma & \cos\gamma & 0 \\ 0 & 0 & 1 \end{pmatrix}$$

where γ is the angle between the great circle which passes through the station location and the geomagnetic pole, and the geographic meridian of the station.

Rotation from geographic latitude and longitude into gsm:

This rotation, and expressions required to calculate the rotation angles, are outlined in *Hapgood* [1992].

GOES rotation:

The rotation from GOES satellite coordinates (Hp,He,Hn) into the VDH coordinate system is a product of two rotations, in the satellite "pn" (YZ) and "pe" (XZ) planes:

$$< \alpha, X >< \beta, Y >$$

where $\alpha = C \sin\lambda$, $\beta = C \cos\lambda$, $C \equiv$ geographic colatitude of the north geomagnetic pole, and $\lambda \equiv$ degrees of longitude between the satellite geographic meridian and the geographic meridian of the north geomagnetic pole. The geographic latitude, ϕ, and longitude, λ, of the dipole north geomagnetic pole are given by *Hapgood* [1992] as follows:

$$\phi = 78.8 + 4.283 \times 10^{-2} \frac{MJD - 46066}{365.25}$$

$$\lambda = 289.1 - 1.413 \times 10^{-2} \frac{MJD - 46066}{365.25}$$

where MJD is the modified Julian date, which is the time (in days) from 0000 UT on 17 November 1858.

APPENDIX B. GEOMAGNETIC INDICES

Geomagnetic indices provide a measure of the level of magnetospheric activity. Several indices exist, each one measuring different manifestations of magnetic activity. Three indices, AE, Kp, and Dst, are utilized in this thesis; outlines of their derivations are given in *Rostoker* [1972]. The AE, Kp, and Dst indices are described as follows:

AE: The AE index provides an indication of auroral zone activity. It is derived from magnetic field measurements at 12 ground stations distributed in an approximately uniform longitudinal array in the auroral, and slightly sub-auroral, zone. Only the H (horizontal, directed towards the north geomagnetic pole) component of the magnetic field, which is indicative of electrojet activity, is considered in construction of the index. The H values from each station are scaled and superimposed in a magnetogram format. AE is calculated as the difference between the upper envelope (AU) and lower envelope (AL) of the superimposed values at a given time. The index is usually calculated at 2.5 minute intervals.

Problems arise in using this index to measure localized magnetic activity. The array of stations used in calculations of the index do not necessarily detect substorms which take place on a contracted oval (during quiet conditions), or substorms which occur on an expanded oval (during very active conditions) when the oval is displaced well equatorward of its average position. It is possible that a large disturbance may occur that is not detected at any of the stations, and hence is not reflected in the AE value. Additionally, a large directly driven system may enhance the electrojet such that substorm wedge signatures are not large enough to be measured over and above the electrojet disturbance when all magnetograms are superimposed.

Kp : The Kp index provides a quantitative measure of magnetic disturbance levels. Kp values range from 0 - 9, with plus and minus symbols to denote values between intervals, i.e. 1-, 1, 1+. The Kp derivation makes use of measurements of all three magnetic field components (in local geomagnetic coordinates) from 11 sub-auroral zone stations, and is calculated for three hour intervals. The absolute minimum and absolute maximum values, during the three hour interval, are determined for each component at a given station. The difference between these maximum and minimum values are then calculated for each component, and the maximum difference is scaled for each station, and converted to a K index, using a logarithmic scale. The K indices of each station are then corrected for regional peculiarities and averaged to determine Kp.

The Kp index is best used to determine long-term trends in magnetospheric activity, rather than identify individual substorm events. A large value of Kp indicates substorm activity during the three hour interval in which the index was measured. However, the time of substorm onset(s), and the duration of the substorm, cannot be determined from the Kp index. The value of Kp is also limited by the locations of stations used in the determination of the index. It is possible that substorm activity may take place at high latitudes, and not be detected by any of the sub-auroral zone stations. This type of activity would therefore not be reflected in the Kp index.

Dst : The Dst index gives an indication of the enhancement of the magnetospheric ring current. It is derived from measurements at 5 ground stations which are located at low latitudes, such that they are far from the influence of auroral and equatorial electrojets. The stations are equally spaced in longitude so as to provide uniform coverage in local time. Only the H components at each station are considered in the calculations. The hourly H average is calculated for each station (from one minute values) and the Dst value:

$$\text{Dst} = < \Delta H(t) > - < S_q(t) > - < \Delta H_o >$$

is calculated for the station. The Dst value reflects the disturbance of the H value from quiet values, due to increases in magnetospheric current strengths alone. The hourly Dst value is then calculated as the average of the Dst values at each station.

Problems arise in using this index to calculate the strength of the symmetric ring current during substorms. A localized nightside partial ring current develops during periods of enhanced activity, and the effects of this asymmetric ring current are measured in the Dst value, in addition to the effects from the symmetric ring current [*Mayaud*, 1980]. The Dst index does not allow for a discrimination between the symmetric and partial ring current contributions.

Bibliography

Akasofu, S.-I., The development of the auroral substorm, *Planet. Space Sci.*, *12*, 273, 1964.

Akasofu, S.-I., S. Chapman and A. B. Heinel, The aurora, in *Handbuch der Physik*, volume XLIXII (Geophysics III), part 1, edited by S. Flügge, p. 1, Springer-Verlag, New York, 1966.

Akasofu, S.-I., *Polar and Magnetospheric Substorms*, Reidel, Dordrecht, 1968.

Akasofu, S.-I., What is a magnetospheric substorm, in *Dynamics of the Magnetosphere*, edited by S.-I. Akasofu, p. 447, D. Reidel, Hingham, Mass., 1979.

Anger, C. D., S. K. Babey., A. Lyle Broadfoot, R. G. Brown, L. L. Cogger, R. Gattinger, J. W. Haslett, R. A. King, D. J. McEwen, J. S. Murphree, E. H. Richardson, B. R. Sandel, K. Smith and A. Vallance Jones, An ultraviolet imager for the Viking spacecraft, *Geophys. Res. Lett.*, *14*, 387, 1987.

Axford, W. I. and C. O. Hines, A unifying theory of high latitude geophysical phenomena and geomagnetic storms, *Can. J. Phys.*, *39*, 1433, 1961.

Axford, W. I., H. E. Petschek, and G. L. Siscoe, Tail of the magnetosphere, *J. Geophys. Res.*, *70*, 1231, 1965.

Baker, D. D., Particle and field signatures of substorms in the near magnetotail, in *Magnetic Reconnection in Space and Laboratory Plasmas, Geopys. Monogr. Ser.*, volume 30, edited by E. W. Hones, p.193, AGU, Washington, D.C., 1984.

Bame, S. J., J. R. Ashbridge, H. E. Felthauser, E. W. Hones, and I. B. Strong, Characteristics of the plasma sheet in the Earth's magnetotail, *J. Geophys. Res.*, *72*, 113, 1967.

Baumjohann, W. and G. Haerendel, Dayside Convection, viscous interaction and magnetic merging, in *Solar Wind-Magnetosphere Coupling*, edited by Y. Kamide and J. A. Slavin, p. 415, Terra Scientific Publishing Company, Tokyo, 1986.

Baumjohann, W., G. Paschmann, and C. A. Cattell, Average plasma properties in the central plasma sheet, *J. Geophys. Res.*, *94*, 6597, 1989.

Biermann, L., Solar corpuscular radiation and the interplanetary gas, *Observatory*, *77*, 109, 1957.

Birkeland, K., *The Norwegian aurora polaris expedition 1902-1903*, volume 1, p. 1, H. Aschehoug and Co., Christiania, 1908.

Boström, R., A model of the auroral electrojets, *J. Geophys. Res.*, *69*, 4983, 1964.

Burch, C. R., Reflecting Microscopes, *Proc. Phys. Soc.*, *59*, 41, 1947.

Chapman, S., and V. C. A. Ferraro, A new theory of magnetic storms, *Nature*, *126*, 129, 1930.

Cole, A. E., A. Court, and A. J. Kantor, Model Atmospheres, in *Handbook of Geophysics and Space Environments*, edited by S. L. Valley, p. 2-1 Air Force Cambridge Research Laboratories, United States Air Force, 1965.

Clauer, C. R., and R. L. McPherron, Mapping the local time-universal time development of magnetospheric substorms using mid-latitude magnetic observations, *J. Geophys. Res.*, *79*, 2811, 1974.

Cummings, C. D., J. N. Barfield, and P. J. Coleman, Magnetospheric substorms observed at the synchronous orbit, *J. Geophys. Res.*, *73*, 6687, 1968.

Donovan, E. F. and G. Rostoker, Internal consistency of the Tsyganenko magnetic field model and the Heppner-Maynard empirical model of the ionospheric electric field distribution, *Geophys. Res. Lett.*, *18*, 1043, 1991.

Donovan, E. F., G. Rostoker and C. Y. Huang, Regions of negative Bz in the Tsyganenko 1989 model neutral sheet, *J. Geophys. Res.*, *97*, 8697, 1992.

Donovan, E. F., Modelling the magnetic effects of field-aligned currents, *J. Geophys. Res.*, *98*, 13529, 1993a.

Donovan, E. F., Modelling the Magnetic Effects of Distributed Magnetospheric Currents, Ph.D. Thesis, University of Alberta, 1993b.

Donovan, E. F., G. Rostoker, S. H. Skone, B. T. Sijgers, C. V. Tran, B. Jackel, Modeling the nightside magnetospheric magnetic field, *EOS Trans. AGU*, *74*, 43, p. 539, 1993.

Dungey, J. W., Interplanetary magnetic field and the auroral zones, *Phys. Rev. Lett*, *6*, 47, 1961.

Dungey, J. W., The structure of the exosphere or adventures in velocity space, in *Geophysics. The Earth's Environment*, Gordon and Breach, New York, 1963.

Eastman, T. E. and E. W. Hones, Characteristics of the magnetospheric boundary layer and magnetopause layer as observed by IMP 6, *J. Geophys. Res.*, *84*, 2019, 1979.

Eastman, T. E., L. A. Frank, W. K. Peterson, and W. Lennartsson, The plasma sheet boundary layer, *J. Geophys. Res.*, *89*, 1553, 1984.

Elphinstone, R., D. J. S. Murphree, L. L. Cogger, D. Hearn, M. G. Henderson, and R. Lundin, Observations of changes to the auroral distribution prior to substorm onset, in *Magnetospheric Substorms*, Geophysical Monograph 64, edited by J. R. Kan, T. A. Potemra, S. Kokubun, T. Iijima, p. 257, AGU, Washington, D. C., 1991.

Fairfield, D. H., Magnetic field signatures of substorms on high-latitude field lines in the nighttime magnetosphere, *J. Geophys. Res.*, *78*, 1553, 1973.

Fairfield, D. H., A statistical determination of the shape and position of the geomagnetic neutral sheet, *J. Geophys. Res.*, *85*, 775, 1980.

Fairfield, D. H., Structure of the geomagnetic tail, in *Magnetotail Physics*, edited by A. T. Y. Lui, p. 23, Johns Hopkins University Press, Baltimore, MD, 1987.

Fairfield, D. H., M. E. Acuna, L. J. Zanetti and T. A. Potemra, The magnetic field of the equatorial magnetotail: AMPTE/CCE observations at $R < 8.8R_E$, *J. Geophys. Res.*, *92*, 7432, 1987.

Fairfield, D. H., An evaluation of the Tsyganenko magnetic field model, *J. Geophys. Res.*, *96*, 1481, 1991.

Feldstein, Y. I., and G. V. Starkov, Dynamics of auroral belt and polar geomagnetic disturbances, *Planet. Space Sci.*, *15*, 209, 1967.

Goertz, C. K. and R. W. Boswell, Magnetosphere-ionosphere coupling, *J. Geophys. Res.*, *84*, 7239, 1979.

Hapgood, M. A., Space physics coordinate transformations: a user's guide, *Planet. Space Sci.*, *40*, 711, 1992.

Harang, L., The mean field of disturbance of polar geomagnetic storms, *Terr. Magn. Atmos. Elect.*, *51*, 353, 1946.

Hasegawa, A. and T. Sato, Generation of field-aligned current during substorm, in *Dynamics of the Magnetosphere*, edited by S.-I. Akasofu, p. 529, D. Reidel, Hingham, Mass., 1979.

Heppner, J. P., The Harang discontinuity in auroral belt ionospheric currents, *Geofys. Publ.*, *29*, 105, 1972.

Hesse, M. and J. Birn, Progress in the study of three-dimensional plasmoids, in *Modeling the Magnetospheric Plasma Processes*, p. 55, AGU, Washington, D.C., 1991.

Hines, C. O., The energization of plasma in the magnetosphere: hydromagnetic and particle drift approaches, *Planet. Space Sci.*, *10*, 239, 1963.

Hones, E. W., T. Pytte, and H. I. West, Associations of geomagnetic activity with plasma sheet thinning and expansion: A statistical study, *J. Geophys. Res.*, *89*, 5471, 1984.

Huang, C. Y. and L. A. Frank, A statistical study of the central plasma sheet: Implications for substorm models, *Geophys. Res. Lett.*, *13*, 652, 1986.

Hughes, T. J. and G. Rostoker, Current flow in the magnetosphere and ionosphere during periods of moderate activity, *J. Geophys. Res.*, *82*, 2271, 1977.

Hughes, T. J., A Comprehensive Model of Ionospheric-Magnetospheric Current Systems During Periods of Moderate Magnetospheric Activity, Ph.D. Thesis, University of Alberta, 1978.

Hultqvist, B., The Viking project, *Geophys. Res. Lett.*, *14*, 379, 1987.

IAGA Commission 2 Working Group 4, International geomagnetic reference field 1965.0, *J. Geophys. Res.*, *74*, 4407, 1969.

Iijima, T. and T. A. Potemra, The amplitude distribution of field-aligned currents at northern high latitudes observed by TRIAD, *J. Geophys. Res.*, *81*, 2165, 1976.

Iijima, T. and T. A. Potemra, Large scale characteristics of field-aligned currents associated with substorms, *J. Geophys. Res.*, *83*, 599, 1978.

Iijima, T. and T. A. Potemra, Large-scale characteristics of Birkeland currents, in *Dynamics of the Magnetosphere*, edited by S.-I. Akasofu, p. 165, D. Reidel, Hingham, Mass., 1979.

Iijima, T., T. A. Potemra, and L. J. Zanetti, Large scale characteristics of magnetospheric equatorial currents, *J. Geophys. Res.*, *95*, 991, 1990.

Jordan, C. E., J. N. Bass, M. S. Gussenhoven, H. J. Singer, and R. V. Hilmer, Comparison of magnetospheric magnetic field models with CRRES observations during the August 26, 1990, storm, *J. Geophys. Res.*, *97*, 16907, 1992.

Kamide, Y., ***Electrodynamic Processes in the Earth's Ionosphere and Magnetosphere***, Kyoto Sangyo University Press, Kyoto, Japan, 1988.

Kan, J. R., Generation of field-aligned currents in magnetosphere-ionosphere coupling in a MHD plasma, *Planet. Space Sci.*, *35*, 903, 1987.

Kavanagh, L. D., Magnetospheric structure, in *Earth's Magnetospheric Processes*, edited by B. McCormac, p.3, 1972.

Kaufmann, R. L., Substorm currents: growth phase and onset, *J. Geophys. Res.*, *92*, 7471, 1987.

Kidd, S. R., and G. Rostoker, Distribution of auroral surges in the evening sector, *J. Geophys. Res.*, *96*, 5697, 1991.

Kisabeth, J. L., Development of the polar electrojets, Ph.D. Thesis, University of Alberta, 1972.

Kokobun, S., and R. L. McPherron, Substorm signatures at synchronous altitude, *J. Geophys. Res.*, *86*, 11265, 1981.

Langel, R. A., The main field, in *Geomagnetism*, edited by J. A. Jacobs, volume 1, p. 249, Academic Press, London, 1987.

Lassen, K., Relation of the plasma sheet to the nighttime auroral oval, *J. Geophys. Res.*, *79*, 3857, 1974.

Lopez, R. E., The position of the neutral sheet in the near-Earth region, *Geophys. Res. Lett.*, *17*, 1617, 1990.

Lopez, R. E., and T. von Rosenvinge, A statistical relationship between the geosynchronous magnetic field and substorm electrojet magnitude, *J. Geophys. Res.*, *98*, 3851, 1993.

Lui, A. T. Y., C. D. Anger, and S. -I. Akasofu, The equatorward boundary of the diffuse aurora and auroral substorms as seen by the ISIS 2 auroral scanning photometer, *J. Geophys. Res.*, *80*, 3603, 1975.

Lui, A. T. Y., Estimates of current changes in the geomagnetotail associated with a substorm, *Geophys. Res. Lett.*, *5*, 853, 1978.

Lui, A. T. Y., Road map to magnetotail domains, in *Magnetotail Physics*, edited by A. T. Y. Lui, p. 3, Johns Hopkins University Press, Baltimore, MD, 1987.

Lui, A. T. Y., R. W. McEntire, and S. M. Krimigis, Evolution of the ring current during two geomagnetic storms, *J. Geophys. Res.*, *92*, 7459, 1987.

Lui, A. T. Y., A synthesis of magnetospheric substorm models, *J. Geophys. Res.*, *96*, 1849, 1991.

Lundin, R., L. R. Lyons, and N. Pissarenko, Observations of ring current composition at L < 4, *Geophys. Res. Lett.*, *7*, 425, 1980.

Lyons, L. R., and D. J. Williams, *Quantitative Aspects of Magnetospheric Physics*, D. Reidel Publishing Company, Boston, Mass., 1984.

Manuel, J. R., and J. C. Samson, The spatial development of the low-latitude boundary layer, *J. Geophys. Res.*, *98*, 17367, 1993.

Mayaud, P. N., *Derivation, Meaning, and Use of Geomagnetic Indices*, AGU, Washington, D. C., 1980.

McIlwain, C. E., Substorm injection boundaries, in *Magnetospheric Physics*, edited by B. M. McCormac, p. 143, D. Reidel, Hingham, Mass., 1974.

McPherron, R. L., Growth phase of magnetospheric substorms, *J. Geophys. Res.*, *75*, 5592, 1970.

McPherron, R. L., Substorm related changes in the geomagnetic tail: The growth phase, *Planet. Space Sci.*, *20*, 1521, 1972.

McPherron, R. L., C. T. Russell, and M. P. Aubry, Satellite studies of magnetospheric substorms on August 15, 1968, 9, Phenomenological model for substorms, *J. Geophys. Res.*, *78*, 3131, 1973.

McPherron, R. L., and J. N. Barfield, A seasonal change in the effect of field-aligned currents at synchronous orbit, *J. Geophys. Res.*, *85*, 6743, 1980.

McPherron, R. L., Physical processes producing magnetospheric substorms and magnetic storms, in *Geomagnetism*, volume 4, edited by J. A. Jacobs, Academic, London, 1991.

Mead, G. D., and D. H. Fairfield, A quantitative magnetospheric model derived from spacecraft magnetometer data, *J. Geophys. Res.*, *80*, 535, 1975.

Miura, A., Anomalous transport of magnetohydrodynamic Kelvin-Helmholtz instabilities in the solar wind-magnetosphere interaction, *J. Geophys. Res.*, *89*, 801, 1984.

Murphree, J. S., R. D. Elphinstone, L. L. Cogger, and D. Hearn, Viking optical substorm signatures, in *Magnetospheric Substorms*, Geophysical Monograph 64, edited by J. R. Kan, T. A. Potemra, S. Kokubun, T. Iijima, p. 241, AGU, Washington, D. C., 1991.

Nagai, T., Observed magnetic substorm signatures at synchronous altitude, *J. Geophys. Res.*, *187*, 4405, 1982.

Newcomb, W. A., Motion of magnetic lines of force, *Ann. Phys.*, *3*, 347, 1958.

Nicholson, W. R., *Introduction to Plasma Theory*, J. Wiley and Sons, New York, 1983.

Ohtani, S., S. Kokubun, R. C. Elphic, and C. T. Russell, Field-aligned current signatures in the near-tail region 1. ISEE observations in the plasma sheet boundary layer, *J. Geophys. Res.*, *93*, 9709, 1988.

Ohtani, S., S. Kokubun, R. Nakamura, R. C. Elphic, C. T. Russell, and D. N. Baker, Field-ailigned current signatures in the near-tail region 2. Coupling between the region 1 and the region 2 systems, *J. Geophys. Res.*, *95*, 18913, 1990.

Olson, W. P. and K. A. Pfitzer, A quantitative model of the magnetospheric magnetic field, *J.Geophys. Res.*, *79*, 3739, 1974.

Parker, E. N., Newtonian development of the dynamical properties of ionized gases of low density, *Phys. Rev.*, *107*, 924, 1957.

Parker, E. N., Interaction of the solar wind with the geomagnetic field, *Phys. Fluids*, volume 1, 171, 1958.

Parks, G. K., *Physics of Space Plasmas, An Introduction*, Addison Wesley, Redwood City, Ca., 1991.

Perreault, P., and S.-I. Akasofu, A study of geomagnetic storms, *Geophys. J. R. Astr. Soc.*, *54*, 547, 1978.

Rostoker, G., Geomagnetic Indices, *Rev. Geophys. and Space Phys.*, *10*, 935, 1972.

Rostoker, G., S.-I. Akasofu, J. Foster, R. A. Greenwald, Y. Kamide, K. Kawasaki, A. T. Y. Lui, R. L. McPherron, and C. T. Russell, Magnetospheric substorms-definition and signatures, *J. Geophys. Res.*, *85*, 1663, 1980.

Rostoker, G., S.-I. Akasofu, W. Baumjohann, Y. Kamide and R. L. McPherron, The roles of direct input of energy from the solar wind and unloading of stored magnetotail energy in driving magnetospheric substorms, *Space Sci. Rev.*, *46*, 93, 1987.

Rostoker, G. and T. E. Eastman, A boundary layer model for magnetospheric substorms, *J. Geophys. Res.*, *92*, 12187, 1987.

Rostoker, G., Magnetospheric substorms as a signature of the solar terrestrial interaction, in *Ionospheric Structure and Variability on a Global Scale and Interactions with Atmosphere and Magnetosphere*, edited by L. Bossy and R. W. Schunk, p.2, AGARD-CP-441, Neury Sur Seine, France, 1989.

Rostoker, G., Some observational constraints for substorm models, in *Magnetospheric Substorms*, Geophysical Monograph 64, edited by J. R. Kan, T. A. Potemra, S. Kokubun and T. Iijima, p. 61, AGU, Washington, D. C., 1991.

Rostoker, G., Mapping of regions of auroral activation in the ionosphere to the magnetotail, in *Proceedings of the International Conference on Substorms (ICS-1)*, Kiruna, Sweden, 23-27 March 1992, ESA SP-335, p. 71, 1992.

Rostoker, G. and S. H. Skone, Magnetic flux mapping considerations in the auroral oval and the Earth's magnetotail, *J. Geophys. Res.*, *98*, 1377, 1993.

Rufenach, C. L., R. L. McPherron, and J. Schaper, The quiet geomagnetic field at geosynchronous orbit and its dependence on solar wind dynamic pressure, *J. Geophys. Res.*, *97*, 25, 1992.

Samson, J. C., D. D. Wallis, T. J. Hughes, F. Creutzberg, J. M. Ruohoniemi, and R. A. Greenwald, Substorm intensifications and field line resonances in the nightside magnetosphere, *J. Geophys. Res.*, *97*, 8495, 1992.

Sato, T., Auroral Physics, in *Magnetospheric Plasma Physics*, edited by A. Nishida, p. 197, D. Reidel, Dordrecht, 1982.

Savaud, J.-A., and J. R. Winckler, Dynamics of plasma, energetic particles, and fields near synchronous orbit in the nighttime sector during magnetospheric substorms, *J. Geophys. Res.*, *85*, 2043, 1980.

Sibeck, D. G., R. E. Lopez, and E. C. Roelof, Solar wind control of the magnetopause shape, location and motion, *J. Geophys. Res.*, *896*, 5489, 1991.

Siscoe, G. L., The magnetospheric boundary, in *Physics of Space Plasmas (1987)*, edited by T. Chang, G. B. Crew and J. R. Jasperse, p. 3, Scientific Publishers, Cambridge, Mass., 1987.

Speiser, T. W., Particle trajectories in model current sheets 1. Analytical solutions, *J. Geophys. Res.*, *70*, 4219, 1965.

Tsyganenko, N. A., Global quantitative models of geomagnetic field in the cislunar magnetosphere for different disturbance levels, *Planet. Space Sci.*, *35*, 1347, 1987.

Tsyganenko, N. A., A magnetospheric magnetic field model with a warped tail current sheet, *Planet. Space Sci.*, *37*, 5, 1989.

Vallance Jones, A., R. L. Gattinger, F. Creutzberg, R. A. King, P. Prikryl, L. L. Cogger, D. J. McEwen, F. R. Harris, C. D. Anger, J. S. Murphree, and R. A. Koehler, A comparison of CANOPUS ground optical data with images from the Viking UV camera, *Geophys. Res. Lett.*, *14*, 391, 1987.

Vasyliunas, V. M., Fundamentals of current description, in *Magnetospheric Currents*, Geophysical Monograph 28, edited by T. A. Potemra, p. 63, AGU, Washington, D. C., 1984.

Voigt, G.-H., The shape and position of the plasma sheet in Earth's magnetotail, *J. Geophys. Res.*, *89*, 2169, 1984.

Wallis, D. D. and E. E. Budzinski, Empirical models of height integrated conductivities, *J. Geophys. Res.*, *86*, 125, 1981.

Wiens, R. G., and G. Rostoker, Characteristics of the development of the westward electrojet during the expansive phase of magnetospheric substorms, *J. Geophys. Res.*, *80*, 2105, 1975.

Williams, D. J. and G. D. Mead, Night side magnetosphere configuration as obtained from trapped electrons at 1100 kilometers, *J. Geophys. Res.*, *70*, 3017, 1965.

Yasuhara, F., Y. Kamide and S.-I. Akasofu, Field-aligned and ionospheric currents, *Planet. Space Sci.*, *23*, 1355, 1975.

Zanetti, L. J., T. A. Potemra, T. Iijima, and W. Baumjohann, Equatorial, Birkeland, and ionospheric currents of the magnetospheric storm circuit, in *Magnetospheric Substorms*, Geophysical Monograph 64, edited by J. R. Kan, T. A. Potemra, S. Kokubun and T. Iijima, p. 111, AGU, Washington, D. C., 1991.

Zmuda, A. J. and J. C. Armstrong, The diurnal flow pattern of field-aligned currents, *J. Geophys. Res.*, *79*, 4611, 1974.